Development and Analytical Characterization of Lipid-Based Nanoparticles

by

Minzhi Yu

A dissertation submitted in partial fulfillment
of the requirements for the degree of
Doctor of Philosophy
(Pharmaceutical Sciences)
in the University of Michigan
2022

Doctoral Committee:

Professor Anna Schwendeman, Co-Chair
Professor Steven P. Schwendeman, Co-Chair
Professor Y. Eugene Chen
Professor Duxin Sun

Minzhi Yu

minzhiyu@umich.edu

ORCID iD: 0000-0002-3141-7285

Dedication

To my parents with love.

Acknowledgements

First, I would like to thank my parents for their unconditional support and love, as well as for inspiring me to be a life-long learner. And to my grandparents. Thank you for always reminding me to eat well and take care of myself no matter where I am and what happens in life. I would not have had the privilege to finish this thesis without the enormous hard work of my grandparents and parents.

Second, I would like to thank my extremely supportive mentor, Dr. Anna Schwendeman. You have always been a role model for me. I have learned so much from you, not only about scientific research but also about career development, personal growth, and interpersonal skills. Thank you for encouraging me to grow into a better researcher and a stronger person. I would also like to thank my co-advisor, Dr. Steven P Schwendeman. Thank you for teaching me to conduct top-quality research and coaching my scientific communication skills. I would also like to thank Dr. Duxin Sun and Dr. Y. Eugene Chen for their feedback and investment in my research.

I would like to thank the College of Pharmacy, Rackham Graduate School, American Heart Association, National Institute of Health, and Globalization of Pharmaceutics Education Network for funding me over the course of my studies. I am extremely lucky to have the opportunity to work with many collaborators in the past years. I would like to thank Dr. Wenmin Yuan for her mentorship during my first few years in the program. I would like to thank Dr. Yanhong Guo for her guidance, and

Dr.Raymond Adili for his help in my animal studies. I would also like to acknowledge Dr. Yan Wang and other researchers from the FDA, who provided valuable advice on the experiment and manuscript of Chapter 5. I especially want to thank Dr. Christel Bergström for her support and guidance during my visit to Uppsala University.

I am very grateful to work in such a great lab. I would like to thank lab managers Rose Ackermann, Karl Olsen, and Brian Shay for training me and helping me overcome technical challenges in my study. I would like to thank Dr. Hongliang He, Dr. Lisha Liu, and Kristen Hong for their help with animal studies. I would also like to acknowledge Dr. Wenmin Yuan and Ziyun Xia for contributing to the research of Chapter 5 of this dissertation. And to every former and current member of the Schwendeman labs, thank you for creating such a supportive and fun working environment. Thank you all for proofreading my drafts, helping practice presentations, sharing snacks, inviting me to parties, and everything you have done to make graduate school such a wonderful journey.

Finally, I would like to thank my friends for supporting me during my Ph.D. study. To my cohort, Lucy, Hongxiang, Jason, Justin, and Xiaoqi, going through this journey with you is such a wonderful experience. And to friends from Bergström's lab, thank you so much for helping me adjust to a new environment. I hope one day we will have ramen together again in the future. Special thanks to my friend Luyao and Yaqi, who are always there whenever I need to talk to someone. I am so fortunate to know you all in my journey. Until we see each other again, Go Blue!

Table of Contents

List of Tables

List of Figures

Abstract

Lipid-based nanoparticles are highly versatile platforms with extensive therapeutic applications. Despite rapid scientific advances in the past several decades, clinical translation of lipid nanoparticles remains challenging. Focusing on translational research of lipid nanoparticles, this thesis has two sections addressing preclinical formulation development and analytical methods on formulation characterization, respectively.

The first section of the thesis, consisting of Chapters 2 and 3, focuses on the formulation optimization of synthetic high-density lipoproteins (sHDLs). sHDLs are a class of nanoparticles composed of ApoA-1 mimetic peptides and phospholipids mimicking the biofunctions of endogenous HDLs, including mediating cholesterol efflux, regulating endothelial functions, and resolving inflammation responses. To optimize the endothelial protective function of sHDLs, in Chapter 2, a vascular cell adhesion molecule 1 (VCAM-1) specific ligand was introduced on the surface of sHDLs to achieve an active targeting of activated endothelium. Indeed, these sHDLs demonstrated enhanced binding to the activated endothelium while inhibiting inflammatory responses and reducing leukocyte adhesion on inflamed endothelium. These data provided support as a stand-alone therapy or drug delivery carrier for inflammatory disease treatment.

In Chapter 3, phosphatidylserine (PS), a bioactive lipid with intrinsic anti-inflammatory effects, was introduced in sHDL nanoparticles. This incorporation improved the sHDL stability and anti-inflammatory effects on LPS-activated macrophages without impairing the sHDL cholesterol efflux capacity and pharmacokinetic profile. Overall, the strategies developed in Chapters 2 and 3 may facilitate the optimization of sHDL functionalities to treat varieties of inflammatory diseases.

The second section of the thesis, consisting of Chapters 4 and 5, focuses on developing analytical methods to ensure the successful formulation development, regulatory filing, and quality control of liposomal drug products. Chapter 4 examined the dialysis-based drug release assay which is commonly used to evaluate *in vitro* drug release kinetics of lipid nanoparticles. The analysis of the mass transfer process during dialysis assay revealed that due to the drug diffusional resistance of the dialysis membrane, the apparent drug release rate measured from the sampling compartment does not always accurately represent the actual drug release kinetics. To solve this problem, a series of mathematical models were developed to predict actual drug release kinetics from apparent drug release data and a calibration of the diffusional membrane resistance before release testing. The models not only enable the proper interpretation of the data from dialysis studies but also help to evaluate the dialysis methodology applied to *in vitro* drug release assays.

In Chapter 5, a series of analytical methods were developed to characterize the key product attributes of a commercial multivesicular liposomal product, Exparel. The particle size, particle inner structure characteristics, drug and lipid contents, residual

solvents, and pH of the product were characterized. In addition, a rotator-based, sample-and-separate *in vitro* drug release test was developed for formulation comparison and quality control purposes. The batch-to-batch variability of Exparel was examined by the established analytical methods. The knowledge derived from this chapter may facilitate the development of generic multivesicular liposomes.

Chapter 1 Introduction

1.1 Current status and future directions of synthetic high-density lipoprotein therapies

1.1.1 Structure and functions of endogenous high-density lipoprotein (HDL)

High-density lipoproteins (HDLs) are a highly heterogeneous lipoprotein family with a density of 1.063-1.21 g/ml [1]. ApoA-1 is the most abundant apolipoprotein in HDL, whereas other apolipoproteins, such as ApoA-2 and ApoE, are also found in HDL particles[1]. Phospholipids are predominated lipid species of HDLs, accounting for 35-50% of total lipid contents, followed by cholesterol ester (30-40%), sphingolipids (5-10%), cholesterol (5-10%), and triglyceride (5-12%) [2]. Additionally, a large number of proteins have been reported to be associated with endogenous HDLs. Some examples of the associated proteins include lecithin:cholesterol acyl transferase (LCAT), cholesteryl ester transfer protein (CETP), paraoxonase family (PONs), and complement components [1].

Endogenous HDLs play vital roles in various physiological functions, including mediating reverse cholesterol transport (RCT), regulating inflammatory responses, and maintaining endothelial functions [3]. Mediating RCT is the most studied function of HDLs. RCT is initiated by cholesterol efflux, where free cholesterol moves from peripheral cells to ApoA-1 and HDLs mediated by varies mechanisms, including passive

diffusion of cholesterol, facilitated diffusion by scavenger receptor BI (SR-BI), and active transport of cholesterol by ATP-binding cassette transporters A1 (ABCA1) and G1 (ABCG1) [4]. Free cholesterol is then converted to cholesterol ester by lecithin:cholesterol acyltransferase (LCAT) and delivered to the liver for elimination [5]. As the accumulation of cholesterol in the artery wall is the major driving force for the development and progression of atherosclerotic cardiovascular disease, the cholesterol efflux capacity of HDL has been considered the key protective function of HDLs [6].

HDLs also play crucial roles in modulating inflammation responses through mechanisms that can be dependent or independent of the cholesterol mobilization effects of HDLs [7, 8]. On macrophages, cholesterol efflux mediated by HDL reduces the cholesterol content of lipid rafts, which suppresses the expression of Toll-like receptor 4 (TLR-4) on cellular membranes and inhibits the downstream myeloid differentiation primary response 88 (MyD88)/NF-κB or TIR-domain–containing adapter-inducing interferon-β (TRIF) signaling pathways [9]. Independent of cholesterol efflux, HDL could also inhibit TRIF signaling by promoting the translocation of TRIF-related adaptor molecule (TRAM) from the cell membrane to intracellular compartments [10]. Additionally, HDLs could effectively neutralize lipopolysaccharide (LPS) and lipoteichoic acid (LTA), reducing LPS- and LTA-induced inflammatory responses during bacterial infection [11].

Oxidative stress and oxidized lipoprotein, especially oxidized low-density lipoprotein (ox-LDL), are recognized as the main driving force for atherosclerosis [12]. Various HDL-associated enzymes, such as paraoxonase (PON) 1 and lecithin-cholesterol acyltransferase (LCAT), have been shown to prevent the oxidation of LDLs

[13, 14]. Previous studies also suggested the capacity of HDLs to scavenge reactive oxygen species (ROS) such as lipid hydroperoxides from cell membranes [15]. In addition to neutralization of ROS, HDLs could directly inhibit ROS generation through various mechanisms including suppressing inflammatory response and regulating mitochondrial function [16, 17].

Recent studies suggested the pivotal role of HDLs in regulating endothelial functions. Nitric oxide (NO) generated by endothelial NO synthase (eNOS) is essential for the maintenance of vascular tone [18]. On endothelial cells, HDLs preserve eNOS localization on caveolae by modulating the lipid environment [19]. Moreover, HDLs could activate eNOS through SR-BI-dependent activation of phosphatidylinositol-3-kinase-protein-kinase-B (PI3K-AKT) pathway and mitogen-activated protein kinase (MAPK) pathways [20]. Additionally, HDLs exert other endothelial protective functions, including inhibiting the expression of adhesion molecules [21], preventing endothelial cell apoptosis [22], and regulating angiogenesis [23].

Recent studies have been proposing more protective functions of HDLs. For example, HDLs have been found to inhibit platelet activation and reduce platelet aggregation, which is presumably mediated by SR-BI [24]. As the major carrier of circulating microRNAs (miRNA), HDLs are suggested to play crucial roles in mediating intercellular communication [25]. The multifaceted protective functions of HDLs suggest great potential for HDL-targeting therapies to treat varieties of diseases.

1.1.2 Current status of sHDL therapies

Various HDL-mimicking nanoparticles, such as inorganic nanoparticles, polymeric nanoparticles, and liposomes, have been developed to mimic the function of

endogenous HDLs [26-28]. Compared with other HDL-mimicking nanoparticles, synthetic HDLs (sHDLs) composed of phospholipids and recombinant ApoA-1 or its mimetics are the most translatable nanoparticle candidates, given their biocompatible components and available GMP manufacturing process [29]. Several sHDL candidates have entered clinical trials, with two candidates, CLS112 and CER-001, currently active in clinical trials.

1.1.2.1 CSL112

Designed for treating acute coronary syndrome (ACS), CSL112 was formulated with plasma-derived human ApoA-1 and soy phosphatidylcholine (soy PC) to mimic the structure of cholesterol-poor, pre-β subclass of HDLs [30]. Preclinical studies demonstrated the potent ABCA-1-dependent cholesterol efflux capacity of CSL112 *in vitro* and in animal models [30]. In Phase 1 clinical trials, infusion of CSL112 to healthy volunteers was found to significantly increase plasma cholesterol levels over more than 72 h. The half-life of ApoA-1 was estimated to be 19-93 h. In addition, a good safety profile was observed for both single-infusion and repeated-infusion groups [31].

In Phase 2a study, 1.7, 3.4, or 6.8 g CSL112 was infused into patients with stable atherosclerotic disease. Consistent with Phase 1 results, a rapid elevation of plasma ApoA-1 and cholesterol levels was observed following infusion [32]. In the following Phase 2b, ApoA-I Event Reducing in Ischemic Syndromes I (AEGIS-I) study, patients with a spontaneous myocardial infarction in the past 7 days were treated with weekly infusions of low dose CSL112 (2 g ApoA-1/dose), high dose CSL112 (6 g ApoA-1/dose) or placebo for 4 weeks. Again, the results showed that CSL112 was well tolerated, with no significant hepatotoxicity and renal toxicity compared to the placebo [33]. However,

no statistical difference was found between different groups in the number of major adverse cardiovascular events 12 months post-treatment [33]. As the statistical power was low, the efficacy of CSL112 in reducing major adverse cardiovascular events remains inconclusive [33].

The Phase 3, ApoA-I Event Reducing in Ischemic Syndromes II (AEGIS-II) trial is currently ongoing. 17,400 patients with high-risk acute myocardial infarction are randomized to receive 4 weekly infusions of 6 g CSL112 or placebo [34]. The results of this study are expected to determine the efficacy of CSL112 in reducing major adverse cardiovascular events.

1.1.2.2 CER-001

CER-001 is composed of recombinant ApoA-1, egg sphingomyelin (eSM), and dipalmitoyl phosphatidylglycerol (DPPG) [35]. The anionic lipid DPPG, accounting for 3% of total phospholipid weight, was introduced to enhance particle plasma stability and reduce kidney elimination [35]. In animal studies, CER-001 showed strong RCT-enhancing and plaque-reduction effects [35]. Phase 1 clinical trial showed that CER-001 infusion led to a dose-dependent increase in HDL cholesterol with good safety profiles [36]. In Phase 2, Can HDL Infusions Significantly Quicken Atherosclerosis Regression (CHI-SQUARE) study, 6 weekly infusions of CER-001 were given to ACS patients with a dose of 3, 6, 12 mg/kg or placebo. The atheroma volume in ACS patients was measured by intravascular ultrasonography and quantitative coronary angiography [37]. While no statistical difference was found in the atheroma volume reduction between groups, a post-hoc analysis suggested that 3 mg/kg CER-001 produced significant atheroma regression in patients with a baseline percent atheroma volume >30% [37,

38]. Based on this finding, ACS patients with a baseline percent atheroma volume >30% were recruited in the following Phase 2, CER-001 Atherosclerosis Regression Acute Coronary Syndrome Trial (CARAT) study, where 10 weekly infusions of 3 mg/kg CER-001 or placebo were given to patients [39]. However, the difference in the atheroma regression between the treatment and placebo groups was found not statistically significant [40]. No further clinical trial has been conducted for ACS so far.

Other therapeutic applications of CER-001 have been tested in clinical trials. In Phase 2, The Modifying Orphan Disease Evaluation (MODE) study, 32 patients with homozygous familial hypercholesterolemia (HoFH) were treated with 12 biweekly infusions of 8 mg/kg CER-001 [41]. Results showed that 24 weeks after the first infusion, patients treated with CER-001 presented reduced carotid mean vessel wall area compared to the placebo group [41]. In another open-label study, patients with familial hypoalphalipoproteinemia (FHA) received 20 infusions of 8 mg/kg CER-001 over 6 months. CER-001 treatment was found to significantly elevate ApoA-1 and HDL cholesterol levels, as well as reduce carotid mean vessel wall area in FHA patients [42]. Based on these encouraging results, the Phase 3, CER-001 Therapy as a Novel Approach to Treat Genetic Orphan Diseases (TANGO) study was conducted. A total of 29 infusions (9 weekly infusions followed by 20 biweekly infusions) of 8 mg/kg CER-001 or placebo were given to 30 patients with FHA [43]. Unfortunately, results failed to show the therapeutic benefits of CER-001 in reducing carotid mean vessel wall area and arterial wall inflammation [43, 44]. Several possible reasons, such as insufficient dose, limited treatment duration, and interference of prior statin treatment, have been proposed to explain the lack of atherosclerosis-reducing efficacy of CER-001 [44].

Despite the previous setbacks, CER-001 has shown therapeutic potential in familial LCAT deficiency in two compassionate use cases. The patients in both cases received 10 mg/kg CER-001 infusions 3 times per week for 3 weeks, followed by 10 mg/kg twice per week for 3 weeks, and then 10 mg/kg weekly infusions for 6 weeks. In one case, CER-001 treatment was shown to slow down the deterioration of kidney functions and reduce lipid deposits in kidneys [45]. In another case, CER-001 stabilized the kidney functions of the patient and produced long-lasting improvement in the patient's visual function [46]. With the promising clinical data, CER-001 received the Orphan Drug Designation (ODD) from FDA in 2022 to treat LCAT deficiency presenting as kidney dysfunction and/or ophthalmologic disease [47].

The developer of CER-001 has been exploring more therapeutic applications in recent years. Currently, a Phase 2a study is ongoing to investigate the protective effects of CER-001 on septic patients at high risk of developing acute kidney injury [48]. Interim results reported the positive effects of CER-001 in reducing inflammatory cytokines [49]. In another Phase 2 trial, ^{89}Zr-labeled CER-001 showed accumulation in tumors of patients with esophageal cancer, suggesting the potential application of CER-001 as an imaging reagent or drug delivery platform [50]. The potential benefits of CER-001 in COVID-19 were also proposed, although more data are needed to investigate the therapeutic effects in clinical settings [51].

1.1.3 Emerging trends for next-generation sHDL products

As discussed above, while current sHDL candidates showed potent cholesterol mobilization effects and safety profiles, their therapeutic efficacy is not as prominent as expected. The sub-optimal results could be attributed to several conceptual and

methodological limitations of current sHDL products. Conceptual-wise, current sHDLs mainly focus on elevating HDL-c levels, while other aspects, such as anti-inflammation and endothelium-regulation functions, were omitted. However, there is increasing recognition that HDL functionality, instead of HDL-c levels, is the better indicator of the protective effects of HDLs, demanding a paradigm shift for HDL replacement therapy from elevating HDL-c levels to enhancing sHDL functionalities [52-54]. Methodological-wise, the formulation development was severely limited by regulatory challenges with the lack of FDA-approved phospholipids and proper characterization methods. With the recent advances in other lipid-based drug products, significant progress has been made to address these technical problems, making it possible to formulation sHDLs with novel protein or lipid components. sHDLs with more sophisticated formulation designs and tailored functions would be the future direction for sHDL therapies.

1.1.3.1 Formulation innovations

ApoA-1 mimetic peptides: Full-length ApoA-1 protein, which is purified from human plasma or manufactured using recombinant technology, is exclusively used in current sHDL products [30, 35]. However, safety and scalability concerns involved in the manufacture and formulation of full-length ApoA-1 pose challenges in the clinical translation of sHDL products. Complex and time-consuming purification processes are needed to remove other plasma components, viruses, host cell proteins, endotoxins, and other impurities [55]. Failure to remove impurities can trigger the immune response and cause adverse effects [56]. ApoA-1 may undergo modifications in the purification process, resulting in dysfunctional ApoA-1 proteins [56]. Additionally, surface surfactants such as cholate are required to assemble full-length ApoA-1 to sHDL, which

can lead to adverse effects if not fully removed. Such complex manufacturing and formulation processes limit the large-scale production of sHDL.

In recent years, several ApoA-1 mimetic peptides have been developed to address the above problems [57, 58]. Compared to full-length ApoA-1, ApoA-1 mimetic peptides could be synthesized on a large scale without requiring extensive purification. Moreover, ApoA-1 mimetic peptides readily complex with phospholipids, which significantly simplifies the manufacturing process [58, 59]. The increasing understanding of the structure-activity relationship of ApoA-1 allows the optimization of ApoA-1 mimetic peptides focusing on different functions. For example, to avoid the recognition of anti-ApoA-1 autoantibodies, Pagano et al. designed an ApoA-1 mimetic peptide with an altered C-terminal alpha-helix which is the major binding site for anti-ApoA-1 [60]. The optimized ApoA-1 mimetic peptide was shown to inhibit the pro-inflammatory cytokine production induced by anti-ApoA-1 IgG [60].

Incorporation of bioactive lipids: In contrast to the simple composition of sHDLs, endogenous HDLs present highly diverse and dynamic lipidome profiles with more than 200 lipid species identified [2, 61]. The type and content of lipids in HDLs have significant impacts on the functionalitiy of HDLs. For example, HDL-associated sphingosine-1-phosphate exerts potent anti-inflammatory and endothelial protective functions via activating $S1P_1$ signaling pathways [62, 63]. Anionic phospholipids, such as phosphatidylinositol (PI), phosphatidic acid (PA), and phosphatidylserine (PS), have also been shown to be associated with the protective functions of HDLs [64]. Notably, a strong positive correlation was found between PS abundance and HDL functions such as cholesterol efflux, anti-inflammation, and anti-oxidation capacities [64]. As PS has

long been recognized as an anti-inflammatory signaling lipid involved in apoptosis and phagocytosis processes, it was hypothesized that introducing PS could increase the therapeutic effects of sHDLs [65, 66].

1.1.3.2 Broader therapeutic application of sHDLs

Historically, the development of sHDL has been focused on treating cardiovascular diseases. However, increasing studies showed that abnormal HDL levels and dysfunctional HDLs are prevalent in a broad array of diseases. By tuning peptide and lipid components, sHDLs could be optimized to exert diverse protective functions tailored to various therapeutic applications.

***Infectious diseases*:** Low HDL cholesterol (HDL-C) has been reported as a predictive factor for poor outcomes in various infections [67-69]. For example, previous research in our lab showed that the HDL-C levels are reduced by 40-70% in septic pneumonia patients compared to non-septic controls, and that HDL-C levels on the first day in ICU are predictive of overall patient survival [70, 71]. In the cecal ligation and puncture (CLP)-induced sepsis mouse model, administration of sHDL normalized body temperature, reduced pro-inflammatory cytokine levels, and restored endothelial integrity, which led to the improved survival rates of the sHDL-treated group [72]. In the Phase 2a clinical trial of CER-001, administration of 5, 10, or 20 mg/kg of CER-001 twice daily was reported to improve the inflammation biomarkers and endothelial functions in septic patients [49]. The therapeutic mechanisms of sHDLs in infectious diseases could include the neutralization of endotoxins, normalizing endothelial functions, modulating inflammatory responses, and, in some cases, interfering with virus entry by modulating membrane cholesterol contents [72, 73]. Thus, optimizing the

functionality of sHDLs to treat inflammatory diseases would be a promising direction to future sHDL development.

***Autoimmune diseases*:** Decreased HDL level is commonly observed in patients with autoimmune diseases such as systemic lupus erythematosus (SLE) and rheumatic arthritis [74, 75]. Moreover, HDLs isolated from patients with autoimmune diseases present abnormal proteomic and lipidomic profiles, rendering dysfunctional HDLs with impaired cholesterol efflux, anti-inflammatory, and anti-oxidant effects [74, 76]. sHDLs have been shown to successfully rescue the quantity and quality of HDLs in lupus and rheumatic arthritis models. For example, administration of ETC-642, an HDL mimetic composed of an ApoA-I mimetic peptide and phospholipid, significantly decreased the TNF-α and IL-6 levels on NZM2328 lupus mouse models [77]. Infusion of ApoA-1 or sHDLs was also found to reduce joint inflammation in PG-PS induced arthritis rat model [78]. Further investigations to understand the immunomodulation mechanisms of HDLs will advise optimization of the sHDL composition for autoimmune disease treatment.

Cancer: sHDLs can be formulated to encapsulate various therapeutic agents, including hydrophobic and amphiphilic small drug molecules, proteins, and nucleic acids, making them a versatile drug delivery platform [28]. Moreover, the interaction between sHDLs and SR-BI enables an active targeting of sHDLs to SR-BI overexpressing cancer cells [79, 80]. Indeed, the recent Phase 2 clinical trial of CER-001 on patients with esophageal cancer showed the accumulation of CER-001 in tumor tissues [50]. Such evidence encourages further investigations on sHDLs as drug delivery systems for cancer therapy.

Other emerging therapeutic applications: In addition to disease areas discussed above, sHDLs therapies have been proposed for neuronal disorders, including Alzheimer's disease [81] and ischemic strokes [82], lipid storage disorders such as Niemann-Pick diseases [83], and ocular diseases such as age-related macular degeneration [84]. With the increasing understanding of the functions of endogenous HDLs in physiological and disease conditions and the structure-activity relationship of HDLs, the therapeutic applications of sHDLs are expected to be further expanded in the future.

1.1.4 Research scope and overview of Chapters 2 and 3

Chapters 2 and 3 are focused on developing sHDLs with enhanced functions. As the activated endothelium is both the therapeutic target and delivery barrier for sHDLs, in Chapter 2, a VCAM-1 specific ligand was introduced to sHDLs to allow an active targeting of sHDLs to activated endothelial cells. The active targeting efficiency was investigated *in vitro* and *in vivo*. The impacts of the introduction of the targeting ligand on the therapeutic effects of sHDLs were evaluated. In Chapter 3, the bioactive phosphatidylserine (PS) was incorporated into sHDLs. The effects of PS incorporation on particle characteristics, cholesterol efflux capacity, anti-inflammatory effects, pharmacokinetics, and pharmacodynamic profiles of sHDLs were systematically investigated. Overall, the knowledge derived in Chapters 3 and 4 may facilitate the optimization of sHDL formulation and functionalities to treat varieties of inflammatory diseases.

Chapter 2 was published in *Frontiers in Pharmacology*. The manuscript for Chapter 3 will be submitted for publication shortly after the dissertation defense.

1.2 Analytical characterization of liposomal products: regulatory challenges

Liposomes are a group of lipid-based vesicles characterized by one or more aqueous compartments separated by one or more phospholipid bilayers. The lipid membrane and enclosed aqueous chamber in liposomes enable the encapsulation of both hydrophobic and hydrophilic therapeutic agents, making liposomes a highly adaptable drug delivery platform [85]. Compared to traditional dosage forms, liposomes showed numerous advantages, including prolonging the circulation time of the drug, enhancing biodistribution in target tissues, and reducing systemic toxicity [85]. Since the FDA approval of the first liposomal product, Doxil®, in 1995, more than a dozen of liposomal drug products have been approved in the US, with more candidates in clinical trials [86].

Analytical characterization is of vital importance for formulation development, regulatory filing, and quality control of liposomal products. The complex compositions, unique structure, and complicated structure-activity relationship of liposomes, however, create a great challenge for the identification and assessment of critical quality attributes (CQAs) to developers as well as regulatory agencies [87]. In 2018, the FDA published a guidance document on liposomal product development to facilitate the new drug application (NDA) or abbreviated new drug application (ANDA) for liposome drug products [88]. For most liposomal products in the nanoparticle range, the FDA Guidance for Industry on drug products containing nanomaterials also provides recommendations on analytical characterizations [89]. The analytical characterization methods of CQAs identified in these guidances were summarized below. The unaddressed regulatory challenges are also discussed.

1.2.1 Analytical characterization of liposomal products

1.2.1.1 Total and encapsulated drug contents

While total drug content can be conveniently determined using chromatography techniques, determining drug encapsulation requires the separation of unencapsulated drug from liposomes. Various separation methods, such as ultracentrifugation, ultrafiltration, and dialysis, could be used to isolate unencapsulated drugs from liposomes [87]. The unencapsulated and encapsulated drug are then quantified by chromatography or other techniques to calculate encapsulation efficiency [79]. It is worth noting that factors like mechanical stress or drug adsorption involved in the separation process may cause inaccurate results [89]. Thus, careful validation is needed to ensure the reliability of separation methods.

The drug encapsulated in liposomes may present different physical states such as solution, amorphous precipitate, or nanocrystals [80]. The physical form of encapsulated drugs affects drug dissolution in the inner water phase, which would impact the drug release kinetics of the liposomes. Microscopy techniques such as cryogenic transmission electron microscopy (Cryo-TEM) are commonly used to observe the physical state of encapsulated drugs [81]. For example, the encapsulated drug in Doxil® forms rod-like doxorubicin-sulfate nanocrystals, resulting in the coffee-bean-like shape of liposomes [90]. Differential scanning calorimetry (DSC) can also be used to evaluate the crystallinity of encapsulated drugs in liposomal products such as Doxil® and Ambisome® [82, 83]. Other techniques such as small/Wide angle X-ray scattering (SAXS/WAXS), circular dichroism (CD) spectroscopy, and nuclear magnetic resonance

(NMR) have also been reported to characterize physical forms of encapsulated drugs [80].

1.2.1.2 Lipid content

The lipid components in liposomes are commonly quantified using liquid chromatography (LC) and LC coupled with mass spectrometry (LC-MS). The impurities which may be introduced in the manufacturing process and possible degradation species should also be identified and measured [88].

1.2.1.3 Particle size

Dynamic light scattering (DLS) is a commonly used technique to characterize particle size and distribution of liposomes. While DLS allows a quick measurement with simple sample preparation, some limitations may cause inaccurate results [91]. DLS assumes a spherical particle shape to calculate particle shape, which may not be true for some liposomal products [89, 92]. The low resolution of DLS could also limit its use when measuring polydisperse samples [91]. DLS results are affected by various measurement parameters, such as particle concentration, the composition of dispersion media, temperature, optical parameters of media and particles, scattering angle, and laser wavelength [92]. Thus, DLS measurement parameters should be carefully recorded and reported to ensure the quality and reproducibility of the measurement [92].

Transmission electron microscopy (TEM) can be used to directly visualize the size of liposomes. However, the staining and drying process involved in the sample preparation may lead to changes in particle size and morphology [93]. Alternatively, cryogenic-transmission electron microscopy (cryo-TEM) avoids such drawbacks of

TEM. However, the limited number of analyzed particles and time-consuming data analysis could pose challenges for cryo-TEM analysis [94].

Recently, asymmetric-flow field-flow fractionation (AF4) has gained increasing interest. Separating particles based on their diffusion coefficients in aqueous buffers, AF4 allows a gentle separation of nanoparticles of different sizes [95]. Moreover, when coupled with varieties of online detectors, AF4 could provide extensive information on size-dependent properties (e.g. drug encapsulation) [96, 97].

Other techniques, such as size exclusion chromatography (SEC) and nanoparticle tracking analysis (NTA), are also commonly used to evaluate the particle size distribution of liposomes [87]. With the different advantages and drawbacks of different techniques, complementary methods are recommended by regulatory agencies for particle size characterization [89].

1.2.1.4 Net charge and surface properties

Surface charge and surface modifications such as PEGylation have significant impacts on the pharmacokinetics, immunogenicity, and efficacy of liposomal products [86]. Electrophoretic light scattering is commonly used to measure the zeta potential of liposomes [91]. Results of zeta potential derived from electrophoretic light scattering are significantly affected by parameters including pH, ionic strength, and particle concentrations. Thus, similar to DLS, the measurement parameters of electrophoretic light scattering should be meticulously recorded [92].

Cryo-TEM was used to visualize the PEG layer on the Doxil liposomes [90]. Limited studies have been published on other characterization methods for the surface modification of liposomes.

1.2.1.5 Particle morphology, lamellarity, and inner structure

The lamellarity and inner structure of liposomes have significant effects on particle stability and drug release kinetics, making them CQAs to liposomal products [86]. The morphology and inner structure of liposomes may be directly observed by several microscopy techniques, including light microscopy, polarization microscopy, fluorescent microscopy, TEM, cryo-TEM, and environmental scanning electron microscopy (ESEM). A comprehensive review of these techniques has been conducted by Robson et al. [98]. In addition to direct observation, the lamellarity of liposomes could also be determined by techniques including ^{31}P-NMR [99], small-angle X-ray scattering (SAXS) [100], and small-angle neutron scattering (SANS) [101].

1.2.1.6 In vitro drug release for liposomal drug products

In vitro drug release study is essential to guide formulation development, facilitate quality control and regulatory filing, and, in the best-case scenario, establish the *in vitro-in vivo* correlation (IVIVC) of liposomal formulations [102]. With no standardized *in vitro* drug release tests (IVRT) method available, the sample-and-separate method and the dialysis-based method are two commonly reported methods for liposomal and other nanoparticle drug products [103]. In the sample-and-separate method, release media containing liposomes is sampled during the release period. The unencapsulated drug in collected samples is separated and quantified to calculate drug release percentages [102]. The sample-and-separation method presents several advantages, including simple experiment setups and straightforward sample processing methods. However, sample processing involved in this method can be time-consuming, and additional mechanical stress imposed on liposomes during the separation process

may risk the leakage of liposomes [89]. Thus, thorough method validation is needed to ensure the separation does not affect drug release.

Dialysis-based assay, where liposomes and released drug molecules are separated by dialysis membranes, is another commonly used method. While such an experimental setup allows for convenient sampling with reduced processing, the diffusion barrier posed by dialysis membranes may delay the translocation of the released drug, resulting in an underestimated drug release rate [103-105].

Several novel techniques have been recently developed for IVRT of liposomal products. For electroactive drugs, electrochemical methods have been developed for the *in situ* measurement of free drug concentrations in release media [106]. With its capacity to isolate particles of different sizes, AF4 is particularly suitable for investigating drug release and transfer in complex biological media such as plasma, making it an appealing strategy for developing physiological relevant IVRT for liposomes [107].

1.2.2 Regulatory challenges onthe analytical characterization of liposomes

1.2.2.1 Identification of CQAs

As defined in ICH Harmonized Tripartite Guideline, Pharmaceutical Development Q8, CQA is defined as “a physical, chemical, biological, or microbiological property or characteristic that should be within an appropriate limit, range, or distribution to ensure the desired product quality” [108]. Some CQAs for liposomal drug products identified by FDA have been discussed above. It is worth noting that the CQAs for liposomal drug products are not one-size-fits-all. Instead, as different liposomal products present unique compositions, structures, and therapeutic applications, CQAs must be identified

case-by-case [109]. As the complex interplay between the physicochemical properties and the *in vivo* performance of liposomes has not fully been revealed, identifying CQAs remains a particularly challenging task [110]. Additionally, there is confusion regarding the role of the regulatory agency and product developers in defining CQAs of liposomal products, which necessitates a more well-defined regulatory process [110].

1.2.2.2 Challenges in developing in vitro drug release test

With the lack of a compendial IVRT method and the diverse structures of liposomes, the *in vitro* release assay method for liposomal products has to be specifically designed to fit the given liposome product. However, there has been no consensus on the proper techniques for IVRT of different liposomal products [102].

Establishing *in-vitro-in-vivo*-correlation is especially difficult for liposomal products. FDA guidance recommended that, preferably, *in vitro* drug release should be conducted in a physiological medium [88]. However, most published IVRTs are conducted in simple buffer conditions, which do not simulate *in vivo* conditions. Designing physiological relevant IVRT is a difficult task, as the complex interactions between liposomes and *in vivo* environments are not fully revealed [111]. Future research on liposomal drug release mechanisms, interaction with *in vivo* environments, elimination process, new mathematical models, as well as novel experimental techniques may help to establish IVIVC for liposomal products [111, 112].

1.2.2.3 Challenges specific to generic product development

With many patents of innovator liposomal products expiring, more and more efforts have been made to develop generic liposomal products. Regulatory agencies require that generic liposomal products should demonstrate Q1 (qualitative) and Q2

(quantitative) sameness as reference listed drugs (RLDs) [88]. Moreover, generic liposomal products are also required to have the same physicochemical properties as RLDs [88]. Thus, robust analytical characterization is of vital importance in demonstrating the pharmaceutical equivalence of generic liposomal products. However, as CQA data of the RLD are usually not disclosed, there is little information available for generic product developers, making it a great challenge to identify the nature and range of CQAs of the liposomal product [110]. To fill this gap, FDA has issued several product-specific guidance with non-binding recommendations on the analytical characterization of selected liposomal products [113], which would provide valuable information to generic product developers.

1.2.3 Summary and Perspective

With the rapid development of novel liposomal drug products and emerging novel analytical techniques, the regulatory framework for liposomal products has been an evolving field. To fill the scientific and regulatory gaps in the development of innovator and generic liposomal products, there has been active collaboration between industry, academia, and regulatory authorities. The new knowledge of the structure-activity relationship and *in vivo* mechanisms of liposomes, novel experimental techniques, and more defined regulatory requirements will help to solve the technical and regulatory challenges in liposomal product development.

1.2.4 Research scope and overview of Chapters 4 and 5

The main goal of Chapters 4 and 5 is to develop analytical methods to ensure the successful formulation development, regulatory filing, and quality control of liposome

formulations. The methodology of dialysis-based drug release was examined in Chapter 4. The barrier effects of the dialysis membrane were quantitatively evaluated, based on which a mathematical model was developed to calculate the 'real' drug release from the apparent drug release data. A good fit between predicted drug release profiles and experimentally determined drug release data was found on the model drug Doxil®. The evaluation method developed in this chapter would be useful for analyzing the methodology of dialysis-based drug release assays.

Chapter 5 focused on the analytical characterization of a multivesicular liposomal product, Exparel. Analytical methods are established to characterize CQAs of Exparel identified in the FDA product-specific guidance, including drug and lipid contents, particle size and structure, residual solvents, and pH. In addition, a rotator-based, sample-and-separate IVRT was developed for formulation comparison and quality control purposes. The batch-to-batch variability of Exparel was examined by the established analytical methods. The knowledge derived from this chapter may facilitate the development of generic multivesicular liposomes.

Chapter 4 was published in *Journal of Controlled Release*. Chapter 5 will be submitted to the *AAPS Journal* with some modifications after the defense.

Chapter 2 Development of Activated Endothelial Targeted High-Density Lipoprotein Nanoparticles

2.1 Abstract

Endothelial inflammation is an important pathophysiological driving force in various acute and chronic inflammatory diseases. High-density lipoproteins (HDLs) play critical roles in regulating endothelial functions and resolving endothelial inflammation. In the present study, we developed synthetic HDLs (sHDLs) which actively target inflamed endothelium through conjugating vascular cell adhesion protein 1 (VCAM-1) specific VHPK peptide. The active targeting of VHPK-sHDLs was confirmed *in vitro* on TNF-α activated endothelial cells. VHPK-sHDLs presented potent anti-inflammatory efficacies *in vitro* through the reduction of proinflammatory cytokine production and inhibition of leukocyte adhesion to activated endothelium. VHPK-sHDLs showed increased binding on inflamed vessels and alleviated LPS-induced lung inflammation *in vivo*. The inflamed endothelium-targeted sHDLs may be further optimized to resolve endothelial inflammation in various inflammatory diseases.

2.2 Introduction

Inflammation is a common denominator in the pathophysiology of a broad array of diseases, including atherosclerosis, sepsis, and autoimmune diseases [114-116]. The

vascular endothelium plays important roles in the initiation and progression of inflammation [117-120]. Various stimuli in inflammatory diseases, such as endotoxins, mechanical stress, oxidative stress, and circulating proinflammatory cytokines, could convert endothelial cells from a resting state to an activated state [12, 121-123]. Activated endothelial cells produce proinflammatory cytokines and chemokines, recruiting leukocytes such as monocytes and neutrophils to the site of inflammation [124]. At the same time, activated endothelial cells express adhesion molecules, including selectins, intercellular adhesion molecule-1 (ICAM-1), and vascular cell adhesion molecule-1 (VCAM-1), which enables cellular adhesion and migration of recruited immune cells [125, 126]. In the case of inflammatory diseases, the inflammation often remains unresolved due to dysregulated inflammatory responses. The unresolved inflammation creates a vicious cycle of persisting endothelial activation, recruitment of immune cells, inflammatory responses, and tissue damage [127, 128]. Breaking such a cycle by alleviating endothelial activation and inflammation would be a potential treatment strategy for inflammatory diseases [129, 130].

High-density lipoproteins (HDLs) are a group of lipoproteins mainly composed of esterified and free cholesterol, phospholipids, and apolipoproteins which predominately involve ApoA-1 and ApoE [1]. As a major player in maintaining cholesterol homeostasis, HDLs induce cholesterol efflux from peripheral cells by interacting with various receptors on cell membranes such as ATP-binding cassette transporter A1 (ABCA-1), ATP-binding cassette transporter G1 (ABCG-1), and scavenger receptor BI (SR-BI). HDLs also play crucial roles in regulating inflammation responses and endothelial functions [53], which can be dependent or independent of the cholesterol mobilization

effects of HDLs [7, 8]. For example, it was found that through ABCA1 efflux, HDLs modulate the cholesterol content of lipid rafts, inhibiting the trafficking of Toll-like receptor 4 (TLR-4) to cellular membranes and inhibiting the activation of downstream inflammation pathways [9]. The lipid raft disruption caused by cholesterol efflux could also inhibit the translocation of NADPH oxidase 4 (NOX-4), inhibiting the generation of reactive oxygen species (ROS) [131]. Through binding with SR-BI, HDLs activate the phosphatidylinositol-3-kinase-protein-kinase-B (PI3K-AKT) pathway and mitogen-activated protein kinase (MAPK) pathway. Such kinase cascade activation stimulates endothelial nitric oxide synthase (eNOS) and increases nitric oxide (NO) production [132, 133]. In terms of cholesterol efflux independent anti-inflammatory mechanisms, HDLs could effectively neutralize lipopolysaccharide (LPS) and lipoteichoic acid (LTA) during bacteria infection, reducing LPS- and LTA-induced inflammatory responses [11]. Overall, HDLs have been shown to reduce the expression of adhesion molecules, alleviate intracellular oxidative stress, prevent endothelial cell apoptosis, and inhibit the secretion of proinflammatory cytokines on activated endothelial cells [134-136]. Such anti-inflammation and endothelial protective functions of HDL make it an appealing treatment option for inflammatory diseases.

Inspired by endogenous HDLs, various synthetic HDLs (sHDLs) composed of lipids and ApoA-1 or ApoA-1 mimetic peptides have been developed [57]. Several sHDL candidates, such as CSL112, CER-001, and ETC 642, have entered clinical trials [34, 40, 138] and showed favorable safety profiles. It is worth noting that the current sHDL therapies were originally designed for atherosclerosis treatment [139]. As a result, the formulation development was mainly focused on optimizing the reverse cholesterol

transport capacities of sHDLs to reduce atheroma plaques. However, in recent years, there has been a growing interest in broadening the therapeutic applications of sHDL products to other inflammatory diseases, including sepsis, COVID-19, and autoimmune diseases [72, 74, 140]. Thus, additional focus has been put on optimizing the anti-inflammatory and endothelial protective functions of sHDLs.

Among the variety of adhesion molecules on inflamed endothelium, VCAM-1 has recently received much research interest as a biomarker and targeting site for inflamed endothelium. Expressed in inflamed endothelium, VCAM-1 enables cell adhesion through binding with very late antigen-4 (VLA-4) expressed on the surface of leukocytes and lymphocytes [141]. One VLA-4 mimicking peptide, VHPKQHR, was found to have high binding efficiency with VCAM-1 in phage display studies [142]. Various peptides with the VHPKQHR motif (VHPK peptides) have since been widely used in developing inflamed endothelial targeting imaging agents and drug delivery systems [143]. In the present study, a VHPK peptide is conjugated to sHDLs. It is hypothesized that the conjugation of the targeting peptide would enable an active targeting of sHDLs to activated endothelial cells, increasing the distribution of sHDLs on inflamed endothelium and enabling stronger inflammation resolution effects. To test this hypothesis, the endothelial targeting efficiency and anti-inflammatory effects of VHPK-sHDLs were examined *in vitro.* The *in vivo* targeting effect of VHPK-sHDLs to inflamed endothelium was further examined using intravital microscopy. As a proof-of-concept experiment, an LPS-induced lung inflammation model was used to evaluate the anti-inflammatory effects of VHPK-sHDLs *in vivo*.

2.3 Materials and methods

2.3.1 Materials

ApoA-1 mimetic 22A peptide (PVLDLFRELLNELLEALKQKLK) was synthesized by Genscript Inc. (Piscataway, NJ). VHPK peptide (VHPKQHRGGSKGC) and scrambled peptide (QRHPHVKGGSKGC) were synthesized by RS Synthesis LLC (Louisville, KY) and GeneMed Biotechnologies Inc (South San Francisco, CA). 1,2-dimyristoyl-sn-glycero-3-phosphocholine (DMPC) was purchased from NOF America Corporation (White Plains, NY). 1,2-dioleoyl-sn-glycero-3-phosphoethanolamine-N-[3-(2-pyridyldithio)propionate] (DOPE-PDP) was purchased from Avanti Polar Lipids (Alabaster, AL). LPS from Escherichia coli O111 (L2630):B4 was purchased from Sigma. Recombinant human TNF-α and mouse VCAM-1/CD106 antibody (AF643) were purchased from R&D Systems (Minneapolis, MN). Human VCAM-1 antibody (ab134047) was purchased from Abcam (Waltham, MA). 1,1′-dioctadecyl-3,3,3′,3′-tetramethylindodicarbocyanine (DiD) and 3,3′-dioctadecyloxacarbocyanine perchlorate (DiO) were obtained from Thermo Fisher Scientific (Waltham, MA). Mouse IL-6, mouse MCP-1, human IL-6, human IL-8, human IL-1β, and human TNF-α ELISA kits were purchased from Invitrogen (Waltham, MA).

2.3.2 Cell culture

Human umbilical vein endothelial cells (HUVEC) from pooled donors were purchased from Lonza (Cat #: C2519A, Morristown, NJ). Cells were cultured in EGM-2 complete media (Lonza). HUVEC cells were between passages 3-7 for all experiments. THP-1 cells were obtained from the American Type Culture Collection (ATCC) (Cat#

TIB-202) and kept in RPMI-1640 media supplemented with 10% fetal bovine serum (FBS), 1% Penicillin-Streptomycin (10,000 U/mL), and 0.05 mM 2-mercaptoethanol. J774.A1 cells were cultured in DMEM media supplemented with 10% fetal bovine serum (FBS) and 1% Penicillin-Streptomycin (10,000 U/mL). All cells were cultured in a 37 °C incubator with 5% CO_2.

2.3.3 Synthesis of peptide-DOPE conjugates

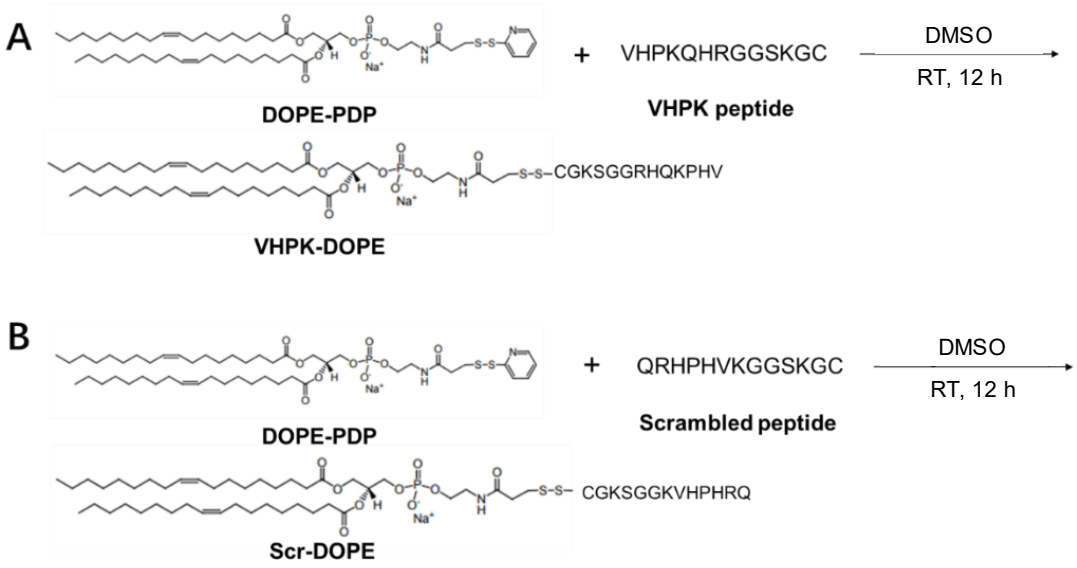

Figure 2.1 Synthesis of VHPK-DOPE (A) and Scr-DOPE (B) conjugates.

Peptide-DOPE conjugates were synthesized as described previously with slight modifications as shown in **Figure 2.1** [144]. Briefly, VHPK or scrambled peptide was reacted with DOPE-PDP (peptide:DOPE-PDP n:n = 1:1.5) in anhydrous DMSO for 12 h. To determine the conjugation efficiency, the unreacted DOPE-PDP content at the end of the reaction was quantified on an ultra-performance liquid chromatography-mass spectrometry (UPLC-MS) with a hydrophilic interaction liquid chromatography (HILIC)

column. The mobile phase consisted of (A) water with 0.1% formic acid (FA), (B) acetonitrile with 0.1% FA, (C) methanol with 0.1% FA, and (D) 100 mM ammonium formate water solution. The flow rate was 0.4 ml/min. The samples were eluted in a gradient with 47.5% B, 47.5% C, and 5% D as initial conditions, which changed to 17% A, 17% B, 39% C, and 5% D in 2 min. DOPE-PDP was detected in a positive mode at m/z = 941.81. The conjugation percentage was calculated by unreacted DOPE-PDP concentrations in the reaction mixture before and after conjugation.

2.3.4 Preparation and characterization of VHPK-sHDLs

The unconjugated, non-targeted sHDLs (NT-sHDL) were prepared by the lyophilization-rehydration method. DMPC and 22A were dissolved and mixed in acetic acid in a weight ratio of 2:1, followed by lyophilization. The lyophilized powder was then rehydrated by PBS (pH 7.4), followed by 3 thermocycles with 5 min incubation at 37 °C and 5 min ice bath for each cycle. The purity of the prepared sHDL was analyzed on a Tosoh TSK gel G3000SWxl column with a PBS flow rate of 1 mL/min and UV detection at 220 nm. For fluorescently labeled sHDLs, DiD or DiO was added to DMPC and 22A mixture prior to lyophilization.

The VHPK-DOPE conjugate (VHPK-DOPE) or scrambled peptide-DOPE conjugate (Scr-DOPE) were then added to NT-sHDLs with a DOPE:total lipid molar ratio of 1:20, followed by 2 h incubation at room temperature under shaking. The resulting VHPK peptide conjugated sHDL (VHPK-sHDL) or scrambled peptide conjugated sHDL (Scr-sHDL) were purified by 7k MWCO Zeba^{TM} spin desalting columns (Thermo Scientific, Waltham, MA). To determine the percentage of VHPK-DOPE inserted to sHDLs, VHPK-DOPE contents before and after desalting were quantified by UPLC-MS

with an ACQUITY UPLC BEH300 C4 column. The mobile phase consisted of (A) water with 0.1% FA, (B) acetonitrile with 0.1% FA, and (C) methanol with 0.1% FA. The flow rate was 0.3 ml/min. The samples were analyzed with a gradient elution of A:B:C of 85:10:5 to 7:62:31 during 0–7 min, followed by an isocratic elution during 7–9 min, and a gradient of A:B:C of 7:62:31 to 85:10:5 during 9–11 min. VHPK-DOPE was detected in a positive mode at m/z = 741.3. The insertion percentage was calculated by dividing VHPK-DOPE content after the desalting process by the total amount of VHPK-DOPE before desalting.

The particle size and zeta potential of different sHDLs were determined by dynamic light scattering (DLS) on a Malvern Zetasizer Nano ZSP (Westborough, MA). The particle size distribution was measured in PBS with a 22A concentration of 1 mg/ml. Zeta potential was measured with a 22A concentration of 0.1 mg/ml in 10 mM phosphate buffer. To assess the morphology of different sHDLs, samples were loaded on a carbon film-coated 400 mesh copper grid from Electron Microscopy Sciences (Hatfield, PA), followed by negatively stained with 1% (w/v) uranyl formate and dried. The samples were imaged with 100kV Morgagni transmission electron microscopy (TEM) with a Gatan Orius CCD.

2.3.5 Cytotoxicity evaluation

HUVEC cells were seeded to 96-well plates at a density of $1x10^4$ cells/well and cultured overnight. Cells were incubated with different sHDLs at indicated 22A concentrations for 24 h. The cell viability was then determined using CellTiter 96® AQueous One Solution Cell Proliferation Assay according to the protocol provided by the manufacturer.

2.3.6 Cellular binding assay

HUVEC cells were seeded to 12-well plates and cultured to reach confluence before experiments. Endothelial inflammation was induced by pretreatment of TNF-α at 2 ng/ml for 8 h. Cells were fixed with 2% paraformaldehyde (PFA) for 15 min, followed by incubation with DiD-labeled sHDLs at a 22A concentration of 5 μg/ml for 30 min. The fluorescent intensity was determined by flow cytometry. For confocal microscopy imaging, HUVECs were seeded to 4-well chamber slides and cultured to reach confluence. The cells were fixed with 2% PFA at 4°C for 30 min, washed with PBS, and incubated with DiD-labeled sHDLs (22A concentration 5 μg/ml) at 37°C for 15 min. For VCAM-1 blocking, cells were pre-incubated with human VCAM-1 antibody at 10 μg/ml for 30 min before incubation of sHDLs. The slides were then washed with PBS, mounted using DAPI-containing mounting media, and imaged using a confocal microscope.

2.3.7 Cholesterol efflux assay

J774.A1 cells were seeded in 24-well plates at a density of 2.5 x 10^5 cells/well and incubated overnight. Cells were then labeled overnight with 1 μCi/ml [^{3}H] cholesterol in DMEM containing 0.3% fatty acid-free bovine serum albumin (BSA) and 5 μg/mL ACAT inhibitor Sandoz 58-035. Cells were then washed with PBS twice and incubated in DMEM containing 0.3% BSA and 5 μg/mL ACAT inhibitor Sandoz 58-035 for 24 h. After being washed with PBS, cells were incubated with different sHDLs for 4 h at 22A concentrations of 5, 10, 25, or 50 μg/mL in DMEM containing 0.3% BSA. At the end of incubation, media was collected, and cells were lysed with 0.1% SDS in 0.1 M NaOH. Radioactive counts in media and cell lysis fractions were measured by liquid

scintillation counting using Perkin Elmer Tri-Carb 2910TR (Waltham, MA). The cholesterol efflux percentage was calculated by dividing the media count by the sum of the media and cell counts.

2.3.8 Anti-inflammatory study

For anti-inflammatory studies on THP-1 derived macrophages, THP-1 cells were seeded to 24-well plates at a density of 2 x 10^5/well. THP-1 cells were incubated with 50 ng/ml phorbol 12-myristate 13-acetate (PMA, Sigma) for 48 h to induce macrophage differentiation. The differentiated, adherent cells were washed with PBS and were allowed to rest in PMA-free media for 24 h. THP-1 derived macrophages were then co-incubated with 100 ng/ml LPS and sHDLs at a 22A concentration of 10, 20, or 50 μg/ml for 12 h. For anti-inflammatory studies on HUVEC cells, HUVEC cells were seeded to 24-well plates at a density of 5 x 10^4/well. After overnight incubation, HUVEC cells were co-incubated with 100 ng/ml LPS and sHDLs at a 22A concentration of 10, 20, or 50 μg/ml for 12 h. At the end of incubation, the cell culture media was collected, and the cytokine concentrations were quantified by ELISA.

2.3.9 Monocyte adhesion assay

HUVEC cells were seeded to 35 mm glass-bottom dishes and cultured until confluent. Cells were treated with 2 ng/ml TNF-α for 16 h to induce inflammatory responses. Cells without TNF-α pretreatment were used as control cells. THP-1 cells were fluorescently labeled by incubating cells with 0.5 uM BCECF-AM in PBS for 30 min. HUVEC cells were then treated with different sHDLs (22A 100 μg/ml) for 1.5 h. Fluorescently labeled THP-1 cells (2 x10^5) were subsequently added to each well. After

0.5 h incubation, the media containing unbound THP-1 cells was discarded. Cells were gently washed with PBS 3 times. Then cells were fixed with 2% PFA, sealed with coverslips, and visualized by confocal microscopy. The numbers of bound THP-1 in 5 random fields were counted for each dish.

2.3.10 Intravital microscope

All animal experiments in the present study were approved by the Institutional Animal Care and Use Committee (IACUC) of the University of Michigan. C57BL/6 mice aged 3 – 4 weeks were obtained from Charles River Breeding Laboratories (Portage, MI). To induce endothelium inflammation, mice were pretreated with LPS (10 mg/kg i.p.) 3 h before sHDL administration. Mice without any treatment were used as the control group. Before imaging, mice were anesthetized with ketamine/xylazine mixture (Ketamine, 100 mg/kg; xylazine, 10 mg/kg) i.p. and placed on a heated stage. The mesentery was carefully exposed on a glass coverslip through a midline laparotomy. The mouse was then positioned on the microscopic stage, and blood flow in mesenteric venules was imaged using Zeiss Axio Observer Z1 Marianas Microscope. DiO-labeled NT-sHDL or VHPK-sHDL was injected i.v. at a 22A dose of 5 mg/kg. The DiO fluorescent signal of the mesentery was imaged at 10-, 30-, and 90-min post-injection of sHDL. The exposure time was kept as 200 ms throughout all imaging. The average fluorescent intensity was quantified by ImageJ.

2.3.11 In vivo biodistribution study

Female C57BL/6 mice aged 6-8 weeks were obtained from Charles River Breeding Laboratories (Portage, MI). Different DiR-labeled sHDLs were administered

i.v. at a dose of 10 mg/kg of 22A, followed by a 10 mg/kg LPS *i.p.* injection. At different time points post-injection, the mice were sacrificed. major organs were extracted and imaged using IVIS.

2.3.12 LPS-induced lung inflammation model

Female C57BL/6 mice aged 6-8 weeks were obtained from Charles River Breeding Laboratories (Portage, MI). Different sHDLs were administered i.v. at a dose of 10 mg/kg of 22A, followed by a 10 mg/kg LPS i.p. injection. 18 h post-treatment, the mice were sacrificed. The lung was perfused with 0.5 ml of 10% formalin injected from the trachea before collection.

For *ex vivo* binding assay, the lung tissues were fixed overnight in 10% formalin at room temperature, and switched to 15% then 30% sucrose in PBS for 24 h in each solution at 4 °C. The tissues were embedded in optimal cutting temperature (OCT) compound and frozen in isopentane in a liquid nitrogen bath. The tissue sections were sliced using a cryostat and stored at −80 °C until use. For *ex vivo* binding studies, sections were thawed at room temperature for 30 min, rehydrated with PBS for 10 min, and blocked with 3% bovine serum albumin (BSA) in PBS with 0.05% Tween-20 (PBST) for 2 h. Then slides were incubated with mVCAM-1 antibody (R&D systems, AF643) in 1% BSA in PBST at 4 °C overnight in a humidity chamber. The slides were washed with PBST three times, followed by incubated with an FITC labeled secondary antibody in 1% BSA in PBST (ThermoFisher, #31509) for 2 h at room temperature in dark. The slides were washed with PBST three times again, and incubated with DiD-labeled NT- or VHPK-sHDL for 2 h (22A concentration 10 μg/ml). The slides were washed three times with PBS. DAPI containing mounting media was added to each slide and the

slides were sealed with coverslips using clear nail polish. Images were acquired with a Zeiss confocal microscope.

For histological evaluations, the lung was fixed with 10% formalin at room temperature for less than 24 h. The tissues were then embedded in paraffin and sectioned for hematoxylin and eosin (H&E) staining and Ly6G immunohistochemistry (IHC) staining. The numbers of $Ly6G^+$ cells in tissue sections were counted using ImageJ. In parallel experiments, blood samples were collected by cardiac puncture at the end of the experiment. Plasma was isolated and stored at -80 °C until analysis. The IL-6 and MCP-1 levels were quantified by ELISA (Invitrogen).

2.3.13 Statistical analysis

Data analysis was conducted using GraphPad PRISM. Statistical significance was determined using a two-tailed unpaired Student's t-test for 2 groups of data or a one-way analysis of variance (ANOVA) followed by Tukey test for data of more than 2 groups. A p-value less than 0.05 was considered statistically significant.

2.4 Results

2.4.1 Preparation and characterization of VHPK-sHDLs

The preparation method for VHPK-sHDLs is illustrated in **Figure 2.2A**. sHDL nanoparticles composed of ApoA-1 mimetic peptide 22A and DMPC was prepared as described previously [145]. VHPK peptide DOPE conjugate (VHPK-DOPE) and scrambled peptide DOPE conjugate (Scr-DOPE) were successfully synthesized with a conjugation efficiency of over 90% (**Figure 2.2B**). By using a post-insertion method,

around 90% VHPK-DOPE or Scr-DOPE was inserted into sHDLs by the end of incubation (**Figure 2.2C**). Insertion of VHPK or Scr-DOPE slightly increased the particle size of sHDLs (**Figure 2.3A**). As both VHPK and scrambled peptides are positively charged, inserting VHPK- or Scr-DOPE to sHDLs slightly increased the surface charge of conjugated sHDLs (**Figure 2.3B**). TEM images showed a uniform particle size distribution of all three sHDL formulations (**Figure 2.3C**).

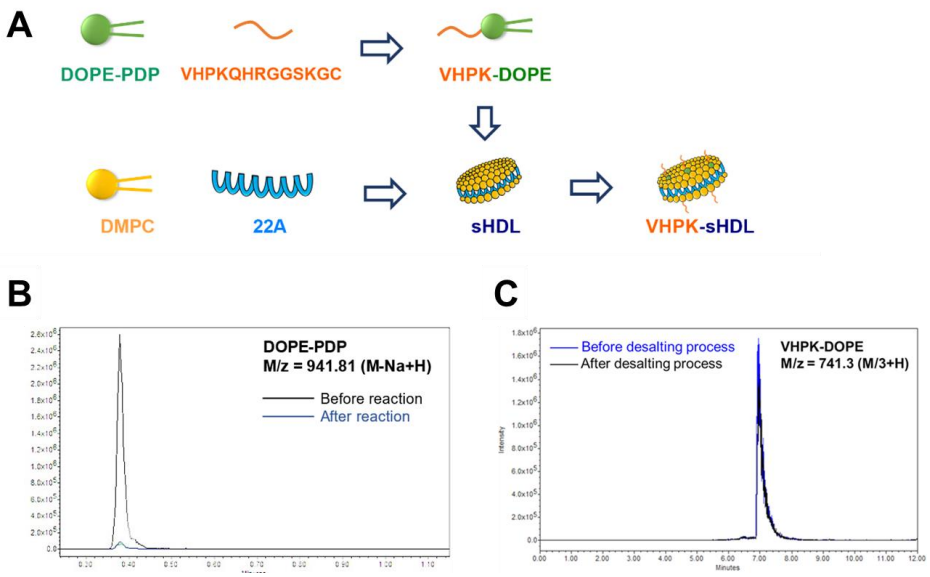

Figure 2.2 (A) Schematic illustration of preparation process of VHPK-sHDLs. LC/MS spectrum showing (B) quantification of unreacted DOPE-PDP before and after conjugation reaction, and (C) quantification of VHPK-DOPE before and after removing uninserted VHPK-DOPE using desalting columns.

2.4.2 Cytotoxicity evaluation

sHDLs have been proved to have a favorable safety profile in previous preclinical and clinical studies [33]. As seen in **Figure 2.4**, both unconjugated and conjugated sHDLs showed minimal cytotoxicity effects with 22A concentrations as high as 100 μg/ml.

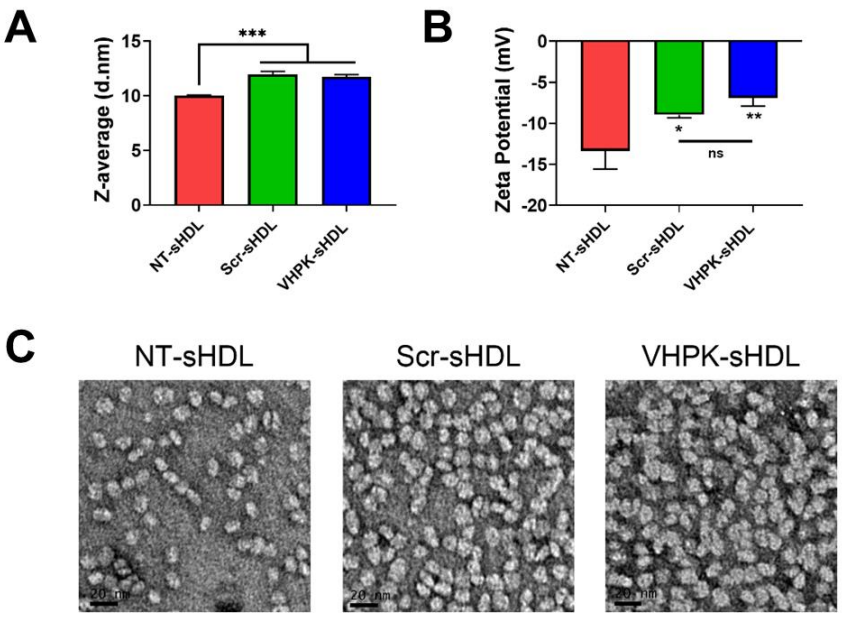

Figure 2.3 Particle size (A) and zeta potential (B) of different sHDLs measured by DLS (n = 3, mean ± SD). (C) Representative TEM images of different sHDLs. Scale bar represents 20 μm. *p<0.05, **p<0.01, ***p<0.05.

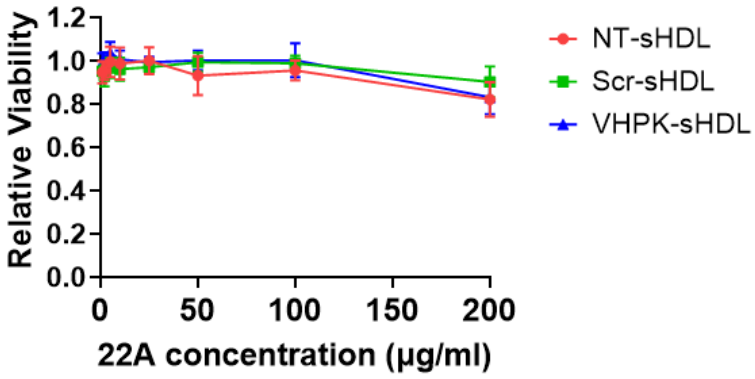

Figure 2.4 Relative cell viability of HUVEC cells incubated with different sHDLs at indicated concentrations. Cells without treatment were used as 100% (n = 6, mean ± SD).

2.4.3 VCAM-1 dependent endothelial targeting in vitro

The cellular binding of different sHDLs was investigated on HUVEC monolayers. HUVEC cells were activated with TNF-α to induce expression of VCAM-1 (**Figure 2.5A**). As shown in **Figure 2.5B and C**, Scr-sHDLs and VHPK-sHDLs showed higher cellular binding on resting HUVEC cells when compared to NT-sHDLs, possibly due to increased non-specific binding caused by the cationic peptide. However, only VHPK-sHDLs showed increased cellular binding on activated HUVEC cells compared to resting cells. Such increased cellular binding was abolished after the binding site of VLA-4 on VCAM-1 was blocked by the pre-incubation with anti-VCAM-1 antibody (**Figure 2.5D**), suggesting the enhanced cellular binding of VHPK-sHDLs is mediated by VCAM-1 in the activated HUVECs.

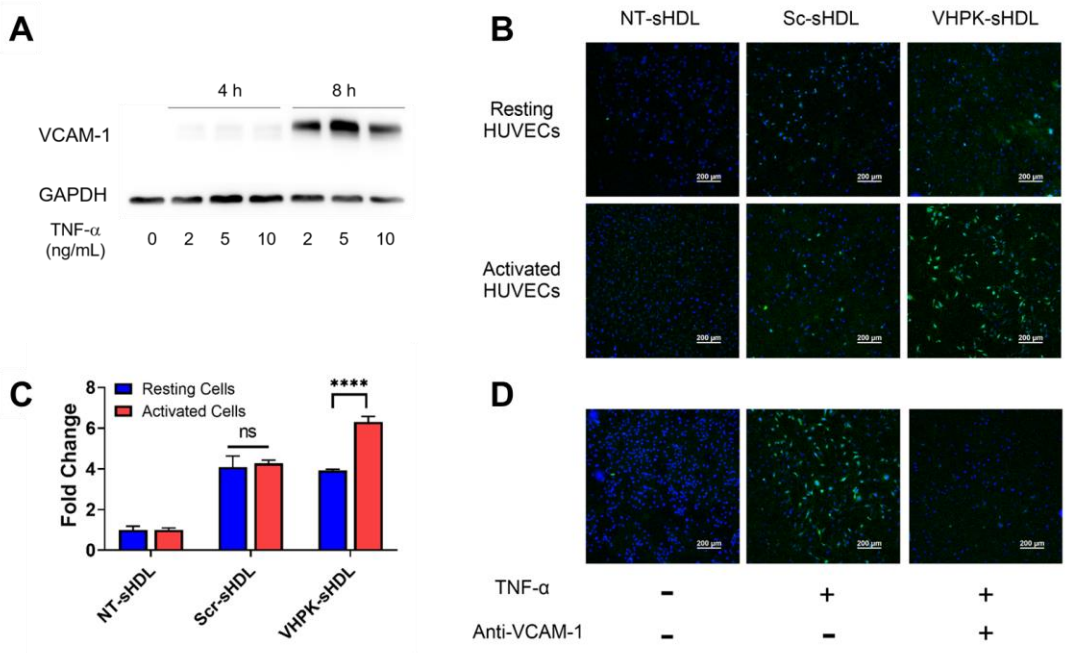

Figure 2.5 (A) VCAM-1 expression on HUVEC cells at different time points after TNF-α activation with different concentrations. Cellular binding of different sHDLs on resting and activated HUVEC cells evaluated by (B) confocal microscope or (C) flow cytometry (n = 3, mean ± SD. ****p<0.001). (D) Representative confocal microscope images of cellular binding of sHDLs on HUVEC monolayers. Blue: Nucleus; Green: DiD-labeled sHDLs.

2.4.4 Cholesterol efflux

As HDL mimetics, sHDLs could efflux cholesterol from peripheral cells [146]. As shown in **Figure 2.6**, a dose-dependent cholesterol efflux effect was confirmed in NT-sHDL, Scr-sHDL, and VHPK-sHDLs. No difference in cholesterol efflux capacity was found in the three kinds of sHDL formulations, suggesting peptide conjugation did not significantly affect the cholesterol efflux capacity of sHDLs.

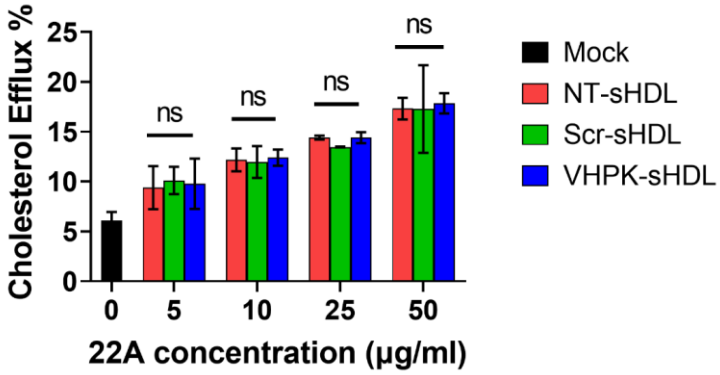

Figure 2.6 Cholesterol efflux capacity of sHDLs on ^{3}H-cholesterol laden J774.A1 cells (n = 3, mean ± SD).

2.4.5 Anti-inflammation effects

The anti-inflammatory effects of different sHDLs were examined on HUVECs and THP-1 derived macrophages. As seen in **Figure 2.7**, both non-targeted sHDLs and peptide conjugated sHDLs showed potent effects in reducing the production of proinflammatory cytokines induced by LPS, suggesting the introduction of targeting peptides did not affect the anti-inflammatory effects of sHDLs.

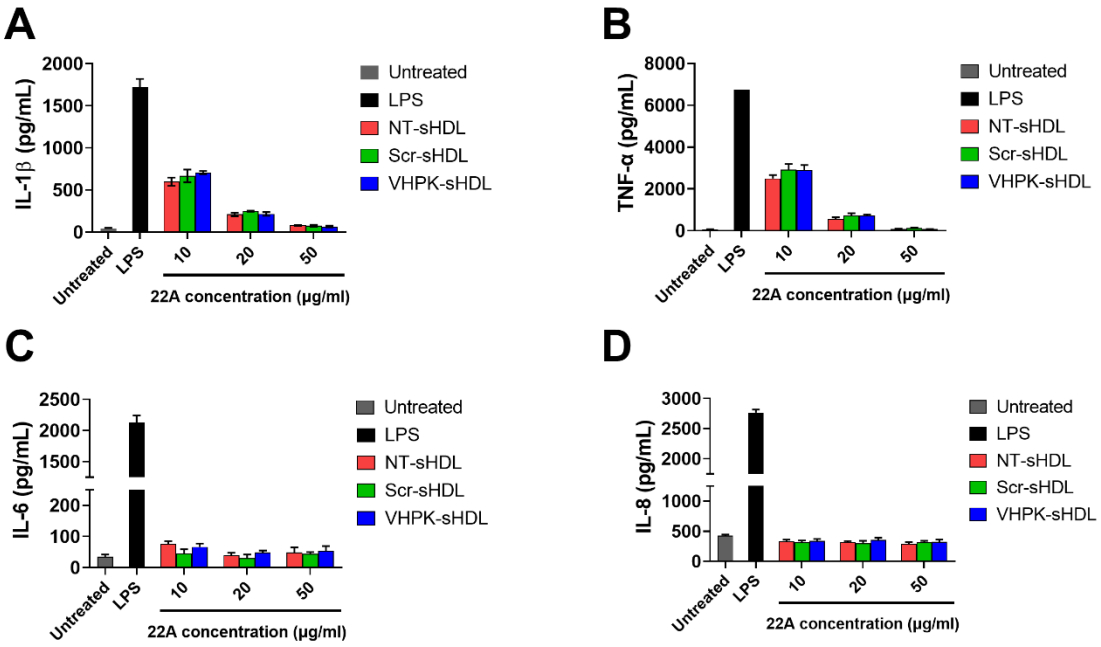

Figure 2.7 IL-1β (A), TNF-α (B), IL-6 (C) and IL-8 (D) levels from THP-1 derived macrophages (A, B) or HUVECs (C, D) after treatment with LPS and different sHDLs. (n = 3, mean ± SD).

2.4.6 Monocyte adhesion on activated HUVEC monolayers

As shown in **Figure 2.8**, TNF-α activated HUVECs greatly increased the cellular adhesion of THP-1 monocytes. Co-incubating NT-sHDL or Scr-sHDL with monocytes did not affect the cellular adhesion of THP-1 cells. VHPK-sHDLs moderately reduced the adhesion/migration of THP-1 cells on the activated HUVEC monolayer. The lack of total blockage of THP-1 on HUVEC monolayers may be attributed to other adhesion molecules mediating THP-1 adhesion and migration such as ICAM-1 [147]. Interestingly, co-incubating VHPK-peptide with monocytes did not affect the monocyte adhesion on activated HUVEC monolayers (data not shown), suggesting the multivalent binding of VHPK-peptide on sHDLs may be essential for the adhesion reduction effects.

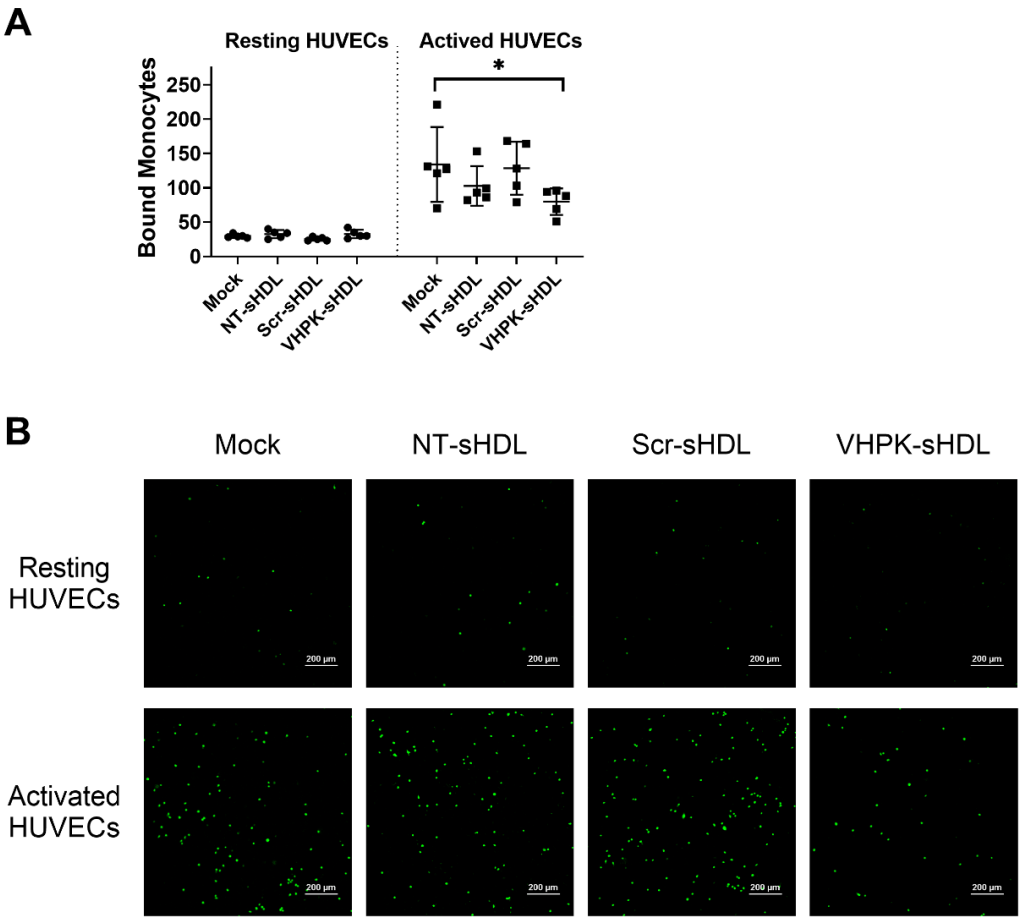

Figure 2.8 (A) Quantification of bound THP-1 monocytes on resting and activated HUVEC monolayers (n = 5, mean ± SD, *p<0.05). (B) Representative images of fluorescently labeled THP-1 monocytes adhered on HUVEC monolayers.

2.4.7 Inflamed endothelial targeting in vivo

The endothelial targeting efficiency of sHDLs with or without the targeting peptide was examined *in vivo* using an intravital microscope. LPS was used to induce general vascular inflammation in mice. As seen in **Figure 2.9**, following *i.v*. injection, VHPK-sHDLs present an enhanced biodistribution on activated endothelium compared to normal vessels, while the biodistribution of NT-sHDL was similar in normal and inflamed endothelium.

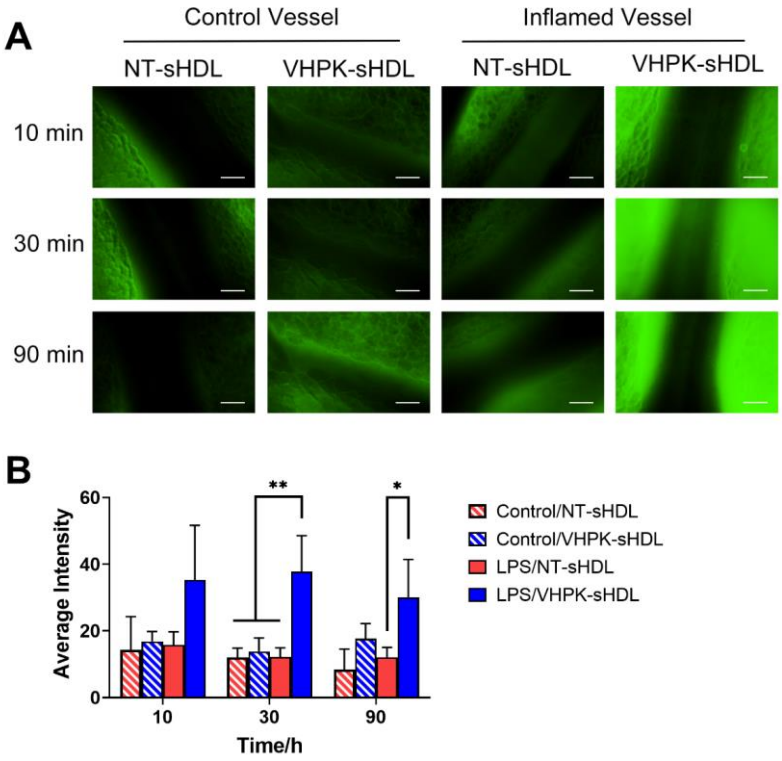

Figure 2.9 (A) Representative intravital microscopy images of the endothelial distribution of NT-sHDLs and VHPK-sHDLs. Scale bar represents 50 μm. (B) Average fluorescent intensity on mice endothelium after administration of different sHDLs. (n = 3, mean ± SD. *p<0.05, **p<0.01.)

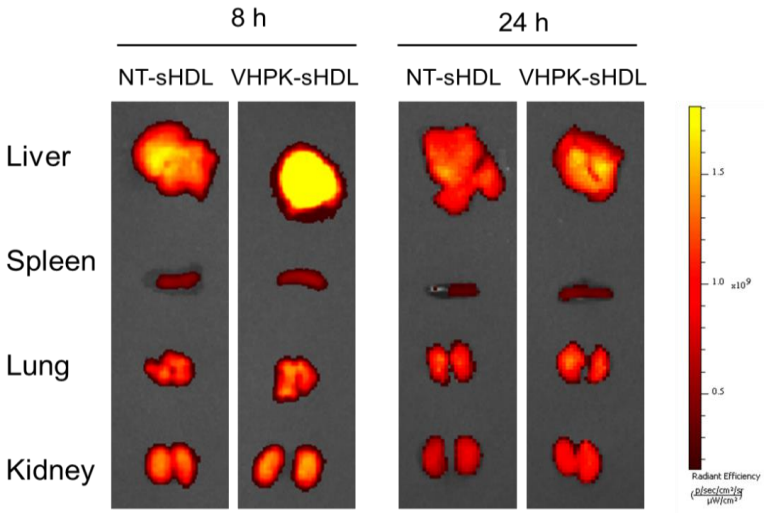

Figure 2.10 Biodistribution of different sHDLs in major organs following *i.v.* injection to LPS-treated mice.

2.4.8 Therapeutic effects of VHPK-sHDL in LPS-induced inflammation model

Vascular endothelial inflammation has different manifestations in different inflammatory diseases. For this proof-of-concept study, a high dose of LPS (10 mg/kg) was injected to induce general endothelial inflammation in mice. A biodistribution study was conducted to examine the organ distribution of different sHDLs following systemic injection. Consistent with our previous studies [145, 146, 148, 149], NT-sHDL and VHPK-sHDLs showed high accumulation in the liver, the primary elimination organ for HDL, as well as organs with large endothelium areas such as lung and kidney (**Figure 2.10**). VHPK-sHDL showed higher signals compared to NT-sHDL, which may be attributed to both increased unspecific binding and active targeting to inflamed endothelium in the liver following systemic LPS injection (**Figure 2.10)**. The lung was chosen as the organ of interest due to its vast endothelium area and well-characterized endothelial dysfunctions including high VCAM-1 expression levels following the LPS challenge. The *ex-vivo* binding assay showed that compared to NT-sHDLs, VHPK-sHDLs presented a higher particle binding as well as a higher co-localization with VCAM-1 on lung tissue sections (**Figure 2.11**), which is consistent with the *in vitro* findings.

As shown in **Figure 2.12B**, while lung tissues from LPS-treated mice presented significant tissue damages manifested by interalveolar septal thickening and interstitial edema, the tissue injury was less affected in NT-sHDL or VHPK-sHDL treated groups. The proinflammatory cytokine levels in plasma were quantified with ELISA. A large intra-group variance was observed, suggesting significant individual differences in LPS tolerance and responses to treatment. Mice treated with VHPK-sHDLs presented lower

plasma MCP-1 levels and showed a trend for lower IL-6 levels in plasma (**Figure 2.12A**). Ly6G$^+$ leukocytes, which are major species of cells to infiltrate in lung inflammation, were stained by immunohistochemistry (IHC). As shown in **Figure 2.12C**, fewer Ly6G$^+$ cells were found infiltrating lung tissues in VHPK-sHDL treated mice than that in NT-sHDL treated groups. While the difference between Ly6G$^+$ counts in VHPK-sHDL treated group and the LPS-treated group was not statistically significant ($p = 0.06$), IHC analysis showed fewer Ly6G$^+$ cells were found bound on the endothelium in VHPK-sHDL treated group, implying the potential for VHPK-sHDL to inhibit leukocyte adhesion and infiltration to inflamed tissues.

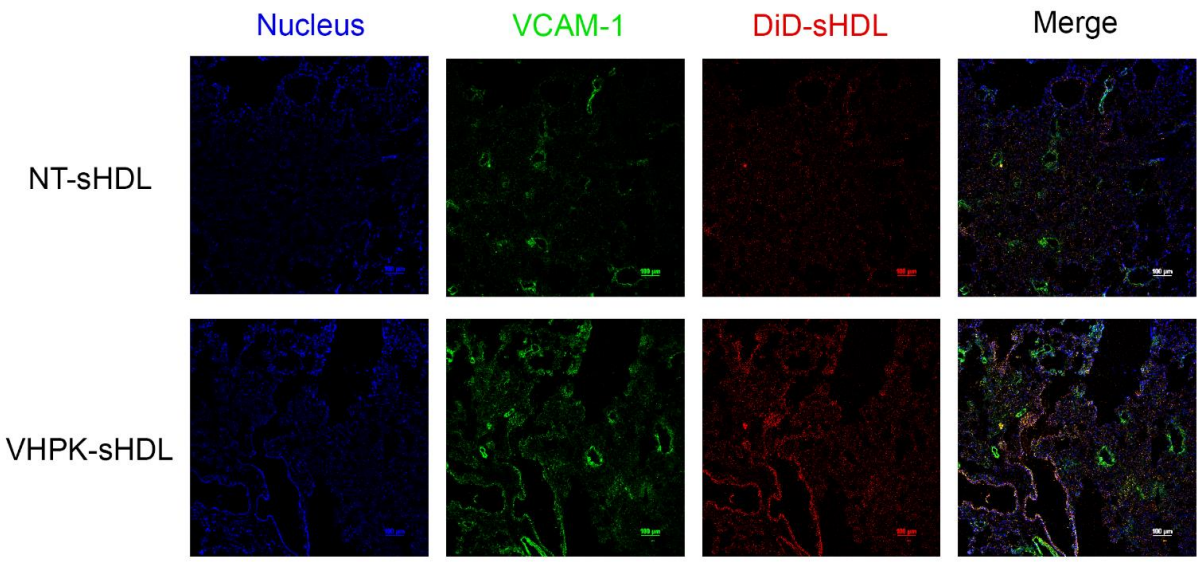

Figure 2.11 Representative confocal microscopy images showing *ex vivo* binding of NT-sHDL and VHPK-sHDL on the lung tissue sections from LPS-treated mice.

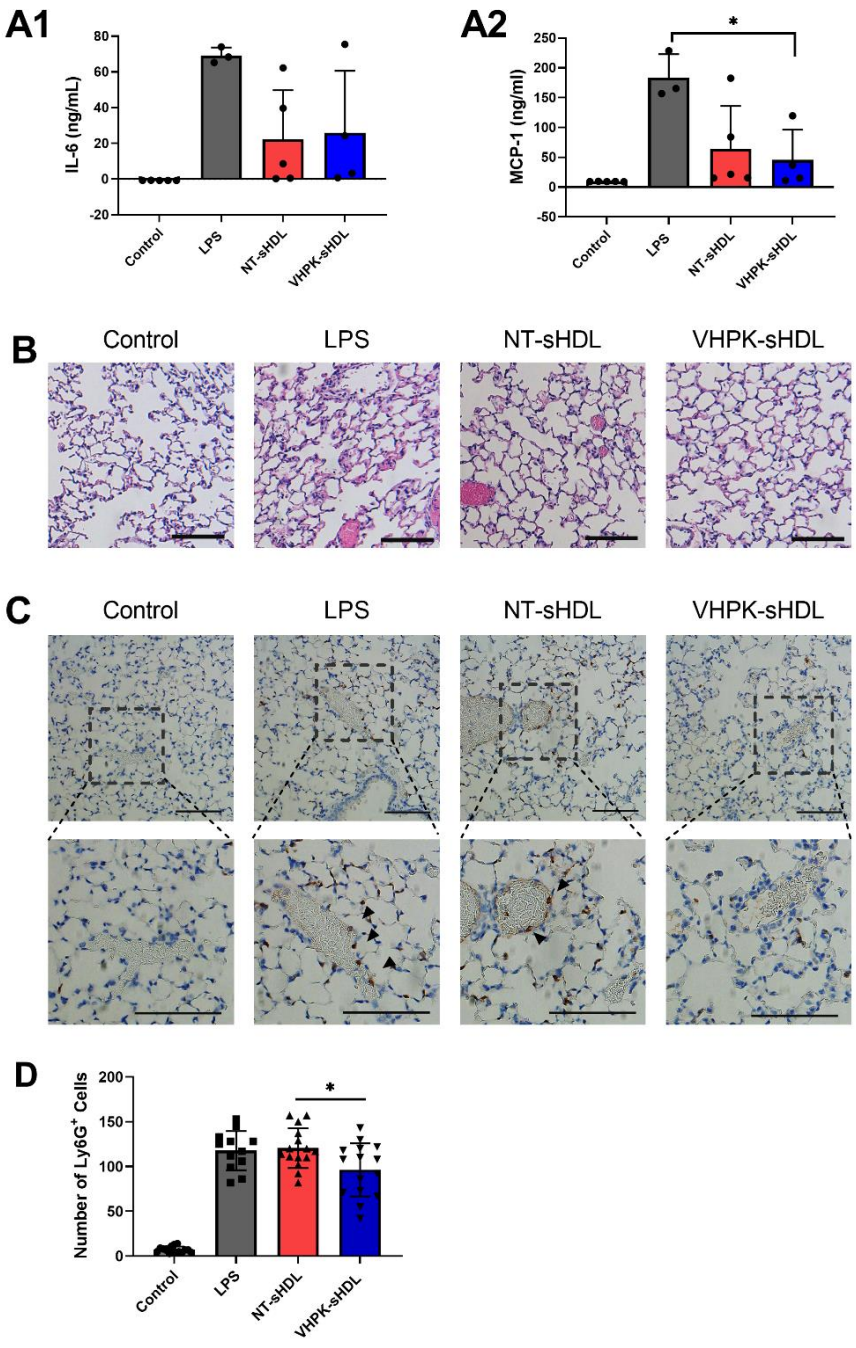

Figure 2.12 Plasma IL-6 (A1) and MCP-1 (A2) levels in mice 18 h after administration of LPS and sHDLs. (n = 3-5, mean ± SD, $p<0.05$). (B) Representative H&E staining of lung tissue sections of mice treated with different sHDLs. (C) Representative images of Ly6G IHC staining of lung sections mice treated with different sHDLs. Control indicates mice without LPS or sHDL treatment. Arrows indicate endothelial bound $Ly6G^+$ cells. The scale bar represents 100 µm. (D) Numbers of $Ly6G^+$ cells counted from IHC stained lung tissue sections (n = 12-15, mean ± SD. $Ly6G^+$ cells were counted from 3 random 20x fields from slides of each mouse).

2.5 Discussion

As the interface between systemic circulation and sites of inflammation, vascular endothelium is an essential targeting site for drug delivery in inflammatory diseases. Moreover, inflamed endothelium plays important roles in disease initiation and progression through recruiting leukocytes into inflamed tissue and producing inflammation mediators, making it a critical therapeutic target in inflammatory diseases. Thus, inflamed endothelial cells are both appealing delivery targets and potential therapeutic targets for the diagnosis and treatment of inflammatory diseases. Among various biomarkers on inflamed endothelium, VCAM-1 has been one of the most frequently studied targeting sites for activated endothelium. Numerous VCAM-1 targeted delivery systems have been developed to deliver imaging agents, small molecule drugs, and mRNAs to inflamed endothelial cells [143]. While most of the VCAM-1 targeting delivery systems were designed for the diagnosis and treatment of atherosclerosis [150], the applications have been broadened to other inflammatory diseases. For example, Garello et al. developed a VCAM-1 targeted paramagnetic micelles for neuroinflammation imaging [151]. In another study, a VLA-4 decorated cell membrane-coated nanoparticle was used to deliver dexamethasone to inflamed lungs [152].

With HDL-mimicking components and structure, sHDLs have been shown to have multiple HDL-like functions, including cholesterol efflux, anti-inflammatory, and endothelial protective functions [28, 153]. Typical HDL-mimicking particles are formulated with the full-length ApoA-1 protein, which is costly and challenging for large-scale manufacturing [56]. In this study, a more scalable and cost-efficient 22-mer ApoA-

1 mimetic peptide, namely 22A, was used to formulate sHDLs. Previous studies suggested that 22A-containing sHDLs have a strong neutralization capacity against endotoxins [72]. Through dislocating TLR-4 from cholesterol-rich lipid rafts, 22A containing sHDLs could also suppress TLR-4 signaling pathways and inhibit the production of proinflammatory cytokines from macrophages and endothelial cells [72, 154]. One of the 22A-containing sHDLs, ETC-642, has entered clinical trials and showed good safety profile and cholesterol mobilization capacity after a single dose intravenous administration [155, 156]. However, sHDLs offer little tissue specificity after systemic administration. For example, in a clinical study on atherosclerosis patients, sHDL showed only ~10% more biodistribution in inflamed plaque regions compared to normal arterial tissues [157]. Enabling an active targeting of sHDLs to inflamed endothelium may be an effective strategy to increase the delivery efficiency of sHDLs to target tissues.

In the present study, a VCAM-1 targeting VHPK peptide was conjugated to the surface of sHDLs to enable an active targeting to inflamed endothelial cells. *In vitro* cellular binding study showed that VHPK-sHDLs have increased cellular binding on activated HUVEC cells compared to resting cells in a VCAM-1 dependent manner. The cellular binding, instead of cellular uptake, was used to evaluate the delivery efficiency of sHDLs in the present study due to the unique interaction mechanisms of HDL and HDL mimetic particles with endothelial cells. While endothelial cells are capable of endocytosis and transcytosis of HDLs, the component exchange between endothelial cells and HDL can occur on the cell surface without particle internalization. For example, endothelial cells have been found to selectively uptake HDL-associated

components such as cholesterol, vitamin E, or hydrophobic dye through surface receptors without uptaking the entire HDL particle [158, 159]. Thus, cellular binding might be an important indicator of delivery efficiency of sHDLs. The increased delivery efficiency of VHPK-sHDLs to inflamed endothelium was also observed *in vivo* in the intravital microscopy study.

A series of *in vitro* studies were conducted to investigate whether VHPK-sHDLs preserve the anti-inflammatory effects of non-targeted sHDLs. Results showed that VHPK-sHDLs present comparable cholesterol efflux and anti-inflammatory effects to NT-sHDL, suggesting that VHPK peptide did not negatively affect the protective function of sHDLs. Interestingly, VHPK-sHDL reduced the monocyte adhesion on the activated HUVEC monolayers, which might be attributed to the competition between VLA-4 expressing monocytes and VHPK-sHDLs on VCAM-1 binding. Similar results were also observed in another VCAM-1 targeted nanoparticle [160], suggesting additional therapeutic mechanisms introduced by the conjugation of VCAM-1 targeted peptide.

Inflammation has diverse manifestations in different inflammatory diseases. For example, vascular inflammation in atherosclerosis is hallmarked by oxidized lipoproteins, monocyte infiltration, and cholesterol-laden foam cells in the subendothelial space [117]. In acute lung injury, uncontrolled inflammation is characterized by excessive production of proinflammatory cytokines as well as neutrophil infiltration [161]. While it is beyond the scope of this study to examine the efficacies of VHPK-sHDLs in every kind of inflammatory disease, as a proof-of-concept study, the therapeutic effects of VHPK-sHDLs were evaluated using an LPS-induced inflammation model. A sublethal dose of LPS was given to mice through i.p. injection. In addition to

evaluating systemic inflammation levels by serum cytokine levels, the lung was chosen as an organ of interest to evaluate the efficacy of sHDLs due to its vast endothelium surface area and well-characterized endothelial dysfunctions. Consistent with the previous study, both non-targeted and targeted sHDLs showed the potential to reduce inflammatory cytokine levels in plasma, which could be attributed to the LPS neutralization and anti-inflammation capacities of sHDLs [72]. When focusing on the lung tissues, H&E staining showed alleviated lung injury in NT- and VHPK-sHDL treated mice. Moreover, mice with VHPK-sHDL treatment showed less infiltration of $Ly6G^+$ leukocytes, which may suggest enhanced effects of VHPK-sHDLs on inhibiting leukocyte recruitment. It is worth noting several limitations of the *i.p.* LPS induced general inflammation model. First, the *i.p.* injection of a sublethal dose of LPS led to a large variance of inflammatory responses in mice. Second, the systemic administration of LPS complicated the efficacy analysis in lung tissues, as both systemic and local inflammatory response contributes to the results. Thus, while the present animal study provided proof-of-concept results on the therapeutic potential of VHPK-sHDL, a more defined animal model will be used to optimize VHPK-sHDL for specific inflammatory diseases.

2.6 Conclusion

VCAM-1 specific, inflamed endothelial targeted VHPK-sHDLs were prepared in the present study. The active targeting of VHPK-sHDLs to inflamed endothelial cells was demonstrated by *in vitro* and *in vivo* results. Conjugation of VCAM-1 targeting ligand did not compromise the cholesterol efflux and anti-inflammatory effects of sHDLs, and may

provide additional protective effects by inhibiting leukocyte adhesion to activated endothelium. Based on the results of this proof-of-concept study, VHPK-sHDLs hold the potential to be further optimized to fully exert therapeutic potential to inflammatory disease either as a stand-alone therapy or drug delivery carrier.

Chapter 3 Enhancement of Anti-Inflammatory Effects of Synthetic High-Density Lipoproteins by Incorporation of Anionic Lipids

3.1 Abstract

Phosphatidylserine (PS) is an anionic phospholipid component in endogenous high-density lipoprotein (HDL). With the intrinsic anti-inflammatory effects of PS and the correlation between PS content and HDL functions, it was hypothesized that incorporating PS would enhance the therapeutic effects of HDL mimetic particles. To test this hypothesis, a series of synthetic high-density lipoproteins (sHDLs) were prepared with ApoA-1 mimetic peptide, POPC, and POPS. Incorporating PS was found to improve the particle stability of sHDLs. Moreover, increasing PS content in sHDLs enhanced the anti-inflammatory effects on LPS-activated macrophages and endothelial cells. The incorporation of PS had no negative impact on cholesterol efflux capacity, *in vivo* cholesterol mobilization, and did not affect the pharmacokinetic profiles of sHDLs. Such results suggest the therapeutic potential of PS-containing sHDLs on inflammation resolution in atherosclerosis and other inflammatory diseases.

3.2 Introduction

High-density lipoproteins (HDLs) are a group of endogenous nanoparticles consisting of apolipoproteins and diverse lipid components[1]. As a major mediator in reverse cholesterol transport, HDL induces cholesterol efflux from peripheral cells and

transfers cholesterol to the liver for elimination[4]. Moreover, HDLs play a pivotal role in inflammation resolution by reducing pro-inflammatory cytokine release from immune effector cells [162], inhibiting endothelial activation [163], and scavenging oxidative lipid species [164]. Low HDL or HDL-cholesterol (HDL-c) levels, altered HDL composition, and impaired HDL functions have been associated with varieties of diseases including cardiovascular diseases, autoimmune diseases, and infections [54, 74, 165].

Biomimetic, synthetic HDLs (sHDLs) have attracted much interest in the past two decades. Mimicking components of endogenous HDLs, sHDLs are typically composed of ApoA-1 or its mimetics, as well as lipid components such as phospholipids and sphingolipids [139]. Several sHDL candidates, such as CSL-111, CSL-112, CER-001 and ETC-642, have been developed and have entered clinical trials [36, 166, 167]. Initially developed for atherosclerosis and optimized to promote cholesterol efflux, these sHDL candidates showed potent HDL-c elevating effects in Phase I/II clinical trials [31, 168]. However, phase II/III results only showed sub-optimal therapeutic benefits [169]. Such clinical results called for a re-evaluation of the current HDL-c-focusing treatment strategies of sHDLs. Moreover, there has been an increasing recognition that HDL functionality, instead of HDL-c levels, is a better indicator of the protective effects of HDLs. Thus, there has been a paradigm shift for HDL replacement therapy from elevating HDL-c levels to enhancing sHDL functions [54]. Developing sHDLs with more sophisticated functionalities is essential for the successful clinical translation of sHDLs.

In contrast to the simple composition of sHDLs, endogenous HDLs present very complex and highly dynamic proteomic and lipidomic profiles, which are closely associated with the functions of HDLs [1, 61]. Among various bioactive components of

endogenous HDLs, anionic phospholipids, such as phosphatidylinositol (PI), phosphatidic acid (PA), and phosphatidylserine (PS), have been shown to have a significant association with the protective functions of HDLs [64]. Notably, a strong positive correlation was found between PS abundance and HDL functions such as cholesterol efflux, anti-inflammation, and anti-oxidation capacities [64, 170].

PS is an anionic lipid mainly located in the inner leaflet of cell membranes. On apoptotic cells, PS is translocated to the outer leaflet of membranes, serving as an ‘eat me’ signal to phagocytes such as macrophages [171]. Activation of PS receptors induces anti-inflammatory and immunosuppressive responses in phagocytes, which enables the silent clearance of apoptotic cells [65, 171]. Based on the correlation between PS content and HDL functions, as well as the intrinsic anti-inflammatory effects of PS, it was hypothesized that introducing PS could increase the therapeutic effects of sHDLs [66, 170]. This hypothesis has been recently examined by Darabi et al., PS-containing sHDLs showed greater anti-inflammatory effects by modulating Akt1/2/3- and p38 MAPK- mediated signaling pathways [172]. As a continuous effort to investigate the impacts of PS on the functionality of HDL mimetics, in the present study, a series of PS-containing sHDLs was prepared using POPC, POPS, and an ApoA-1 mimetic peptide 22A. The impacts of PS incorporation on particle characteristics, anti-inflammatory effects, *in vitro* and *in vivo* cholesterol efflux capacities, and pharmacokinetic profiles were investigated.

3.3 Materials and Methods

3.3.1 Materials

22A peptide (PVLDLFRELLNELLEALKQKLK) was synthesized by Genscript Inc. (Piscataway, NJ). 1-Palmitoyl-2-oleoyl-sn-glycero-3-phosphocholine (POPC) and 1-palmitoyl-2-oleoyl-sn-3-phospho-L-serine sodium salt were (POPS-Na) were purchased from NOF America Corporation (White Plains, NY). LPS from Escherichia coli O111 (L2630):B4 was purchased from Sigma. Mouse IL-6, TNF-α, MCP-1 ELISA kits were purchased from Invitrogen.

3.3.2 Cell culture

RAW264.7 and J774.A1 cells were obtained from ATCC. Both cells were cultured in DMEM media supplemented with 10% fetal bovine serum (FBS) and 1% Penicillin-Streptomycin (10,000 U/mL). HUVEC cells were obtained from Lonza (Morristown, NJ) and cultured in endothelial cell growth media EGM-2 purchased from Lonza. Cells were used before passage 7. All cells were cultured in a 37 °C incubator with 5% CO_2.

3.3.3 Preparation and characterization of sHDLs

sHDLs composed of 22A, POPC and POPS were prepared by the lyophilization-rehydration method. 22A and POPC were dissolved and mixed in acetic acid in lipid to peptide weight ratio of 2:1. For POPS-containing sHDLs, 5%, 10%, 25% or 50% of POPC (mass ratio) was replaced by POPS-Na during preparation. The mixture was then freeze-dried. The lyophilized powder was rehydrated by PBS (pH 7.4), followed by 3 thermocycles. For POPC-sHDLs and 5% POPS/POPC-sHDLs, the thermocycle conditions are room temperature (5 min) and ice bath (5 min) trice. For 10%, 25% and 50% POPS/POPC-sHDLs, the thermocycle conditions are 37 °C (5 min) and ice bath (5

min) trice. The particle size and zeta potential of different sHDLs were examined by dynamic light scattering (DLS) using Malvern Zetasizer Nano ZSP (Westborough, MA). The purity of sHDLs was analyzed by gel permeation chromatography (GPC) on a Tosoh TSK gel G3000SWxl column with a PBS flow rate of 1 mL/min and UV detection at 220 nm. For transmission electron microscopy (TEM) observation, different sHDLs were loaded on a carbon film-coated 400 mesh copper grid from Electron Microscopy Sciences (Hatfield, PA), negatively stained with 1% (w/v) uranyl formate and dried. The samples were imaged with 100kV Morgagni TEM. For particle stability evaluation, different sHDLs were incubated in PBS (pH 7.4) at a 22A concentration of 1 mg/mL at 37 °C. At different time points, the particle size of sHDLs was analyzed by DLS.

3.3.4 Cytotoxicity assay

RAW 264.7cells were seeded to 96-well plates at a density of 5 x 10^4 cells/well. After overnight incubation, cells were incubated with different sHDLs with different 22A concentrations for 24 h. At the end of the incubation, the cell viability was determined using CellTiter 96® AQueous One Solution Cell Proliferation Assay following the protocol provided by the manufacturer.

3.3.5 Cholesterol efflux assay

J774.A1 cells were seeded in 24-well plates at a density of 2 x 10^5 cells/well. Cells were incubated overnight with 1 µCi/ml [^{3}H] cholesterol in DMEM containing 0.3% fatty acid-free bovine serum albumin (BSA) and 5 µg/mL ACAT inhibitor Sandoz 58-035. At the end of the incubation, the media was discarded and cells were then washed with PBS twice. Cells were then equilibrated in DMEM containing 0.3% BSA and 5 µg/mL

ACAT inhibitor Sandoz 58-035 for 24 h. The media was discarded, and cells were washed with PBS again. The [^{3}H] cholesterol labeled cells were incubated with different sHDLs for 4 h at 22A concentrations of 5, 10, 25 or 50 µg/mL in 0.5 mL DMEM containing 0.3% BSA. At the end of incubation, media were collected, and cells were lysed with 0.5 mL 0.1% SDS and 0.1 N NaOH. The cell culture media and cell lysate were centrifuged at 400 g for 10 min. 200 µL supernatant was collected. The radioactive counts were measured using liquid scintillation counting by Perkin Elmer Tri-Carb 2910TR (Waltham, MA). The cholesterol efflux percentage was calculated by dividing the media count by the sum of the media and cell counts.

3.3.6 Anti-inflammatory study

For LPS-induced inflammation, RAW 264.7 cells were seeded to 24-well plates at a density of 2 x 10^5/well and incubated overnight to allow attachment. Cells were co-incubated with 100 ng/ml LPS and sHDLs at a 22A concentration of 10, 20, or 50 µg/ml for 12 h. The cell culture media were collected. The cytokine concentrations were quantified by ELISA. For TNF-α-induced inflammation, HUVEC cells were seeded to 12-well plates and cultured to reach confluence before experiments. HUVEC cells were then incubated with sHDLs and 2 ng/ml TNF-α for 12 h. The cytokine concentrations in cell culture media were quantified by ELISA.

3.3.7 Efferocytosis assay

Efferocytosis assay was conducted using Efferocytosis kit (Cayman Chemicals, Ann Arbor MI) according to instructions from the manufacturer with modification. Briefly, for effector cell labeling, RAW264.7 cells were labeled with CytoTell Blue in PBS at 37

°C for 30 min. The cells were then washed twice with complete media, seeded into 12-well plates at a density of $3x10^5$/well, and incubated overnight. Fluorescent labeled apoptotic bait cells were prepared by incubating non-labeled RAW 264.7 cells with CFSE at 37 °C for 30 min. Apoptosis of the CFSE labeled cells was induced by incubation with staurosporine for 6 h. For the co-incubation study, effector cells, bait cells ($3x10^5$/well), and different sHDLs (22A concentration 100 μg/mL) were incubated for 18 h. For the pre-treatment study, effector cells were pre-treated with different sHDLs (22A concentration 100 μg/mL), followed by the addition of bait cells. After incubation, the effector cells were collected by gentle scraping. The cell suspension was analyzed by flow cytometry. The percentage of CFSE/CytoTell Blue double-positive cells in effector cells was calculated.

3.3.8 In vivo cholesterol mobilization study

Sprague-Dawley rats (8-9 weeks old) were purchased from Charles River Breeding Laboratories (Portage, MI). Animals were randomly assigned to 3 groups with 4 rats per group, and fasted 8 h prior to the administration of sHDLs. POPC-sHDL, 25% POPS/POPC-sHDL and 50% POPS/POPC-sHDL were injected to rats through tail vein at a 22A dose of 50 mg/kg. At different time points, approximately 300 μL blood samples were drawn from the jugular vein. Serum was isolated by centrifuging blood samples at 8,000 rpm for 10 minutes at 4°C. The serum samples were stored at -80 °C until analysis. The serum concentration of phospholipids (PL), total cholesterol (TC), and free cholesterol (FC) were quantified enzymatically using Wako detection kits (Wako Chemicals, Richmond, VA) following protocols provided by the manufacturer.

3.3.9 Statistical analysis

Data analysis was conducted using GraphPad Prism 8. Statistical significance was determined using a two-tailed unpaired Student's t-test for 2 groups of data or one-way analysis of variance (ANOVA) for data of more than 2 groups except for those stated otherwise. A p-value less than 0.05 was considered statistically significant.

3.4 Results

3.4.1 Preparation and characterization of sHDLs

As shown in **Figure 3.1A,** the average particle sizes of different sHDLs were around 12-15 nm, with no difference observed between POPC-sHDL and POPS-containing sHDLs. As expected, the zeta potential of the sHDLs decreases with increasing POPS percentage (**Figure 3.1B**). Interestingly, GPC results showed a more uniform particle size distribution for sHDLs with higher POPS content (**Figure 3.1C**). The DLS and GPC results are consistent with the SEM images of different sHDLs (**Figure 3.1D**). The stability study showed a fast increase in particle size of POPC-sHDLs when incubated at 37 °C, indicating aggregation of POPC-sHDLs. Meanwhile, sHDLs containing higher POPS percentages showed improved particle size stability manifested with slower aggregation and smaller size of aggregates (**Figure 3.1E**).

3.4.2 Cellular toxicity

The potential cellular toxicity of POPS-containing sHDLs was compared with POPC-sHDLs. A series of 22A concentrations up to 500 μg/ml was tested on RAW264.7 macrophages. As shown in **Figure 3.2**, no significant cellular toxicity was

found in all concentration levels for all formulations. No statistical difference was found between different groups.

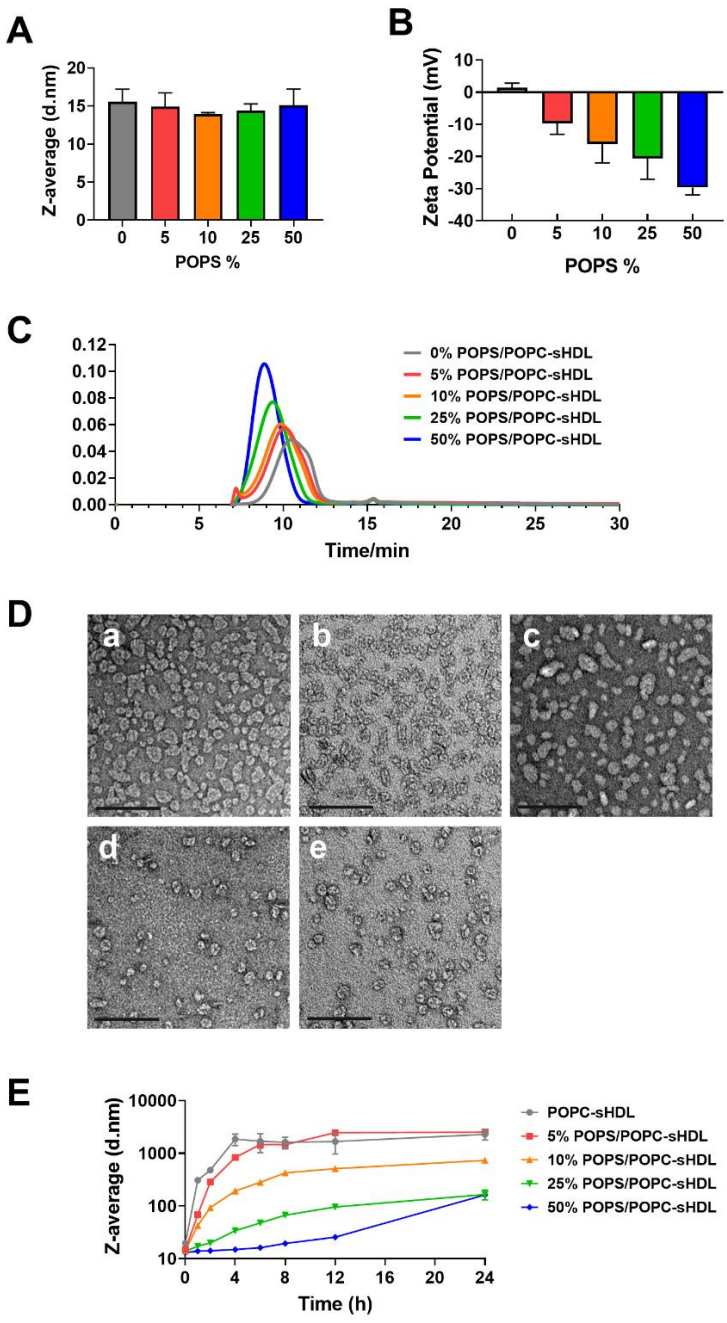

Figure 3.1 Particle size (A) and zeta potential (B) of different sHDLs measured by DLS (n = 3, mean ± SD). (C) GPC chromatogram of different sHDLs. (D) SEM images of different sHDLs. (E) Particle sizes of sHDLs at different time points when incubated at 37°C (n = 3, mean ± SD).

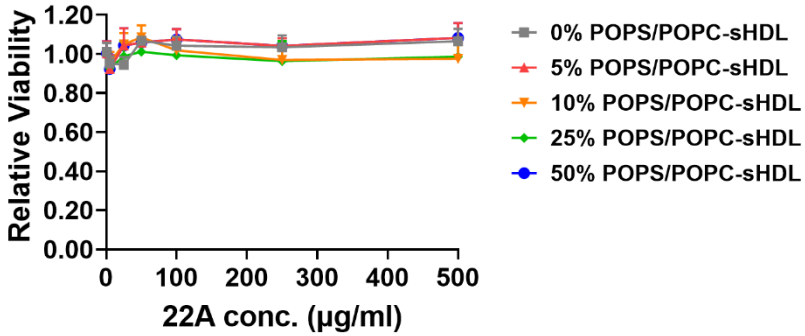

Figure 3.2 Relative cell viability of RAW264.7 cells incubated with different sHDLs. Cells without treatment were used as 100% (n = 6, mean ± SD).

3.4.3 Cholesterol efflux assay

The cholesterol efflux capacity of different sHDLs was evaluated in J774 A.1 macrophage loaded with ^{3}[H]-cholesterol. As shown in **Figure 3.3**, all sHDLs could induce significant cholesterol efflux in a dose-dependent manner. However, no statistical difference was observed among sHDLs with different POPS percentages, suggesting the lipid composition did not significantly affect the cholesterol efflux capacity of sHDLs.

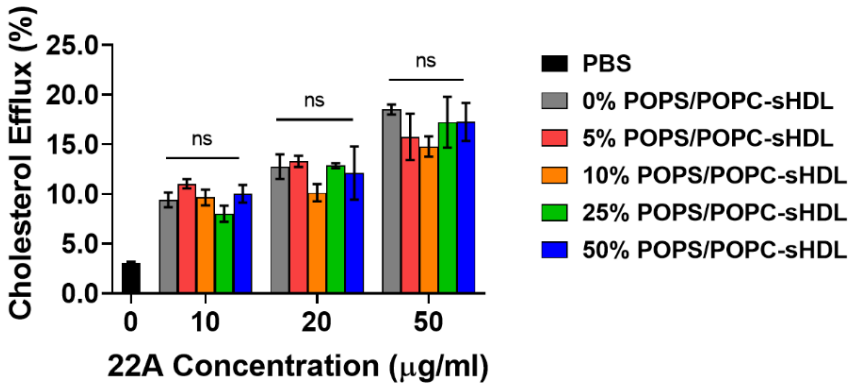

Figure 3.3 Cholesterol efflux effects of different sHDLs (n = 3, mean ± SD).

3.4.4 Anti-inflammatory effects

The anti-inflammatory effects of different sHDLs were investigated on LPS-treated RAW 264.7 macrophages and HUVEC cells. As shown in **Figure 3.4**, while LPS greatly increased the production of pro-inflammatory cytokines, sHDL treatment reduced the cytokine secretion on both cell lines. Notably, a greater reduction in proinflammatory cytokines was observed on cells treated with sHDLs composed of a higher POPS percentage, suggesting stronger anti-inflammatory effects of POPS-containing sHDLs.

3.4.5 Efferocytosis assay

Efferocytosis study was conducted on RAW 264.7 macrophages. As shown in **Figure 3.5A**, when effector cells are co-incubated with sHDLs and bait cells, efferocytosis efficiency decreased as POPS content in sHDLs increased. When macrophages were pretreated with sHDLs prior to efferocytosis assay (**Figure 3.5B**), POPC-sHDL, 5%- or 10%- POPS/POPC-sHDLs did not alter the efferocytosis efficiency of macrophages compared to control cells. However, pre-incubating cells with 25%- and 50%-POPS/POPC-sHDL led to a slight increase in the percentage of double-positive in effector cells, suggesting an enhanced efferocytosis activity of macrophages.

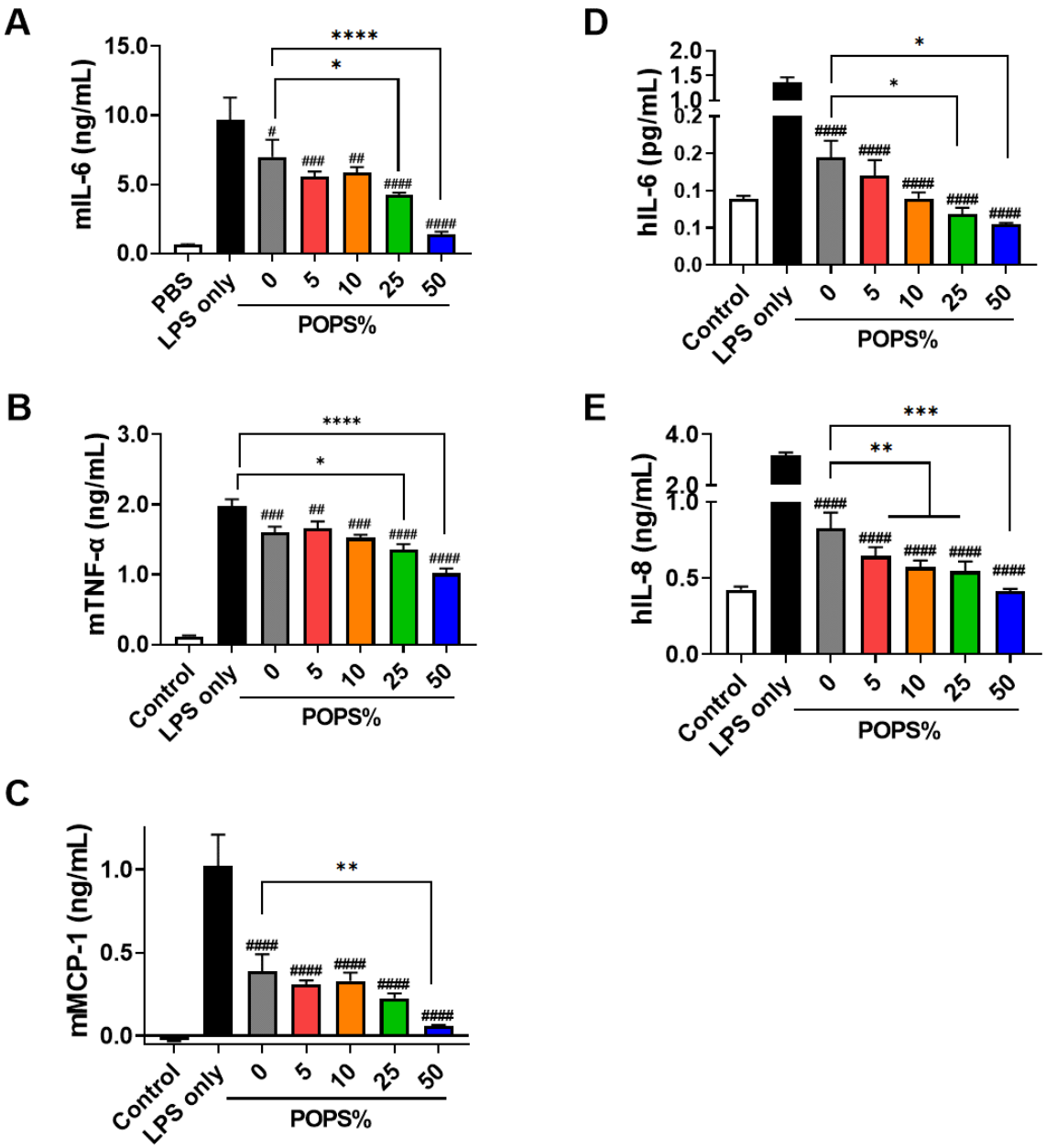

Figure 3.4 Pro-inflammatory cytokine levels from LPS-treated RAW264.7 (A, B, and C) or HUVEC (D and E) cells. (n = 3, mean ± SD). *p<0.05; **p<0.01; ***p<0.005, ****p<0.0001 compared to POPC-sHDLs (0% POPS group). #p<0.05; ##p<0.01; ###p<0.005, ####p<0.001 compared to LPS-only group.

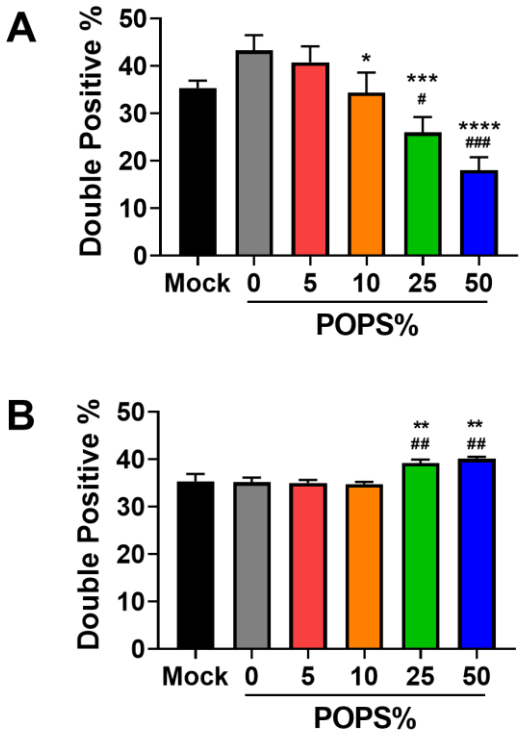

Figure 3.5 Percentage of CytoTell Blue/CFSE double-positive effector cells after (A) co-incubated or (B) pretreated with different sHDLs (n = 3, mean ± SD). *p<0.05; **p<0.01; ***p<0.005, ****p<0.0001 compared to POPC-sHDLs (0% POPS) group. $^{\#}$p<0.05; $^{\#\#}$p<0.01; $^{\#\#\#}$p<0.005 compared to mock group.

3.4.6 In vivo PK/PD studies

As shown in **Figure 3.6**, *i.v.* infusion of sHDLs induced a significant increase in serum cholesterol levels in rats. Compared to the POPC-sHDLs-treated group, rats treated with 25%- and 50%-POPS/POPC-sHDLs showed slightly higher total cholesterol and free cholesterol levels in 2 h post-injection. No significant difference was found in phospholipid levels between different groups at all timepoints.

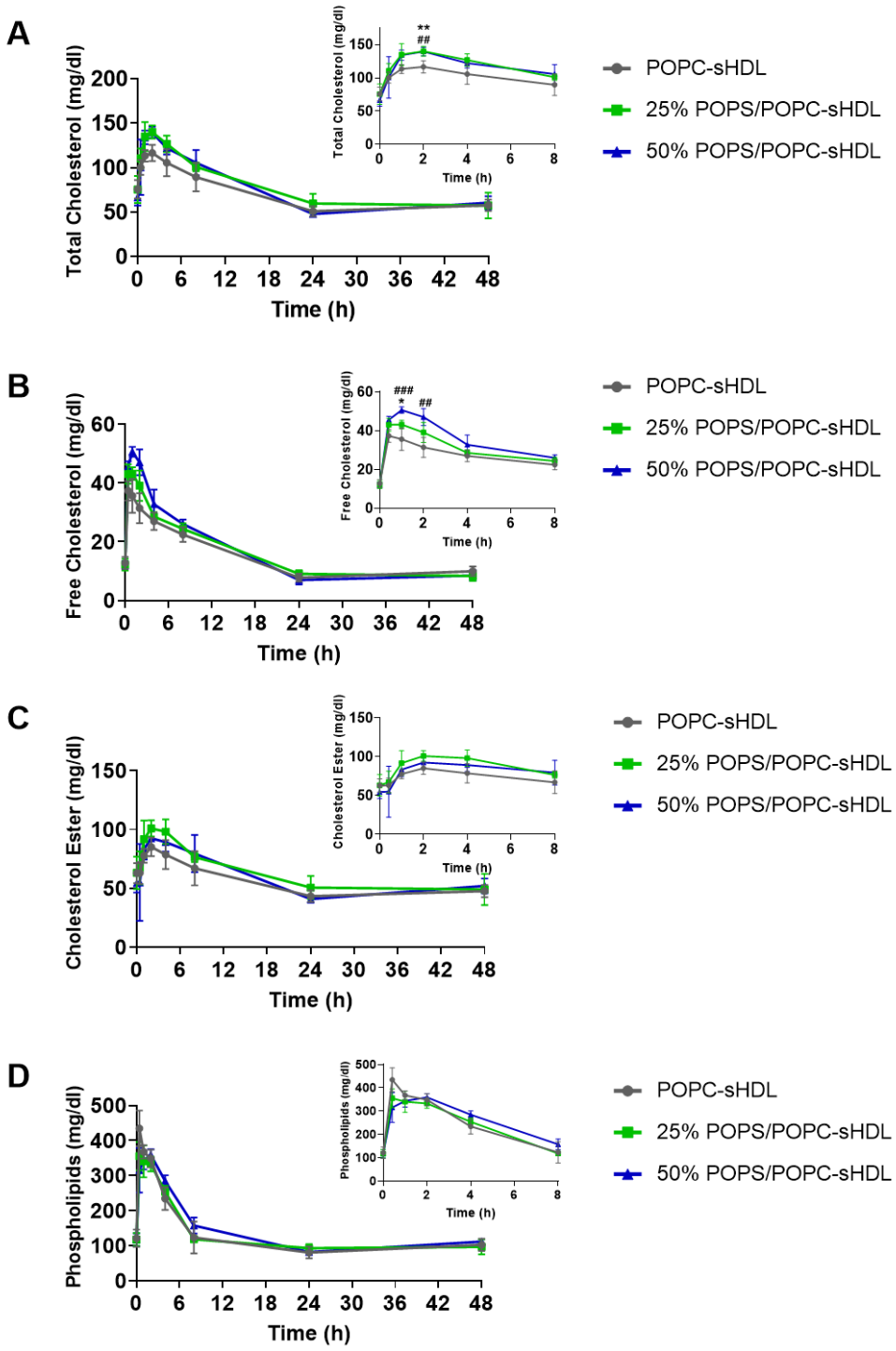

Figure 3.6 Total cholesterol (A), free cholesterol (B), cholesterol ester (C) and phospholipids (D) levels in rat serum after i.v. injection of different sHDLs (n = 4, mean ± SD). *p<0.05, **p<0.01 for 25% POPS/POPC-sHDL compared to POPC-sHDL. ##p<0.005, ###p<0.001 for 50% POPS/POPC-sHDL compared to POPC-sHDL.

3.5 Discussion

Despite accounting for less than 1% of phospholipid content, anionic phospholipids such as PG, PS, and PI are associated with protective functions of HDLs, such as cholesterol efflux, anti-inflammation, and anti-oxidation effects [173]. Among various anionic lipids, PS has generated great research interest with its intrinsic anti-inflammatory capacities [66]. However, the impact of PS on the functionality of sHDL has not been fully examined. In this study, a series of sHDLs with different POPS contents was prepared. The effects of PS on particle characteristics, cholesterol efflux, anti-inflammatory effects, efferocytosis, as well as pharmacokinetic profiles were evaluated.

Substituting POPC to POPS in sHDLs led to a reduction of zeta potential of sHDLs without impacting the main particle size. However, POPS-containing sHDLs presented a more uniform particle size distribution and greater size stability when incubated at 37 °C. The improved particle stability could be attributed to two reasons. First, POPS has a higher phase transition temperature of 14 °C compared to -9 °C of POPC. Thus, with the increasing POPS content, the fluidity of the lipid membrane of sHDLs decreases, which prevents the aggregation of particles [145]. Second, negatively charged POPS creates electrostatic repulsion between particles, which is expected to increase the colloidal stability of sHDLs.

Regarding anti-inflammatory effects, a recent study by Darabi et al. showed that PS incorporation into recombinant HDL particles led to more potent anti-inflammatory effects by modulating Akt1/2/3- and p38 MAPK signaling pathways [172]. Consistent with the previous results, in the present study, POPS/POPC-sHDLs showed increased

anti-inflammatory effects on LPS-activated macrophages and endothelial cells in a POPS-content-dependent manner [172]. The results suggest that POPS incorporation would be an effective strategy to enhance the anti-inflammatory effects of sHDLs.

Efferocytosis, a process where apoptotic cells are cleared by macrophages and other phagocytes in a non-inflammatory manner, is essential for the maintenance of homeostasis and inflammation resolution [174]. Impaired efferocytosis causes the secondary necrosis of apoptotic cells, which contributes to unresolved inflammation in various chronic inflammatory diseases [174-176]. Serving as an ‘eat me’ signal, PS is essential for the recognition and phagocytosis of apoptotic cells in efferocytosis [177]. Activating PS receptors by administrating PS-containing liposomes has been shown to restore the efferocytosis capacity of macrophages in several *in vivo* studies [178]. In the present study, when macrophages were co-incubated with sHDLs and apoptotic cells, increasing POPS percentages led to decreased efferocytosis of bait cells, which may be attributed to the competition of PS receptors [172]. However, when macrophages were pre-treated with sHDLs, slightly higher efferocytosis efficiency was shown on macrophages treated with 25%- or 50%-POPS/POPC-sHDLs. The net effects of POPS-containing sHDLs on efferocytosis *in vivo* may depend on various factors such as dose and pharmacokinetic profiles.

Recognition of apoptosis cells by PS receptors has been shown to lead to a rapid increase in ABCA-1 expression and enhanced cholesterol efflux [179, 180]. Thus, the hypothesis that increasing PS exposure may enhance cholesterol efflux was tested [170]. However, *in vitro* studies showed little difference in cholesterol efflux capacity between POPC-sHDLs and POPS/POPC-sHDLs. This result is consistent with previous

studies by Darabi et al., where PS containing recombinant HDLs did not increase ABCA-1 expression or *in vitro* cholesterol efflux [172]. Interestingly, in the *in vivo* pharmacodynamic study, POPS-containing sHDLs showed a lightly higher cholesterol mobilization capacity while presenting similar pharmacokinetic profiles to POPC-sHDLs. The difference between *in vivo* and *in vitro* results would warrant further investigation.

It was reported that incorporating PS into liposomes could accelerate the elimination of liposomes due to the increased uptake of liposomes in the liver [181]. As the liver is the major elimination organ for sHDLs, there was a concern that introducing PS may negatively affect the pharmacokinetic profiles of sHDLs. However, there was little difference in serum phospholipid levels between the POPC-sHDL group and the two POPS/POPC-sHDL groups, suggesting a limited impact of PS to sHDL pharmacokinetic profiles. The different effects of PS may be explained by different elimination mechanisms of liposomes and sHDLs. Typically, liposomes are mainly eliminated by the reticuloendothelial system such as Kupffer cells in an opsonization-dependent manner [182]. However, with HDL-mimicking structures and small particle sizes, sHDLs are generally considered to be able to evade the reticuloendothelial system [28, 183]. Such difference was exemplified in an early pharmacokinetic study of PS-containing liposomes in rats. Following an initial rapid elimination attributed to elimination by the reticuloendothelial system, PS component in liposomes was found to be incorporated into HDL and eliminated at a slower rate with a similar half-life as rat HDL [184]. Such observation may reconcile the discrepancy in the effects of PS on pharmacokinetic properties between liposomes and sHDLs.

3.6 Conclusion

In this study, a series of sHDLs were prepared with ApoA-1 mimetic peptide, POPC, and POPS. Increasing PS content in sHDL particles improved particle stability and significantly increased the anti-inflammatory effects of sHDLs. Limited impacts were found on cholesterol efflux capacity and pharmacokinetic profiles of sHDLs. Such results suggest the therapeutic potential of PS-containing sHDLs on inflammation resolution in atherosclerosis and other inflammatory diseases.

Chapter 4 Predicting Drug Release Kinetics from Nanocarriers inside Dialysis Bags

4.1 Abstract

Dialysis methods are frequently used to determine the *in vitro* drug release kinetics of nanoparticle drug delivery systems. However, the need for the released drug to diffuse through the dialysis membrane delays its appearance in the sampling compartment. Thus, the apparent drug release data outside the dialysis bag typically does not match the desired release kinetics inside the bag adjacent to the nanocarriers. To address this issue, here we describe a simple approach to determine the actual drug release kinetics from nano drug carriers inside the dialysis bag from the experimental data measured from the sampling compartment. First, a calibration experiment is carried out to determine the diffusion barrier properties of the dialysis membranes. The apparent drug release profile of the nanocarrier is then determined using the dialysis method, and a mathematical model is applied to determine the actual drug release kinetics from the experimental data. The model was tested on DOXIL® (doxorubicin liposomes), and an excellent agreement was found between the predicted and measured drug concentration inside the dialysis membranes. By taking the barrier effects of dialysis membranes into consideration, our model independent of drug carrier not only enables the proper interpretation of the data from dialysis studies but also helps to evaluate the dialysis methodology applied to *in vitro* drug release assays.

4.2 Introduction

Dialysis methods are frequently used to determine the *in vitro* drug release profiles of nanoparticle drug delivery systems. The drug release profile generated from dialysis-based assays has been widely used to guide formulation development, facilitate quality control and regulatory filing, and, in the best-case scenario, establish the *in vitro-in vivo* correlation (IVIVC) of the nanoparticle formulation [102, 103, 185].

However, the validity of the dialysis method as well as the reliability of the release data generated from dialysis assays have long been questioned [186-188]. For conventional dialysis settings (**Figure 4.1**), the drug that is released from the nanocarriers first enters the solution inside the dialysis bag (donor compartment) and then permeates through the dialysis membrane to reach the bulk solution outside the dialysis bag (receiver compartment). Thus, the apparent drug release kinetics, which is measured by sampling the receiver compartment, is determined by both the actual drug release kinetics and drug permeation kinetics. In practice, it is usually assumed that the membrane permeation process is rapid (i.e., not rate limiting) and can be neglected. As a result, the apparent drug release kinetics is often interpreted as the actual drug release kinetics without further processing. However, accumulating evidence suggests that dialysis membranes can significantly delay the translocation of the released drug, in which case the apparent drug release profile will not properly describe the actual drug release kinetics [104, 187, 189-191]. For example, Zambito *et al.* [186] compared the drug release data of diclofenac-loaded nanoparticles using dialysis and an ultracentrifugation method. It was found that in the dialysis method, the membrane permeation process, instead of the actual drug release kinetics, dominated the rate by

which the drug appeared in the receiver compartment where samples are taken [186]. Under this circumstance, even though the drug is rapidly released from the nanocarrier, the apparent drug release rate remains low, which may be wrongly attributed to the sustained-release of the carriers if not carefully interpreted.

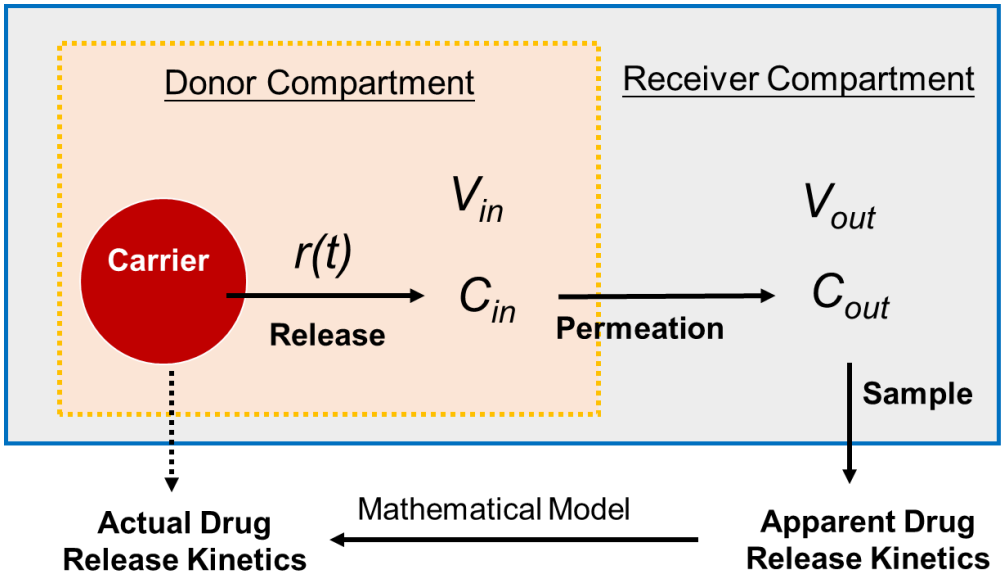

Figure 4.1 The relationship between apparent and actual release kinetics occurring during release testing by the dialysis method. The drug molecules are released from the carrier with the actual rate of *r(t)* in the solution inside the dialysis membrane (the donor compartment). Then the released drug diffuses through the dialysis membrane to reach the bulk solution outside the dialysis membranes (the receiver compartment). The samples are taken from the receiver compartment to calculate the apparent drug release fraction from the carrier. V_{in} is the volume inside the dialysis donor compartment, C_{in} is the concentration of the released drug in the donor compartment, V_{out} is the volume of the receiver compartment, and C_{out} is the concentration of the released drug in the receiver compartment.

Some studies that discuss the pitfalls of dialysis methods conducted a parallel release assay using different methods such as ultracentrifugation, ultrafiltration, and the drug-selective electrode to determine the actual drug release kinetics for comparison

[186, 192]. However, the external forces used in alternative methods such as centrifugation force may also alter the drug release profile, leading to an improper comparison. Also, such strategies typically only allow for the qualitative, but not quantitative, methodological analysis of dialysis methods. Thus, simple mathematical methods which differentiate the actual drug release kinetics and the effects of dialysis membranes from the apparent drug release data could be very useful for the proper data interpretation and methodology evaluation.

Several mathematical methodologies have been described to determine the exact drug release kinetics by taking the effects of dialysis membranes into consideration [188, 192-194]. For example, Anderson et al. developed a series of mechanism-based mathematic models to determine the drug release constant of liposomes using the apparent release profiles derived from the dialysis assays [192, 193]. However, most models have focused on certain drug delivery systems and required drug-specific parameters such as solubility, pKa, particle sizes and distribution coefficients, which complicates their general application in determining actual drug release kinetics for drug delivery systems. In the present study, we do not seek to explain the release of a specific nanocarrier nor the effect of the release set-up on drug release kinetics. Instead, we propose a general approach, which determines the actual drug release kinetics inside the dialysis bag and enables quantitative methodological analysis. In the approach, calibration experiments are performed first to determine the barrier property of dialysis membranes. The apparent drug release kinetic data is then collected by the conventional dialysis assay while determining any volume changes in the bag. The apparent release data outside the bag is suitably fit to allow an estimation

of its time derivative before a mathematical model is applied to calculate the actual drug release kinetics. The free drug concentration inside the dialysis bag can also be predicted and analyzed for methodology evaluation purposes. The proposed model, which is independent of the drug carrier, not only enables the proper interpretation of the data of dialysis assays, but also could become a valuable tool to evaluate the appropriateness of the dialysis methodology used for *in vitro* drug release testing of nanoparticle drug delivery carriers.

4.3 Materials and Methods

4.3.1 Materials

DOXIL® (doxorubicin HCl liposome injection) was purchased from the University of Michigan Hospital Pharmacy. The mean particle size of DOXIL liposomes is reported to be 87 nm by our previous manuscript [195]. Doxorubicin hydrochloride (DOX•HCl) was purchased from SHJNJ Pharmatech (Shanghai, China). 2-Hydroxypropyl-beta-cyclodextrin (HP-CD) was purchased from SHJNJ Pharmatech (Shanghai, China). Sucrose was purchased from Fisher Chemical. Dialysis bags from regenerated cellulose (RC) membranes with molecular weight cut-off (MWCO) of 10 kD and 20 kD and Float-A-lyzer® cellulose ester (CE) dialysis tubes with MWCO of 8-10 kD, 20 kD, 50 kD, 100 kD and 300 kD were purchased from Spectrum Laboratories (Rancho Dominguez, CA). ZebaTM spin desalting columns (0.5 mL, 7 kD MWCO) were purchased from Thermo Fisher Scientific. All other reagents were of analytical grade and purchased from Sigma.

4.3.2 In vitro drug release kinetic experiments

The USP-4 (flow-through cell apparatus) drug dissolution method, where the nanoparticle formulation is trapped in dialysis bags and dialyzed against the circulating release media flowing through the cells, is selected to represent the typical experiment set-up of dialysis-based nanoparticle drug release assays. A rapid, discriminatory, and robust USP-4 drug release assay for DOXIL was developed previously in our lab and used to perform the calibration and drug release kinetics experiments [195]. Briefly, 0.4 mL DOX•HCl stock solution (2 mg/mL, in 10 mM Histidine•HCl, 10% sucrose (w/v), pH 6.5) or 0.4 mL DOXIL® formulation (2 mg/mL in DOX•HCl) was added to the dialysis bags for calibration experiments or drug release experiments respectively, together with 1.2 mL release media composed of 100 mM NH_4HCO_3, 5% sucrose (w/v), 75 mM MES, 5% HP-CD (w/v), and 0.02% NaN_3 (pH 6.0). The dialysis tubes were inserted into the flow-through cells of the USP-4 apparatus. 78.4 mL release media was added into the media reservoir to achieve the total volume of 80 mL. The experiment temperature was set to 45 °C to achieve the accelerated release of DOXIL. The flow rate was 16 mL/min [15]. The absorbance of the released doxorubicin was detected using Specord 200 plus Spectrophotometer at 480 nm. A linear relationship between free doxorubicin concentration and UV absorbance ($R^2 > 0.999$) was confirmed by the standard curve. To determine the UV absorbance of doxorubicin once completely released from the carriers, a free DOX control was set by directly placing 0.4 mL DOX•HCl stock solution and 79.6 mL release media in the media reservoir. The apparent cumulative drug release fraction (f_{app}) is calculated with the following formula:

$$f_{app} = \frac{A_{(Released\ DOX)} - A_{(Background)}}{A_{(Free\ DOX\ control)} - A_{(Background)}} \bullet 100\%$$

Where $A_{(Released\ DOX)}$ is the UV absorbance of the released DOX in bulk solution outside the dialysis membrane, $A_{(Free\ DOX\ control)}$ is the UV absorbance of the control DOX solution, and $A_{(background)}$ is the UV absorbance of blank release media.

4.3.3 Quantification of doxorubicin

Zeba™ spin desalting columns (7 kD MWCO) were used to separate liposomal doxorubicin and released free doxorubicin. To confirm the capacity of desalting columns to remove free DOX, 100 μL DOX stock solution (2 mg/mL) was passed through Zeba™ spin desalting columns (7 kD MWCO). The eluted solution was adjusted to 1 mL using 0.1% Triton X-100 solution. Another 100 μL DOX solution without desalting process was also diluted to 1 mL using 0.1% Triton X-100 solution. The UV absorbance of both samples was measured at UV 480. To test the liposomal recovery, the DOXIL® liposome formulation was passed through Zeba™ spin desalting columns (7 kD MWCO) to remove the unencapsulated DOX and the eluted DOX liposomes were collected. 100 μL collected DOX liposomes were diluted to 1 mL using 0.1% Triton X-100 solution. Another 100 μL collected DOX liposomes were passed through the desalting column again, and the eluted solution was adjusted to 1 mL using 0.1% Triton X-100 solution. The DOX concentrations were quantified at UV 480 nm via a microplate-reader. The liposomal recovery % was calculated with the following formula:

$$Recovery\ \% = \frac{A_{(Before\ desalting)} - A_{(Background)}}{A_{(After\ desalting)} - A_{(Background)}} \bullet 100\%$$

At 0 h, 1 h, 3 h, 6 h, and 20 h after the start of the release assay, the experiment was stopped, and the dialysis devices (bags or tubes) were removed from the USP-4 apparatus. The solution inside the dialysis bags or tubes was carefully collected after gentle centrifuge (500 g × 2 min, room temperature), and the volume of the solution was determined. For sample processing, 100 μL solution was passed through the desalting columns at 1500 g for 1 min at the room temperature. The volume of the collected liposome was adjusted to 1 mL using 1% Triton X-100 water solution for liposomal DOX concentration quantification. To determine the total amount of doxorubicin, another 100 μL sample was withdrawn from the dialysis bags and diluted with 1% Triton X-100 to the final volume of 1 mL. The DOX concentrations were quantified at UV 480 nm via microplate-reader. The free DOX concentration in the sample was calculated with the following formula:

$$C_{free} = C_{total} - \frac{C_{liposmal}}{Liposomal\ Recovery\ \%}$$

where C_{free} is the concentration of free DOX in the sample, C_{total} is the concentration of the total DOX in the sample, $C_{liposomal}$ is the concentration of liposomal encapsulated DOX after passing through the desalting columns, and *Liposomal Recovery %* is the recovery of DOX liposomes from the desalting columns.

4.3.4 Model development

As seen in **Figure 4.1**, we denote the volume of the donor compartment as V_{in}, the volume of the receiver compartment as V_{out}, and the concentration of the released drug in the donor compartment and the receiver compartment as C_{in} and C_{out}, respectively. *A* is the surface area of the dialysis bags where diffusion occurs, and *P* is

the permeability or mass transfer coefficient of the drug passing through the dialysis membranes. To generate the mathematical model considering mass transport during dialysis, we assume that the drug concentration in each compartment is homogeneous for each of the models below.

4.3.4.1 Model 1: Dialysis with large receiver reservoir with constant volumes

For simplification, in this model, we assume that V_{in} and V_{out} are maintained constant during both the calibration and drug release experiments. We also assume that the volume of the receiver reservoir is much larger than that inside the bag, i.e., $V_{out} >> V_{in}$, and in most cases $C_{in} >> C_{out}$, holds during the dialysis process. Thus C_{out} is neglected in the driving force for diffusion across the dialysis membrane.

First, we consider the drug transport during the calibration experiment where drug translocates through the dialysis membranes in the absence of any drug carrier. A simple mass balance about the donor compartment accounting for the drug loss due to diffusion may be written as follows:

$$V_{in}\frac{dC_{in}}{dt} = -APC_{in} \quad (1)$$

Integrating (1) between times 0 and t gives:

$$C_{in} = C_0 e^{-\frac{A}{V_{in}}Pt} \quad (2)$$

where C_0 is the initial drug concentration in the dialysis bags. Therefore, there is a simple first-order decay of drug expected as the drug leaves the bag by simple diffusion.

In practice, it is most convenient to sample outside the bag. Therefore, the second mass balance is about drug transport to the receiver compartment, which may be written as follows:

$$V_{out}\frac{dC_{out}}{dt} = APC_{in} \quad (3)$$

Inserting (2) into (3), gives

$$V_{out}\frac{dC_{out}}{dt} = APC_0 e^{-\frac{A}{V_{in}}Pt} \quad (4)$$

Multiplying by V_{out} and dt on both sides, and integrating (4) from t = 0 to time t gives

$$C_{out} = \frac{C_0 V_{in}}{V_{out}}\left(1 - e^{-\frac{A}{V_{in}}Pt}\right) \quad (5)$$

Since V_{out} >> V_{in} (in our experiment, V_{out} = 49 x V_{in}), the final drug concentration in the receiver compartment (C_f) can be written as:

$$C_f = C_0 V_{in}/V_{out} \quad (6)$$

Inserting (6) into (5) gives the drug fraction released into the receiver compartment (f_{app}) as follows:

$$f_{app} = \frac{C_{out}}{C_f} = 1 - e^{-\frac{A}{V_{in}}Pt} \quad (7)$$

If the calibration and the drug release experiments are performed following the same protocol, which is the case for our study, A and V_{in} are kept the same in the two experiments, making AP/V_{in} as a constant denoted as k_{cal}. Thus,

$$f_{app} = \frac{C_{out}}{C_f} = 1 - e^{-k_{cal}\cdot t} \quad (8)$$

where k_{cal} is a calibration constant for a specific drug/bag combination determined by the slope of the linear decay of $ln(1-f_{app})$ vs. time.

Then, we consider the scenario where the nanocarriers are placed in the dialysis bag and the dialysis assay is performed under the same conditions as the calibration experiment. A mass balance around the solution in the bag may be written as follows:

$$V_{in}\frac{dC_{in}}{dt} = r(t) - APC_{in} \tag{9}$$

where *r(t)* is the mass release rate of the drug from the nanoparticle dosage form as a function of time. Rearranging and integrating (9) from *t* = 0 to time t gives:

$$\int_0^t r(t)dt = V_{in}\int_0^{C_{in}} dC_{in} + AP\int_0^t C_{in}dt \tag{10}$$

Normalizing the released mass of drug ($\int_0^t r(t)dt$) by the total drug mass, M_0, gives and initial expression for the actual drug release fraction from the formulation in the bag:

$$f(t) = \frac{\int_0^t r(t)dt}{M_0} = \frac{V_{in}C_{in}}{M_0} + \frac{AP}{M_0}\int_0^t C_{in}dt \tag{11}$$

Next, we consider the mass balance in the receiver compartment. As is the case without the nanocarrier, the mass balance in the receiver compartment is from (3). Rearranging (3) gives C_{in} as a function of the rate of change in concentration with time in the receiver compartment as follows:

$$C_{in} = \frac{V_{out}}{AP} \bullet \frac{dC_{out}}{dt} \tag{12}$$

Integrating (12) from *t* = 0 to time t gives

$$\frac{C_{out}V_{out}}{AP} = \int_0^t C_{in}dt \tag{13}$$

Inserting (12) and (13) into (11):

$$f(t) = \frac{\int_0^t r(t)dt}{M_0} = \frac{V_{in}V_{out}}{APM_0}\frac{dC_{out}(t)}{dt} + \frac{C_{out}\,V_{out}}{M_0} \tag{14}$$

Noting the apparent fraction drug released (f_{app}) assuming the negligible resistance of the dialysis bag is

$$f_{app} = \frac{C_{out} V_{out}}{M_0} \quad (15)$$

Taking the derivative of both side of equation (15) with respect to *t* gives:

$$\frac{df_{app}}{dt} = \frac{V_{out}}{M_0} \frac{dC_{out}}{dt} \quad (16)$$

Then (14) may be written as a function of f_{app} in a simple form after using (15) and (16)

$$f(t) = \frac{V_{in}}{AP} \frac{df_{app}}{dt} + f_{app} \quad (17)$$

Finally noting the definition for k_{cal} ($\equiv AP/V_{in}$), (17) becomes:

$$f = \frac{1}{k_{cal}} \frac{df_{app}}{dt} + f_{app} \quad (18)$$

and from (12), (16) and the expression for k_{cal}, the free drug concentration in the donor compartment is

$$C_{in} = \frac{M_0}{V_{in} k_{cal}} \cdot \frac{df_{app}}{dt} \quad (19)$$

Hence, from the calibration constant, k_{cal}, and the measured and fitted apparent fraction release kinetics f_{app}, the actual release kinetics of the formulation (i.e., *f* vs. *t*) may be readily determined from (18). Moreover, the value of C_{in}, the concentration of drug inside the bag, may be also predicted from (19).

4.3.4.2 Model 2: Dialysis under conditions with constant volumes and where the concentration of drug in the receiver media cannot be ignored

In the derivation of the Model 1, we assume that the C_{in} >> C_{out} during the entire release experiment. However, depending on the setup of the dialysis assays, this assumption may not always be met. To address this limitation, we revise the Model 1 by considering the presence of C_{out} in the driving force for diffusion. The volume of the donor compartment is still assumed to keep constant during dialysis.

In the calibration experiment, no drug carrier is present, and all drug molecules are dissolved in the media inside the dialysis bag. Since V_{in} << V_{out}, C_{out} may still be negligible in the early phase of the translocation. For example, V_{out} is 49-fold larger than V_{in} in our experimental setup. In this case, C_{in} remains ten times higher than C_{out} before 83% drug is translocated in the receiver compartment. Thus, eq (1) – (8) still holds true in the early stages of the calibration experiments.

For drug release assays with a nanocarrier, under the assumptions of Model 2, the mass balance in the donor compartment is revised from Model 1 as follows:

$$V_{in}\frac{dC_{in}}{dt} = r(t) - AP(C_{in} - C_{out}) \tag{20}$$

The new mass balance in the receiver compartment is:

$$V_{out}\frac{dC_{out}}{dt} = AP(C_{in} - C_{out}) \tag{21}$$

Solving (20) and (21) yields the actual drug release fraction as follows (the complete derivation process is provided in the Supplementary Materials):

$$f = \frac{V_{in}C_{out}}{M_0} + \frac{1}{k_{cal}} \cdot \frac{df_{app}}{dt} + f_{app} \tag{22}$$

With the time-dependent C_{in} as

$$C_{in} = C_{out} + \frac{M_0}{V_{in}\,k_{cal}} \cdot \frac{df_{app}}{dt} \tag{23}$$

4.3.4.3 Model 3: Dialysis with volume changes and appreciable receiver drug concentration

During the dialysis process, the volume of the donor compartment and the receiver compartment may be subject to change due to osmotic pressure and membrane swelling. To account for the volume change of the donor compartment, the mass balance in the donor and the receiver compartment can be rewritten as:

$$\frac{d(C_{in}V_{in})}{dt} = r(t) - AP(C_{in} - C_{out}) \quad (24)$$

$$\frac{d(C_{out}V_{out})}{dt} = AP(C_{in} - C_{out}) \quad (25)$$

Note that for conventional dialysis bags, the surface area *A* typically remains the same when V_{in} changes. For dialysis tubes such as the Float-A-Lyzer apparatus, since the bottom area is fixed, *A* changes with V_{in}, with the fixed ratio of $A/V_{in} = 2/R$, where the *R* is the radius of dialysis tubes. Thus, the two conditions should be solved respectively (see Supplementary Materials), which summarized below.

For conventional dialysis bags:

$$f = f_{app} + F_V\left(\frac{V_{in(0)}\,C_{out}}{M_0} + \frac{1}{k_{cal}} \cdot \frac{df_{app}}{dt}\right) \quad (26)$$

$$C_{in} = C_{out} + \frac{M_0}{V_{in(0)}} \cdot \frac{1}{k_{cal}} \cdot \frac{df_{app}}{dt} \quad (27)$$

For dialysis tubes with fixed bottom areas:

$$f = f_{app} + \frac{1}{k_{cal}} \cdot \frac{df_{app}}{dt} + F_V \frac{V_{in(0)}\,C_{out}}{M_0} \quad (28)$$

$$C_{in} = C_{out} + \frac{1}{F_V} \cdot \frac{M_0}{V_{in(0)}} \cdot \frac{1}{k_{cal}} \cdot \frac{df_{app}}{dt} \quad (29)$$

where the volume correction factor $F_V = \frac{V_{in}}{V_{in\,(0)}}$, $V_{in(0)}$ is the initial volume of the donor compartment and V_{in} is the time-dependent volume of the donor compartment.

4.3.5 Data analysis

For the calibration experiment, three parallel runs were made for each dialysis membrane and the apparent drug release fraction (f_{app}) was recorded. For each run, ln(1-f_{app}) was plotted against time (t) using the data of the first 4 h. Simple linear regression was used to fit each scatter plot. The negative slope of the linear regression was used for k_{cal} of this dialysis membrane according to (8).

For the drug release experiment, three parallel runs were made for each dialysis membrane. The time-dependent apparent drug release fraction (f_{app}) was recorded as described above and plotted against time (t). The f_{app} vs t scatter plots were fitted with the Weibull function

$$f_{app} = 1 - e^{-at^b} \tag{30}$$

where a is the scale parameter while b is the shape parameter. Specifically, when Weibull function could not fit the data well, which was the case for 20kD CE release data (owing to constrained diffusion), the data were fitted by a linear function ($f_{app} = ct + d$). After the parameters were determined using nonlinear fitting in R (version 3.4.3), the time derivative function df_{app}/dt was calculated. Then, the fraction of drug release from nanocarriers (f) and drug concentration within the bag (C_{in}) were calculated by the equations derived by Model 1, 2 or 3.

For data simulation, based on the assumption that all parameters are normally distributed, at each defined time points from time zero to 20 hours, 100 values of parameters including a, b, and k_{cal} were simulated by random sampling from the respective normal distribution with mean and standard error estimated from previous model fitting. Fraction of drug release from nanocarriers (f) and drug concentration

within the bag (C_{in}) were calculated together with mean and 95% confidence interval by the equations derived by Model 3. To simplify the simulation process, a fixed value of V_{in}, which was the average value of V_{in} at 24 h time point of all runs, was used when needed.

4.4 Results and Discussion

4.4.1 Calibration of doxorubicin diffusion through dialysis membranes

In the calibration experiments, doxorubicin solution was placed in different dialysis bags to determine the membrane permeation kinetics. Only data during the first 4 h were fitted, since the assumption of $C_{in} >> C_{out}$ only holds true when less than 85% drug has been translocated to the receiver compartment. As seen in **Figure 4.2**, a linear relationship was found between $ln(1-f_{app})$ and time for every dialysis membrane, confirming first-order diffusion kinetics of free doxorubicin molecules through dialysis membranes as described by eq (8). The calibration constant (k_{cal}), which is the negative of the slope of these kinetic curves, was calculated and listed in **Table 4.1**. As expected, for the dialysis membranes of the same type, k_{cal} increased with the increase in MWCO, indicating that the barrier effects of dialysis membranes decreased as MWCO increased. When comparing dialysis membranes of different materials, CE membranes have significantly lower k_{cal} compared to RC membranes with the same MWCO, indicating that CE membranes have a higher resistance to doxorubicin diffusion compared to RC membranes. Such results suggested that both MWCO and the membrane type affect the barrier properties of the dialysis membranes, and choosing dialysis membranes solely based on MWCO may not be reliable. For example, it has

been suggested that the dialysis membrane for drug release assays should have an MWCO which is at least 100 times higher than the molecular weight of the drug molecule[196]. The molecular weight of DOX is 543.5 g/mol, requiring dialysis membranes to have an MWCO of > 50 kD to meet the criteria. However, the CE membrane with 50 kD exhibited medium permeation, whereas the RC membrane with MWCO of 20 kD was associated with a faster translocation of DOX. The different permeation kinetics of membranes made by different materials may be related to the porosity of the dialysis membranes or the interactions between drug molecules and membrane materials. However, few research articles have been published so far to address the impact of the dialysis material on translocation rate of drugs.

Table 4.1 Calibration constant k_{cal} of different membranes for free DOX from **Figure 4.2(B).**

Membrane	k_{cal} (h^{-1})[a]
8-10 kD CE	0.019 ± 0.003
20 kD CE	0.055 ± 0.004
50 kD CE	0.534 ± 0.067
100 kD CE	0.690 ± 0.013
300 kD CE	0.862 ± 0.164
8-10 kD RC	0.733 ± 0.009
20 kD RC	0.812 ± 0.074

[a] The results are presented as mean±SEM (n = 3). Least squares linear regression resulted in $r^2 > 0.98$.

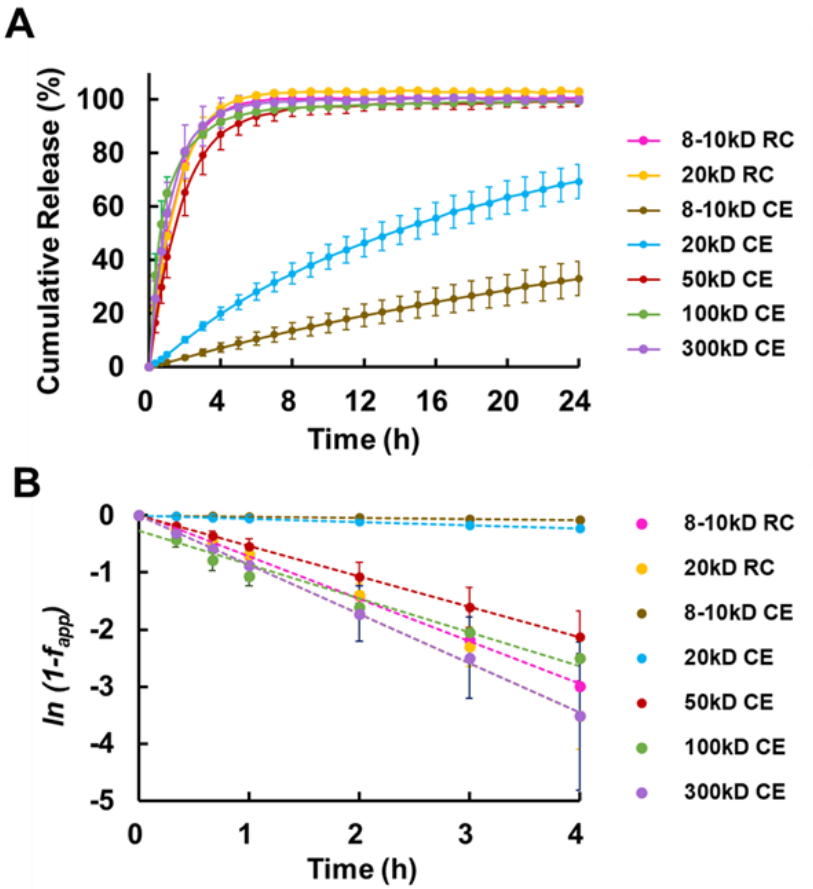

Figure 4.2 DOX diffusion kinetics through different dialysis membranes. (A) Cumulative release of DOX from nanocarrier-free drug solution through different dialysis membranes (lines drawn through data). (B) The k_{cal} was calculated from the linear regression of the first 4 h free DOX release of the plot according to (8). Dashed lines are least squares linear regression lines with kcal listed in **Table 4.1**

Based on the k_{cal} determined in this section, two dialysis membranes with rapid and medium permeation rates to DOX, the RC membrane with MWCO 20 kD and the CE membrane with MWCO 50 kD, were selected for evaluation of DOXIL® release and evaluation of the mathematical methods to determine release on the nanoparticle side of the membrane.

4.4.2 Fitting apparent release data

In order to obtain the time derivative of the apparent drug release fraction curve (df_{app}/dt), the f_{app} vs. time curve were fitted by Weibull function except for 20kD CE membranes where a linear regression is used.. It is worth noting that while the Weibull function has been commonly used to fit drug release kinetics data [197], the choice of the function used for model fitting is made on the case-by-case basis. The following criteria are applied to choose the proper function to fit the apparent drug release data. First, there must be a good agreement between the experimental data and the fitted line. When such agreement can be achieved by several functions, the function with fewer parameters and least standard errors for the estimates of the parameters is more favorable for the simulation process. For example, when developing our approach we initially fitted the data with 4th and 5th order polynomial functions. However, use of the polynomial fits resulted in poor predictions of the initial release data, which resulted in inaccurate predictions of C_{in} in early time points. Furthermore, we observed large standard errors of the parameter estimates when fitting data with polynomial functions, which, when introduced to the simulation process, produced a wide confidence interval of the predicted values and weakened the usefulness of the model. On the other hand, the Weibull functions fits did not have this issue and were therefore preferred.

4.4.3 Applying mathematical models to predict actual DOXIL® release kinetics

In dialysis assays, the actual fraction of drug released (f) occurring inside the dialysis bag can be written as follows:

$$f = f_{app} + \frac{M_{in}}{M_0}$$

As seen above, f_{app} represents the apparent fraction of drug released (i.e., the fraction of free drug that has accumulated in the receiver compartment), M_{in} is the amount of free drug in the donor compartment, and M_0 is the total amount of drug in the formulation. In practice, M_{in}/M_0 is often neglected due to difficulty in monitoring the free drug concentration in the dialysis bags and the assumption that the released drug is rapidly transported to the receiver compartment and/or the amount of drug in the bag is small compared to that outside the bag. However, determining M_{in} is important if it is desired to know accurately the actual drug release fraction *f.*

By applying the k_{cal} determined in the calibration experiments and fitting the f_{app} release kinetics to the Weibull function, three models developed with different assumptions were used to calculate the time-dependent free drug concentration in the donor compartment. The calculated values are compared with the experimental data. As seen in **Figure 4.3**, Model 1 predicted drug concentration inside the bag with a good agreement to the experimental data in the first few hours, but failed to predict well the data at later stages of the release. This discrepancy can be attributed to the fact that the assumption $C_{in} >> C_{out}$ is compromised at the late stage of the release. When taking the diminishing concentration gradient into consideration, Model 2 presented better C_{in} predictions of the experimental data. The Model 2 was further revised to account for the volume change in dialysis tubes during the experiment. As seen in **Figure 4.4**, there was a small yet significant decrease in the volume inside the dialysis bags during the first 3 h of dialysis, after which the volume kept constant. While it is possible to mathematically describe the volume change and incorporate it into the general model, for simplification purposes, we used the equilibrium volume to calculate the volume

correction factor F_v in our calculation. The kinetics of C_{in} predicted by Model 3 demonstrated the closest agreement with the experimental data.

Model 3 was then applied to calculate the actual drug release kinetics from the apparent drug release data. As seen in **Figure 4.5**, while the apparent drug release data significantly underestimated the actual drug release fraction, a good agreement between the predicted value and the experimental value of actual drug release fraction was found in both assays performed in 20 kD RC membranes and 50 kD CE membranes. Thus, Model 3 served as a reliable tool to determine the actual drug

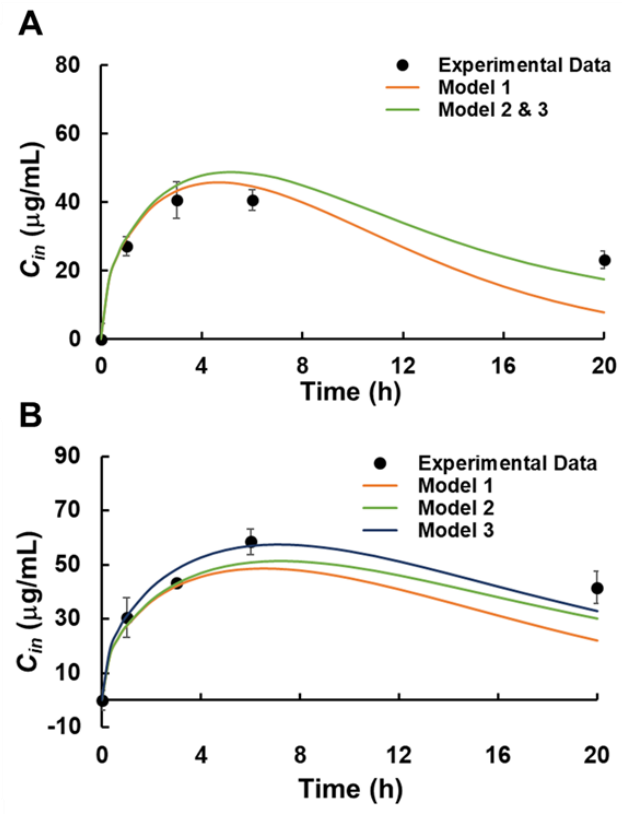

Figure 4.3 Predicted and observed free DOX concentrations in the donor compartment (C_{in}) during release from DOXIL® in (A) 20 kD RC membrane dialysis bags and (B) 50 kD CE membrane dialysis tubes. The experimental data are presented as mean ± SD (n = 3). Error bars not shown when smaller than symbols.

release kinetics from apparent drug release data of dialysis methods, allowing for a more proper data interpretation.

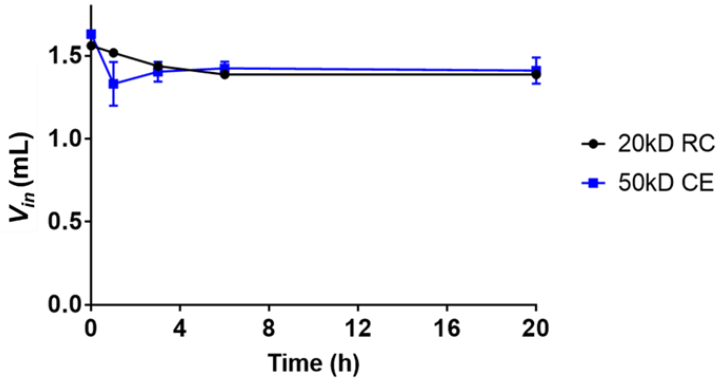

Figure 4.4 Volumes of donor compartments (V_{in}) during the release process. Lines drawn through data. The results are presented as mean ± SD (n = 3).

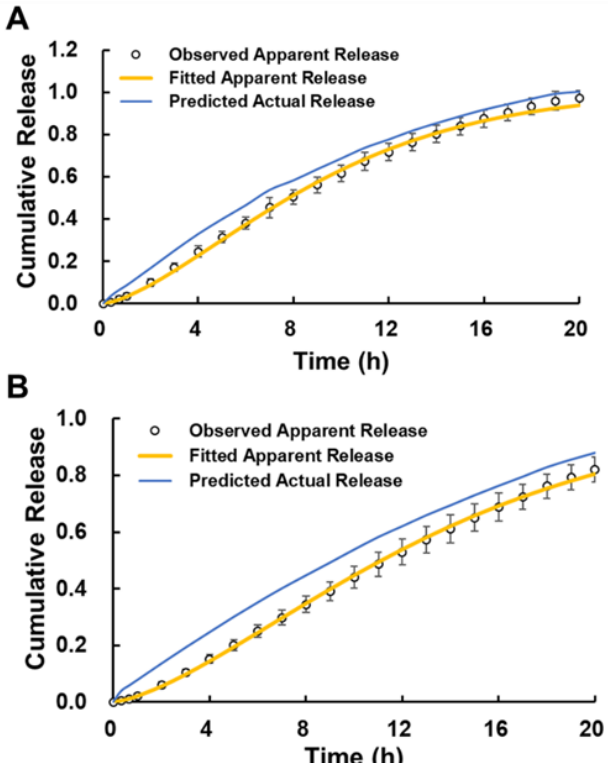

Figure 4.5 Predicted actual (*f*) and apparent (f_{app}) cumulative release kinetics of DOX from DOXIL®. Analysis and experiments were performed using (A) 20 kD RC membrane dialysis bags and (B) 50 kD CE membrane dialysis tubes. The predicted actual release was performed with Model 3 and fitted apparent release curve were performed with Weibull functions. The results are presented as mean ± SD (n = 3).

4.4.4 The impact of dialysis membrane on drug release

Model 2 was further used to calculate the free drug concentration in the donor compartment (C_{in}) as well as the actual drug release kinetics (f) from the apparent drug release profiles derived from dialysis assays using different membranes. As seen in **Figure 4.6B**, increased C_{in} was observed in the early few hours of dialysis in each dialysis membrane. The accumulation of the free drug in the dialysis bags indicates that the drug release rate from the liposomes exceeded the drug permeation rate through the dialysis membranes. Over this period, dialysis membrane diffusion kinetics, rather than the actual drug release kinetics from the nanocarrier, was the largest determinant of the drug translocation to the receiver compartment (that is, the apparent drug release kinetics). For dialysis membranes with higher barrier effects like the MWCO 20 kD CE membrane, the membrane diffusion remained as the rate-limiting factor throughout the dialysis process, as evidenced by the high free drug concentration in the donor compartment. In addition, we noticed that there was a large variance in apparent drug release in 3 repeated runs using the 20 kD CE tubes, which led to a more scattered simulation result compared to those of other membranes. Since the apparent drug release profile is predominately controlled by membrane diffusion, such large variance can be attributed to the variability between different 20 kD CE dialysis tubes. For dialysis membranes with faster drug permeation rates such as the MWCO 20 kD RC membrane and the MWCO 300 kD CE membrane, while they have a shorter membrane-dominating phase and a lower drug accumulation inside the dialysis bags, the membrane diffusion was still the largest rate-limiting factor in the first 4 hours.

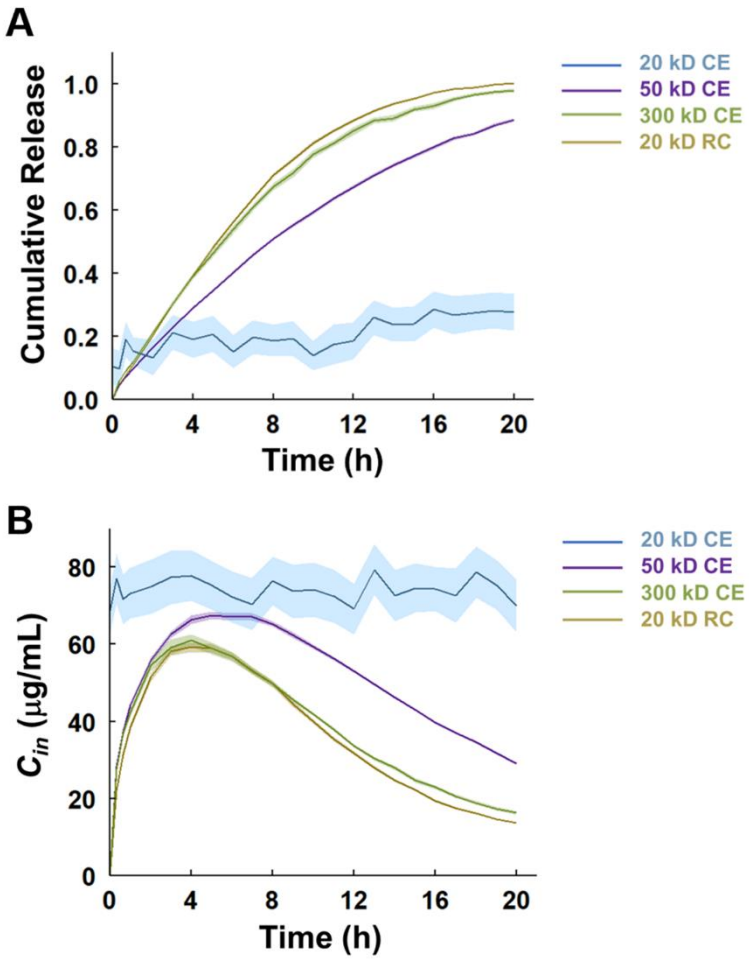

Figure 4.6 (A) Predicted liposome cumulative release kinetics of DOX from DOXIL® from different dialysis devices and (B) Predicted free drug concentration in the donor compartment (C_{in}). The shade indicates 95% confidence interval (CI) generated by data simulation.

The actual drug release kinetics was also predicted for additional dialysis bags. As shown in **Figure 4.6A**, the actual drug release rate inside the dialysis bags was negatively correlated with the k_{cal} of the membrane. This can be attributed to the accumulation of free drug inside the dialysis bags, which violates an effective sink conditions for the drug releasing liposome. In dialysis settings, the sink condition is assumed to be achieved by having a large volume of release media in the receiver

compartment which is 10 – 20 times higher than the volume required for the saturated drug solution [198]. The underlying assumption of this practice is that the free drug can quickly equilibrate across the dialysis membrane, and thus maintaining a low free drug concentration inside the dialysis bag. However, this assumption may not always be true due to the barrier effects of dialysis membranes. As seen in **Figure 4.6B**, the free drug concentration during the dialysis was 2 – 8 times higher than the final equilibrium concentration of doxorubicin outside the bag, which was 10 μg/ml. This effect is more prominent for dialysis membranes with low permeability coefficients. For example, for the CE membrane with MWCO of 20 kD, the actual drug release was much slower compared to other dialysis membranes, and approximately followed zero-order kinetics. In this case, the barrier effects of the dialysis membrane not only delayed the apparent drug release profile but also hindered the 'actual' drug release, indicating the membrane was unsuitable to evaluate drug release kinetics under these conditions. Analyzing the free drug concentration inside the dialysis bags using the models developed in the present paper may serve as a useful tool for the methodological evaluation of dialysis assays.

4.5 Conclusion

Despite the common use of dialysis methods for *in vitro* drug release kinetics studies, several common issues associated with their use such as barrier effects of dialysis membranes and violated sink conditions decrease assay accuracy. These limitations often lead to underestimated drug release rate, which may be wrongly attributed to the sustained release of drug from the nanoparticles without proper methodology evaluation and data interpretation. In the present study, a straightforward

strategy to manage these effects is proposed independent of the drug carrier in the bag. First, the dialysis membrane is calibrated by a diffusion experiment across the dialysis membrane without the nanocarrier. After fitting a suitable mathematical expression to the apparent drug release data from the nanocarrier obtained from the conventional dialysis assays, a mathematical model can be used to predict that actual drug release kinetics. In the cases where the volume changes in the dialysis bags, a volume correction factor can be added to the mathematical model to enable a better prediction. An excellent agreement is observed between the predicted actual release kinetics and concentration in the bag and the experimentally determined values. Our model not only enables the proper interpretation of the data from dialysis studies but also helps to evaluate the dialysis methodology applied to *in vitro* drug release assays.

4.6 Supplementary Materials

4.6.1 Materials and Method

4.6.1.1. Permeation kinetics of DOX in different buffers

DOX solution was prepared with the concentration of 2 mg/mL either in the same buffer as DOXIL® formulation (10 mM Histidine•HCl, 10% sucrose (w/v), pH 6.5) or in the release media (100 mM NH_4HCO_3, 5% sucrose (w/v), 75 mM MES, 5% HP-CD (w/v), and 0.02% NaN_3. pH 6.0). A volume of 0.4 mL DOX solution was added to the dialysis bags together with 1.2 mL release media. The dialysis tubes were inserted to the flow-through cells of the USP-4 apparatus. 78.4 mL release media was added into the media reservoir to achieve the total volume of ~80 mL. To determine the UV absorbance of doxorubicin once completely released from the carriers, a free DOX control was set by directly placing 0.4 mL DOX•HCl stock solution and 79.6 mL release media in the media reservoir. The apparent cumulative drug release was calculated with the following formula:

$$\text{Cumulative release } \% = \frac{A_{(Released\ DOX)} - A_{(Background)}}{A_{(Free\ DOX\ control)} - A_{(Background)}} \bullet 100\%$$

Where $A_{(Released\ DOX)}$ is the UV absorbance of the released DOX in bulk solution outside the dialysis membrane, $A_{(Free\ DOX\ control)}$ is the UV absorbance of the control DOX solution, and $A_{(Background)}$ is the UV absorbance of blank release media.

4.6.1.2 Determination of the recovery of desalting columns

To test the capacity of desalting columns to remove free DOX, 100 μL DOX stock solution (2 mg/mL) was passed through Zeba™ spin desalting columns (7 kD MWCO). The eluted solution was adjusted to 1 mL using 0.1% Triton X-100 solution. Another 100

μL DOX solution without desalting process was also diluted to 1 mL using 0.1% Triton X-100 solution. The UV absorbance of the both samples was measured at UV 480.

To test the liposomal recovery, the DOXIL® liposome formulation was passed through Zeba™ spin desalting columns (7 kD MWCO) to remove the unencapsulated DOX and the eluted DOX liposomes were collected. 100 μL collected DOX liposomes were diluted to 1 mL using 0.1% Triton X-100 solution. Another 100 μL collected DOX liposomes were passed through the desalting column again, and the eluted solution was adjusted to 1 mL using 0.1% Triton X-100 solution. The DOX concentrations were quantified at UV 480 nm via a microplate-reader. The liposomal recovery % was calculated with the following formula:

$$\text{Recovery } \% = \frac{A_{(Before\ desalting)} - A_{(Background)}}{A_{(After\ desalting)} - A_{(Background)}} \bullet 100\%$$

4.6.1.3. Model 2: Dialysis under conditions with constant volumes and where the concentration of drug in the receiver media cannot be ignored

For drug release assays with nanoparticles, in the non-sink conditions, the mass balance in the donor compartment is revised from the Model 1 as follows:

$$V_{in}\frac{dC_{in}}{dt} = r(t) - AP(C_{in} - C_{out}) \quad \text{(S1)}$$

where *A* is the surface area of the dialysis membrane, *P* is permeation coefficient, C_{in} and C_{out} are the free drug concentration of the donor and the receiver compartments respectively, V_{in} is the volume of the donor compartment, and *r(t)* is the mass release rate of the drug from the nanocarriers.

Rearranging and integrating (S1) gives:

$$\int_0^t r(t)dt = V_{in}\int_0^{C_{in}} dC_{in} + AP\int_0^t (C_{in} - C_{out})\,dt \quad \text{(S2)}$$

Nnormalizing the released mass of drug ($\int_0^t r(t)dt$) by the total drug mass, M_0, gives an initial expression for fractional drug release from the formulation in the bag as follows:

$$f = \frac{\int_0^t r(t)dt}{M_0} = \frac{V_{in}C_{in} + AP\int_0^t (C_{in} - C_{out})\,dt}{M_0} \quad \text{(S3)}$$

Similarly, the mass balance in the receiver compartment can be written as follows:

$$V_{out}\frac{dC_{out}}{dt} = AP(C_{in} - C_{out}) \quad \text{(S4)}$$

Rearranging (S4) gives C_{in} as a function of the concentration in the outside media and its time derivative as follows:

$$C_{in} = \frac{V_{out}}{AP} \bullet \frac{dC_{out}}{dt} + C_{out} \quad \text{(S5)}$$

And integrating (S4) gives

$$\frac{V_{out}C_{out}}{AP} = \int_0^t (C_{in} - C_{out})dt \quad \text{(S6)}$$

Inserting (S5) and (S6) into (S3):

$$f = \frac{V_{in}V_{out}}{APM_0} \bullet \frac{dC_{out}}{dt} + \frac{C_{out}V_{in}}{M_0} + \frac{V_{out}C_{out}}{M_0} \quad \text{(S7)}$$

Noting the apparent fraction drug released from the dialysis bag is

$$f_{app} = \frac{V_{out}C_{out}}{M_0} \quad \text{(S8)}$$

and from the related rate of (S8),

$$\frac{df_{app}}{dt} = \frac{V_{out}}{M_0} \bullet \frac{dC_{out}}{dt} \quad \text{(S9)}$$

Then (S7) may be written as a function of f_{app} as follows after using (S8) and (S9)

$$f = \frac{V_{in}}{AP} \bullet \frac{df_{app}}{dt} + \frac{C_{out}V_{in}}{M_0} + f_{app} \quad \text{(S10)}$$

Noting again that $k_{cal} \equiv \frac{AP}{V_{in}}$, (S10) can be re-written as

$$f = \frac{1}{k_{cal}} \bullet \frac{df_{app}}{dt} + \frac{C_{out}V_{in}}{M_0} + f_{app} \quad \text{(S11)}$$

Since *f* represents the total free drug fraction, and f_{app} is the fraction of free drug in the receiver compartment, the amount of free drug in the donor compartment, M_{in}, can be written as:

$$M_{in} = M_0(f - f_{app}) = M_0(\frac{1}{k_{cal}} \bullet \frac{df_{app}}{dt} + \frac{C_{out}V_{in}}{M_0}) \quad \text{(S12)}$$

The free drug concentration in the donor chamber during the dialysis release experiment can be written as:

$$C_{in} = \frac{M_{in}}{V_{in}} = \frac{M_0}{V_{in}} \bullet \frac{1}{k_{cal}} \frac{df_{app}}{dt} + C_{out} \quad \text{(S13)}$$

4.6.1.4. Model 3: Dialysis with volume changes and appreciable receiver drug concentration

During the dialysis process, the volume of the donor compartment may change due to swelling of the dialysis bags or osmotic pressure differences between donor and receiver solutions. We denote the initial volume of the donor chamber, which is the same in the calibration experiment and drug release experiment, as $V_{in(0)}$. The time-dependent donor chamber volume is denoted as $V_{in(t)}$. The volume of the receiver chamber is denoted as V_{out}. As $V_{out} >> V_{in(t)}$ and the change of the $V_{in(t)}$ is very small, V_{out} can be treated as a constant during the dialysis process.

Two kinds of dialysis devices are considered. For conventional dialysis bags, their surface area typically keeps constant despite the slight changes of volume inside the dialysis bags. For pre-made dialysis tubes with fixed bottom area such as Float-A-Lyzer devices, the area of the dialysis membranes where the diffusion occurs changes proportionally with the volume inside the dialysis tubes. These two conditions are discussed separately below.

4.6.1.4.1 For dialysis devices with fixed *A*.

For drug release assays with nanoparticles, the mass balance in the donor compartment is revised from the Model 2 as follows:

$$\frac{dM_{in}}{dt} = r(t) - AP(C_{in} - C_{out}) \quad \text{(S14)}$$

where M_{in} is the free drug mass inside the dialysis bags.

Rearranging and integrating (S14) gives:

$$\int_0^t r(t)dt = \int_0^{M_{in}} dM_{in} + AP\int_0^t (C_{in} - C_{out})\, dt \quad \text{(S15)}$$

Normalizing the released mass of drug ($\int_0^t r(t)dt$) by the total drug mass, M_0, gives an initial expression for drug release fraction from the formulation in the bag:

$$f = \frac{\int_0^t r(t)dt}{M_0} = \frac{M_{in} + AP\int_0^t (C_{in} - C_{out})\, dt}{M_0} \quad \text{(S16)}$$

Noting $M_{in} = C_{in} V_{in(t)}$, where $V_{in(t)}$ is the time-dependent volume in the dialysis bags, (S16) can be rewriten as:

$$f = \frac{C_{in} V_{in(t)} + AP\int_0^t (C_{in} - C_{out})\, dt}{M_0} \quad \text{(S17)}$$

Again, the mass balance in the receiver compartment can be written as (S4) – (S6). Inserting (S5) and (S6) into (S17) gives:

$$f = \frac{V_{in(t)} V_{out}}{APM_0} \bullet \frac{dC_{out}}{dt} + \frac{V_{in(t)} C_{out}}{M_0} + \frac{V_{out} C_{out}}{M_0} \quad \text{(S18)}$$

Again, note the apparent fraction drug released assuming the negligible resistance of the dialysis bag is

$$f_{app} = \frac{V_{out}\, C_{out}}{M_0} \quad \text{(S8)}$$

and from (S8):

$$\frac{df_{app}}{dt} = \frac{V_{out}}{M_0} \bullet \frac{dC_{out}}{dt} \quad \text{(S9)}$$

Noting that $k_{cal} \equiv \frac{AP}{V_{in(0)}}$, (S18) may be simplified as follows:

$$f = \frac{V_{in(t)}}{V_{in(0)}}\left(\frac{1}{k_{cal}} \bullet \frac{df_{app}}{dt} + \frac{V_{in(0)}C_{out}}{M_0}\right) + f_{app} \quad \text{(S19)}$$

We denote the volume correction factor $F_v \equiv \frac{V_{in(t)}}{V_{in(0)}}$, and then (S19) can be rewritten as

$$f = F_v\left(\frac{1}{k_{cal}} \bullet \frac{df_{app}}{dt} + \frac{V_{in(0)}C_{out}}{M_0}\right) + f_{app} \quad \text{(S20)}$$

The free drug concentration in the donor chamber during the dialysis process can be written as:

$$C_{in} = \frac{M_0(f - f_{app})}{V_{in(t)}} = \frac{M_0}{V_{in(0)}} \bullet \frac{1}{k_{cal}} \frac{df_{app}}{dt} + C_{out} \quad \text{(S21)}$$

4.6.1.4.2 For dialysis devices with fixed $V_{in(t)}/A$.

For dialysis devices with fixed bottom area, such as Float-A-Lyzer tubes, the area of the dialysis membrane changes as the volume inside the dialysis bags change. The time-dependent dialysis membrane area is denoted as *A(t).* For a dialysis tube, the ratio of $V_{in(t)}$ to *A(t)* is a constant.

$$\frac{V_{in(t)}}{A(t)} = \frac{\pi R^2 h}{2\pi R h} = \frac{R}{2} \quad \text{(S22)}$$

where *R* is the radius of the tube and *h* is the height of the solution inside the tube. With *A(t)* as a variable, in the drug release assay, the mass balance in the donor compartment is expressed as (S23):

$$\frac{dM_{in}}{dt} = r(t) - A(t)P(C_{in} - C_{out}) \quad \text{(S23)}$$

where M_{in} is the free drug mass inside the dialysis bag.

Rearranging and integrating (S23) gives:

$$\int_0^t r(t)dt = \int_0^{M_{in}} dM_{in} + \int_0^t PA(t)(C_{in} - C_{out})\, dt \quad \text{(S24)}$$

Normalizing the released mass of drug ($\int_0^t r(t)dt$) by the total drug mass, M_0, gives an initial expression for drug release fraction from the formulation in the bag:

$$f = \frac{\int_0^t r(t)dt}{M_0} = \frac{M_{in} + \int_0^t PA(t)(C_{in} - C_{out})\,dt}{M_0} \quad \text{(S25)}$$

Rearranging (S4) gives C_{in} as a function of the concentration in the outside media and its time derivative as follows:

$$C_{in} = \frac{V_{out}}{A(t)P} \bullet \frac{dC_{out}}{dt} + C_{out} \quad \text{(S26)}$$

and multiplying by V_{in}/M_0 gives the first part on the right-hand-side of (S25)

$$\frac{M_{in}}{M_0} = \frac{V_{in(t)}V_{out}}{A(t)PM_0} \bullet \frac{dC_{out}}{dt} + \frac{C_{out}V_{in(t)}}{M_0} \quad \text{(S27)}$$

At the same time, the mass balance in the receiver compartment can be written as follows:

$$V_{out}\frac{dC_{out}}{dt} = A(t)P(C_{in} - C_{out}) \quad \text{(S28)}$$

And integrating (S28) gives

$$V_{out}C_{out} = \int_0^t A(t)P(C_{in} - C_{out})dt \quad \text{(S29)}$$

Inserting (S27) and (S28) into (S25) gives:

$$f = \frac{V_{in(t)}V_{out}}{A(t)PM_0} \bullet \frac{dC_{out}}{dt} + \frac{C_{out}V_{in(t)}}{M_0} + \frac{V_{out}C_{out}}{M_0} \quad \text{(S30)}$$

Again, note the apparent fraction drug released assuming the negligible resistance of the dialysis bag is

$$f_{app} = \frac{V_{out}C_{out}}{M_0} \quad \text{(S8)}$$

and again with the related rate from (S8),

$$\frac{df_{app}}{dt} = \frac{V_{out}}{M_0} \bullet \frac{dC_{out}}{dt} \quad \text{(S9)}$$

Then, from (S22), (S30) may be simplified as follows:

$$f = \frac{R}{2P} \bullet \frac{df_{app}}{dt} + F_v \frac{C_{out} V_{in(0)}}{M_0} + f_{app} \quad \text{(S31)}$$

where F_v is the volume correction factor $F_v \equiv \frac{V_{in(t)}}{V_{in(0)}}$

It is worth noting that for the calibration experiment using the same dialysis tubes, the volume/area ratio (V_{in}/A) also equals R/2. Thus,

$$k_{cal} = \frac{AP}{V_{in}} = \frac{2P}{R} \quad \text{(S32)}$$

Inserting (S32) to (S31) gives

$$f = \frac{1}{k_{cal}} \bullet \frac{df_{app}}{dt} + F_v \frac{C_{out} V_{in(0)}}{M_0} + f_{app} \quad \text{(S33)}$$

The free drug concentration in the donor chamber during the dialysis process can be written as:

$$C_{in} = \frac{M_0 (f - f_{app})}{V_{in(t)}} = \frac{M_0}{V_{in(0)} F_v} \bullet \frac{1}{k_{cal}} \bullet \frac{df_{app}}{dt} + C_{out} \quad \text{(S33)}$$

4.6.1.5 Data processing

The apparent drug release data (f_{app}) of three parallel runs for each dialysis membrane were recorded. The f_{app} vs t scatter plots were fitted with Weibull function $f_{app} = 1 - e^{-at^b}$ where a is the scale parameter while b is the shape parameter. Specifically, when Weibull function cannot fit the data well, which is the case for 20kD CE release data, the data were fitted by a linear function $f_{app} = ct + d$ to get a better fit. After the parameters were determined using nonlinear fitting in R (version 3.4.3),

4.6.2 Results

4.6.2.1 Permeation kinetics of DOX in different buffers

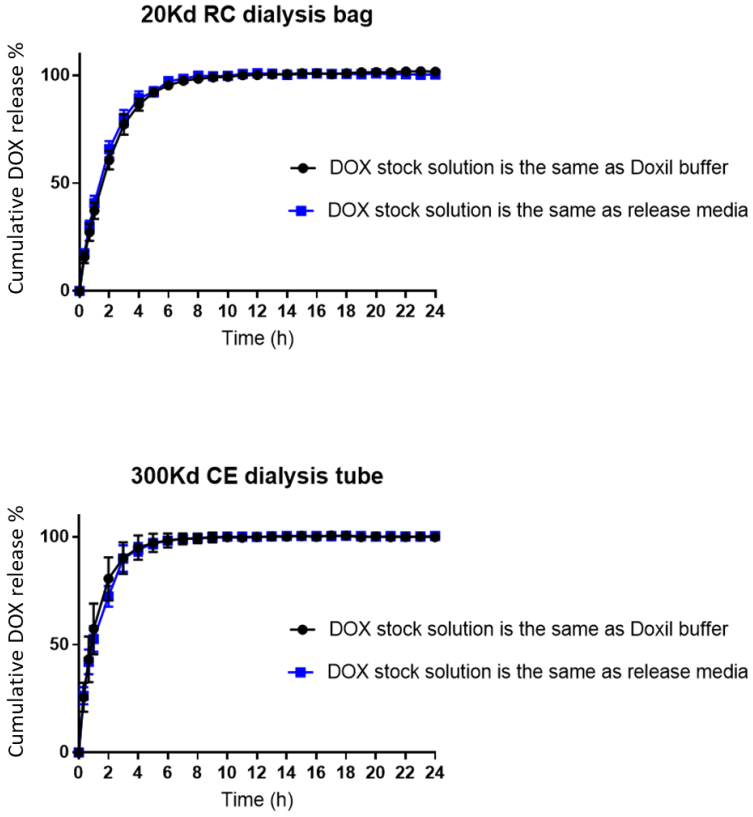

Figure 4.S1. Permeation kinetics of DOX solutions in 20 kD RC (A) and 300 kD CE (B) dialysis membranes for different media inside the dialysis tubes.

DOX liposomes in DOXIL® formulation were dispersed in a different buffer solution from the release media. During the dialysis, different buffers in both sides of dialysis membranes exchanged their components to reach equilibrium, resulting in a changing buffer environment inside the dialysis bags. This causes a concern that the permeation coefficient of DOX across the membrane may change as the solute components change inside the membrane, making it a variable in the mathematical model. To investigate whether DOX presented different permeation kinetics in the different buffers, we performed calibration experiments with DOX solutions in the two

different buffers. As seen in **Figure 4.S1**, no significant difference was found in the permeation kinetics of two DOX solutions in 20 kD RC and 300 kD CE membranes. Thus, the changing buffer has little effect on the permeation coefficient of DOX.

4.6.2.2 Determination of the recovery of desalting columns

The desalting columns are found to completely remove free DOX from the solution. The liposomal recovery of the desalting columns was 95.3% ± 0.6% (mean ± SEM, n = 3).

4.6.2.3 Fitting apparent fraction release kinetics

The apparent drug release data of DOXIL® from 20kD RC dialysis bags, 50kD CE, and 300kD CE dialysis tubes were fitted with the Weibull function. The release data of 20kD CE dialysis tube was fitted with a linear function. As shown in **Figure 4.S2**, a good fitting was achieved for each dialysis membrane.

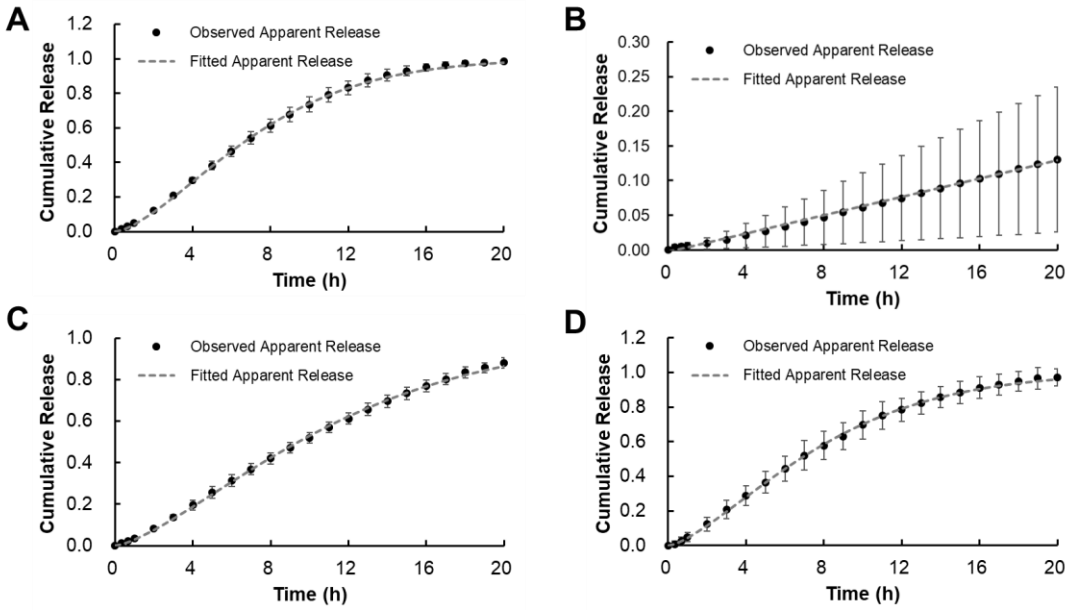

Figure 4.S2 Data fitting of the apparent release data of DOXIL® from 20kD RC (A, r^2 = 0.960), 20kD CE (B, r^2 = 0.997), 50kD CE (C, r^2 = 0.915), and 300kD CE (D, r^2 = 0.938) dialysis devices.

Chapter 5 Product Characterization and Development of *In Vitro* Drug Release Test Method of Exparel Bupivacaine Multivesicular Liposomes

5.1 Abstract

Exparel is a bupivacaine multivesicular liposomes (MVLs) formulation developed based on the DepoFoam technology. The complex composition and the unique structure of MVLs pose challenges to the development and assessment of generic versions. In the present work, we developed a panel of analytical methods to characterize Exparel in particle size, drug and lipid contents, residual solvents, and pH. We further developed an *in vitro* drug release assay for formulation comparison and quality control purposes by optimizing the experimental setup, dilution factors, and release media. The batch-to-batch variability of Exparel was examined by the established analytical methods. Four different batches of Exparel showed good batch-to-batch consistency in particle size, pH, and *in vitro* drug release kinetics. Variance in lipid and drug contents was found across different batches, suggesting possible product variability of Exparel. These analytical methods could benefit the development of generic products by facilitating the *in vitro* equivalency evaluation between generic products and the reference listed drug (RLD).

5.2 Introduction

Exparel is a liposomal bupivacaine formulation, which can locally release bupivacaine over an extended period of 48-72 h [199-201]. Exparel was first approved by FDA in 2011 for single infiltration to provide postsurgical local analgesia. In 2018, Exparel was approved with an additional indication for interscalene brachial plexus nerve block to provide postsurgical regional analgesia [200]. Due to the growing demand for non-opioid postoperative analgesics, the sales of Exparel have been increasing, with full-year sales reaching $413.3 million in 2020 [202]. As key patents of Exparel either have expired or will expire in near future [203-206], Exparel is expected to be an appealing target for generic developers.

Exparel is developed based on DepoFoam technology, where bupivacaine is encapsulated in micron-sized multivesicular liposomes (MVLs) [207]. Unlike traditional unilamellar and multilamellar liposomes with a single aqueous chamber, MVLs present a honeycomb-like structure, with numerous non-centric aqueous chambers separated by a network of lipid membranes [207, 208]. The unique structure of MVLs results in a high aqueous-volume-to-lipid ratio and a high drug encapsulation capacity. In addition to Exparel, DepoFoam technology is also utilized in two other approved but currently discontinued products, DepoCyt (cytarabine liposome injection) and DepoDur (morphine sulfate extended-release liposome injection) [208, 209].

Exparel MVLs are manufactured by a double-emulsion process [210]. First, bupivacaine free base and lipids dissolved in organic solvent are mixed with the first aqueous phase containing phosphoric acid to form water-in-oil (w/o) primary emulsion, where ionized bupivacaine is encapsulated in the inner aqueous phase. The w/o

emulsion is then mixed with the secondary aqueous phase to form a water-in-oil-in-water (w/o/w) emulsion. The organic solvent is removed through evaporation, which results in formation of solidified microparticles. The microparticles are subsequently subject to tangential flow filtration to remove the unencapsulated drug and lipids, exchange the aqueous dispersion media to 0.9% saline, and adjust the drug concentration. The resulting MVLs present complex particle structures with a number of critical quality attributes that potentially can impact the quality and performance of the final product. Some known particle attributes affecting the drug encapsulation and release behavior of Exparel MVLs include particle size, inner structures, pH, and osmolarity of the inner water phase [211, 212]. The complex compositions, manufacturing process, and complicated particle structure of Exparel bupivacaine MVLs pose challenges for generic development and assessment.

In 2018, the FDA issued a product-specific draft guidance for liposomal bupivacaine [113]. According to the draft guidance, generic bupivacaine liposomes should present equivalent product characteristics to the reference product, including free and encapsulated drug content, lipid content, particle morphology and structures, internal aqueous environment, as well as the *in vitro* drug release kinetics [113]. Such evaluations necessitate the analytical methods for formulation characterization of bupivacaine MVLs. Particularly, there has been no compendial *in vitro* release test (IVRT) method of MVLs. Previously reported *in vitro* drug release methods for MVLs usually take several days to weeks, making them unsuitable for a quick determination of *in vitro* drug release profiles [213, 214]. Recently, Manna et al. developed a novel IVRT method for bupivacaine MVLs by modified USP-2 with a reverse-dialysis setup [215].

This method proved extremely valuable to investigate the drug release mechanisms of MVLs, but the relatively long release period (48 – 72 h for >80% drug release) and the need for *in-situ* fiber optic probes may pose challenges for some generic developers. In addition to the unmet demand for IVRT methods, there is a lack of information on the batch-to-batch variability of Exparel.

To address the above problems, we developed a series of analytical methods to characterize Exparel in terms of particle size distribution, drug and lipids contents, formulation pH, and residue solvents. 4 different lots of Exparel RLD were analyzed, and the lot-to-lot variability was analyzed. We further developed an accelerated IVRT method for quality control and comparison purposes by optimizing the experimental setups and release parameters. The methods developed in the present study would be valuable for developing generic bupivacaine MVLs and other MVLs-based products.

5.3 Materials and Method

5.3.1 Materials

Four batches of bupivacaine liposome injectable suspension, Exparel, with batch numbers 17-3110, 17-4046, 17-4161, and 17-4216, were purchased from the Research Pharmacy of the University of Michigan Health System. Another batch of Exparel, 21-P080, was later purchased from the same source for imaging studies described in **5.3.3**. 1,2-dipalmitoyl-sn-glycero-3-phosphoglycerol sodium salt (DPPG-Na) and 1,2-dierucoyl-sn-glycero-3-phosphocholine (DEPC) were purchased from NOF. Tricaprylin was purchased from Sigma. US Pharmacopeia (USP) grade bupivacaine hydrochloride hydrate was purchased from Fisher Scientific. Ropivacaine hydrochloride hydrate was purchased from Cayman Chemical.

5.3.2 Particle size distribution

The particle size distribution was determined using Malvern Mastersizer 2000 (Malvern Instruments Ltd., Worcestershire, UK). Undiluted Exparel MVLs were added to 0.9% saline in a dispersion unit under 850 rpm stirring until the obscuration limit (10%) was reached. Three measurements were conducted for each sample.

5.3.3 Inner structure of Exparel MVLs

The inner structure of Exparel MVLs was observed using cryogenic-scanning electron microscopy (cryo-SEM) and confocal microscopy as described previously [215]. Briefly, for cryo-SEM observation, diluted Exparel MVLs were sandwiched between two freezer hats and fast-frozen in liquid ethane. The frozen samples were then fractured on a pre-cooled Leica EM ACE600. After being sputter-coated with 5 nm of gold, the samples were imaged using a pre-cooled TESCAN Mira 3 FE-SEM operated at 5 kV. For confocal microscopy studies, Exparel MVLs were incubated with lipophilic dye BODIPY 500/510 (C4, C9 (5-Butyl-4,4-Difluoro-4-Bora-3a,4a-Diaza-*s*-Indacene-3-Nonanoic Acid), Thermo Fisher Scientific) with a DEPC: BODIPY molar ratio of 1: 0.024 at room temperature for 1 h in dark. Then the samples were diluted with PBS, loaded onto glass slides, and observed by confocal microscopy at 505–515 nm.

5.3.4 Quantification of bupivacaine

The bupivacaine content was quantified using ultra performance liquid chromatography (UPLC) by Waters ACQUITY UPLC-H Class System with UV detection at 265 nm. For total bupivacaine content quantification, 1 volume of the formulation was first diluted with 3 volumes of water, followed by a further dilution to 40 volumes using

methanol supplemented with 0.1% formic acid (FA). The samples were further diluted with mixture of acetonitrile and methanol (V:V = 2:1) with 0.1% FA to 400 volumes. To isolate unencapsulated bupivacaine, the formulation was firstly centrifuged at 400 rcf for 10 min to remove intact MVLs. The supernatant was then transferred to Amicon Ultra-0.5 mL centrifugal tubes with a 30 kD molecular weight cut-off (MWCO) and centrifuged at 1500 rcf for 15 min. The filtrate containing free bupivacaine was diluted 20 times with mixture of acetonitrile and methanol (V:V = 2:1) containing 0.1% FA. Bupivacaine standard solutions were prepared using USP bupivacaine hydrochloride hydrate in the same solvent. 3 μL sample was injected to a Waters ACQUITY UPLC BEH HILIC column (2.1 × 50 mm). The mobile phase consisted of (A) water with 0.1% FA, (B) acetonitrile with 0.1% FA, (C) methanol with 0.1% FA, and (D) 100 mM ammonium formate water solution (solvent D). The flow rate was 0.65 mL/min. The gradient elution procedure is shown in **Table 5.1**.

Table 5.1 Gradient elution procedure for bupivacaine quantification.

Time/min	A%	B%	C%	D%
0	0	90	5	5
2	0	90	5	5
2.8	20	70	5	5
2.81	20	70	5	5

5.3.5 Quantification of lipid components

Cholesterol was quantified by Free Cholesterol Detection Kit (Wako Diagnostics) following instructions from the manufacturer. DEPC, DPPG-Na, and tricaprylin were quantified by ultra-performance liquid chromatography-mass spectrometry (UPLC-MS) using Waters ACQUITY UPLC-H Class System equipped with a QdaTM detector. 1

volume of the formulation was firstly diluted with 3 volumes of water, followed by a further dilution to 8000 volumes using methanol with 0.1% FA. The samples were separated using an ACQUITY UPLC BEH300 C4 column. The mobile phase consisted of (A) water with 0.1% FA, (B) acetonitrile with 0.1% FA, (C) methanol with 0.1% FA, and (D) 100 mM ammonium formate water solution. The flow rate was 0.3 mL/min. The gradient elution procedure is shown in **Table 5.2**. Lipids were detected at M/z of 899.00 (+) for DEPC, 721.79 (-) for DPPG-Na, and 488.50 (+) for tricaprylin, respectively.

Table 5.2. Gradient elution procedure for lipids quantification.

Time/min	A%	B%	C%	D%
0	50	30	15	5
1	5	60	30	5
4	5	60	30	5
4.5	50	30	15	5

5.3.6 Residual solvent measurement

Residual solvents in the formulation were identified and quantified by gas chromatography (GC) on a Trace 1310 gas chromatograph (Thermo Fisher Scientific Inc., USA). Nitrogen was used as the carrier gas with a flow rate of 25 mL/min. Airflow was 350 mL/min, and hydrogen flow was 35 mL/min. The front detector was 240 ºC, and the front inlet pressure was a constant flow of 2 mL/min. For quantification, 0.2 mL of formulation was added to 0.8 mL DMSO in the GC headspace vials, and the caps were immediately sealed. Each sample was agitated for 20 min at 80 ºC. Then 1 mL of headspace sample was injected into the front inlet with a temperature of 140 ºC, split flow of 40 mL/min, and split ratio of 20. The initial GC column temperature was set to 40 °C for 15 min, followed by an increase to 240 °C at 10 °C /min over 20 min and holding

at 240 °C for 2 min. Standard samples were prepared by dissolving individual organic solvents in 0.9% saline:DMSO = 1:4 (V:V).

5.3.7 pH of internal and external aqueous phase of MVLs

The pH of both internal and external aqueous environment was measured by 430 pH Meter (Corning, USA) with MI-410 microelectrodes (Microelectrodes Inc., USA). To rupture MVLs and release the inner water phase, 1 mL formulation was subject to probe sonication (3W, room temperature) for 2 min and 6 min, followed by pH measurement.

5.3.8 In vitro drug release test (IVRT)

5.3.8.1 Selection of IVRT methods

Three experimental setups, which are respectively facilitated by a rotator, a shaker, or mesh tubes, were tested to develop the *in vitro* drug release assay (**Figure 5.1**). For the rotator-facilitated method, Exaprel formulation was diluted by 50 times using PBS (pH 7.4) containing 0.02% NaN_3. 1.8 mL diluted formulation was put in each 2 mL round-bottom Eppendorf tube. The tubes were fixed on a vertical rotator with a speed of 15 rpm and were incubated at 37 ºC. At the predetermined time points, three tubes were taken for further analysis.

For the shaker-facilitated method, Exaprel formulation was diluted by 50 times using PBS (pH 7.4) containing 0.02% NaN_3. 1.8 mL diluted formulation was put in each mL round-bottom Eppendorf tube. The tubes were put on a horizontal shaker with a speed of 80 rpm incubated at 37 ºC. At the predetermined time points, three tubes were taken for further analysis.

For the mesh-tube facilitated method, 5 mL formulation was put into a nylon monofilament mesh tube with 1 µm membrane pore size (size 1×6 inch, Midwest, LLC, SKU NMO1SBF). The mesh tube was then inserted into a 500 mL glass bottle filled with 245 mL PBS (pH 7.4) containing 0.02% NaN_3. The depth of the tube immersed in the media was adjusted so that the liquid volume inside the mesh tube remained 5 mL to avoid extra dilution of the formulation. The release bottle was put in an incubating shaker at a shaking speed of 80 rpm at 37 °C. At the predetermined time points, 0.5 mL release media was removed outside the bag, and another 0.5 mL fresh blank media was added back.

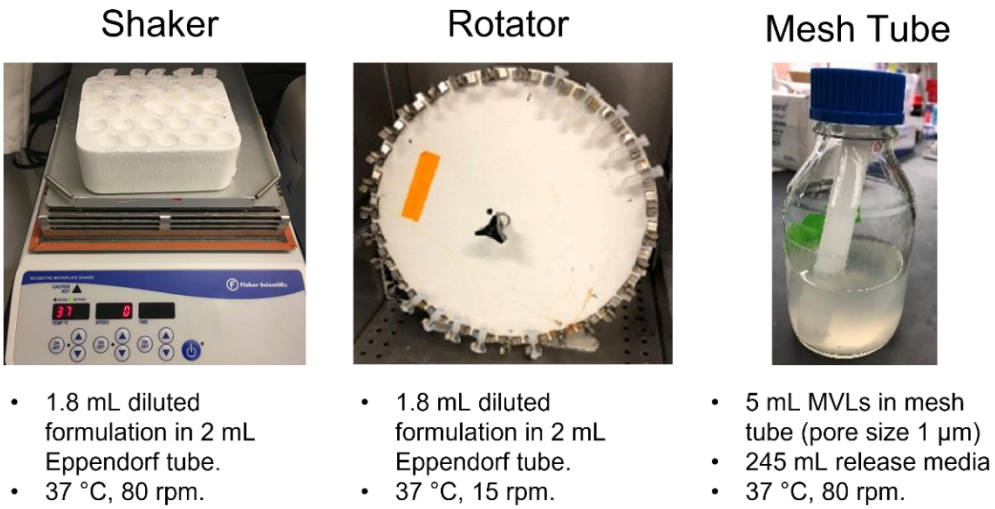

Figure 5.1 Different experimental setups for *in vitro* drug release assays.

The size distribution of MVLs during the release process was analyzed by MasterSizer as described in **5.3.2**. The morphology of the particles was visualized by a microscope. To quantify the released bupivacaine, the samples were centrifuged for 600 g to remove liposome particles. Then 200 µL supernatant was taken and mixed with 50 µL ropivacaine solution (500 µg/mL in PBS with 0.02% NaN_3, pH = 6), which served as an internal standard. The mixture was diluted with 250 µL methanol, followed by

vigorous vortexing. Then 500 µL acetonitrile was added, followed by vigorous vortexing. The final mixture was centrifuged at 10000 rpm for 10 min at room temperature to remove aggregates. The supernatant was injected into Waters ACQUITY UPLC H-Class System equipped with a Waters ACQUITY UPLC BEH C18 column (2.1 × 50 mm). The mobile phase was composed of 70% (A) water with 0.1% FA; 15% (B) acetonitrile with 0.1% FA; and 15% (C) methanol with 0.1% FA. The flow rate was 0.4 mL/min. The UV detection wavelength was 220 nm.

5.3.8.2 In vitro drug release kinetics of intact and compromised Exparel® products

The optimized rotator-based, sample-and-separate IVRT method was selected to assess the *in vitro* drug release from Exparel MVLs. Briefly, Exparel MVLs formulation was diluted 50 times with PBS (pH 7.4) containing 0.02% NaN_3. 1.8 mL of the diluted formulation was put in each 2 mL round bottom Eppendorf tube. The tubes were fixed on a vertical rotator with a speed of 15 rpm at 37 ºC. At the predetermined time points, three tubes were taken out. The released bupivacaine content was quantified as described above. To test the discriminative capacity of the IVRT method, compromised Exparel samples were prepared by being subject to 20 s vortexing or 1 freeze-thaw cycle. The *in vitro* drug release profiles of compromised formulations were determined and compared with intact Exparel formulation. For batch-to-batch comparison, the *in vitro* drug release profiles of 4 batches of Exparel products were determined using the method described above. The release profiles were compared using f2 similarity test with the following equation:

$$f2 = 50\ \log\left[\frac{100}{\sqrt{1 + \frac{\sum_{i=1}^{n}(R_t - T_t)^2}{n}}}\right]$$

where *n* is the number of time points, R_t and T_t are the cumulative release value of the reference and test formulation at time *t*, respectively. A test formulation with a similarity factor *f2* > 50 is considered similar to the reference formulation.

5.4 Results

5.4.1 Particle size distribution

The particle size distribution of four batches of Exparel MVLs was measured by laser diffraction. As shown in **Figure 5.2** and **Table 5.3**, Exparel MVLs have a narrow particle size distribution with a median volume particle diameter (d0.5) around 26 μm, which is consistent with the reported median particle size of 24 to 31 μm [200]. Particles from four batches of products showed almost identical particle size distribution profiles, with no significant statistical difference (One-way ANOVA, p > 0.05).

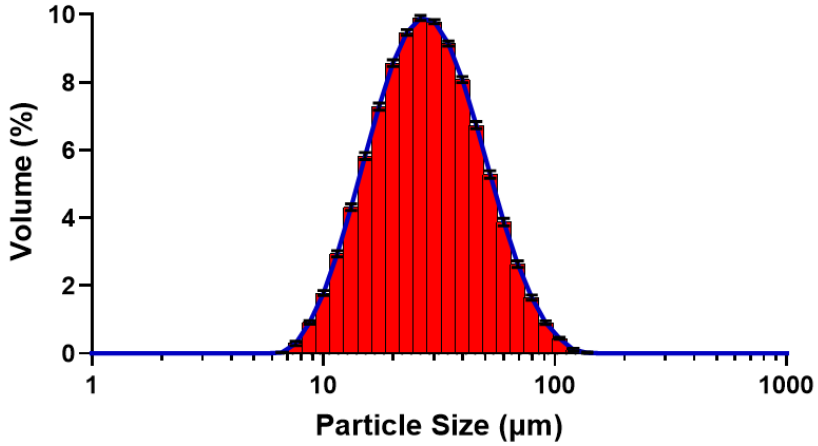

Figure 5.2 Particle size distribution of Exparel bupivacaine multivesicular liposomes. Data are presented as mean ± SD of four batches of product each measured 3 times

Table 5.3 Size distribution of four batches of Exparel formulation measured by laser diffraction. Data are presented as mean ± SD (n = 3).

Lot No.	d0.1 (μm)	d0.5 (μm)	d0.9 (μm)
17-3110	13.12 ± 0.13	26.07 ± 0.19	52.64 ± 0.17
17-4046	13.08 ± 0.10	25.73 ± 0.17	51.47 ± 0.29
17-4161	13.02 ± 0.19	25.62 ± 0.31	51.46 ± 0.54
17-4216	12.99 ± 0.16	25.60 ± 0.25	51.37 ± 0.47

5.4.2 Inner structure of Exparel MLVs

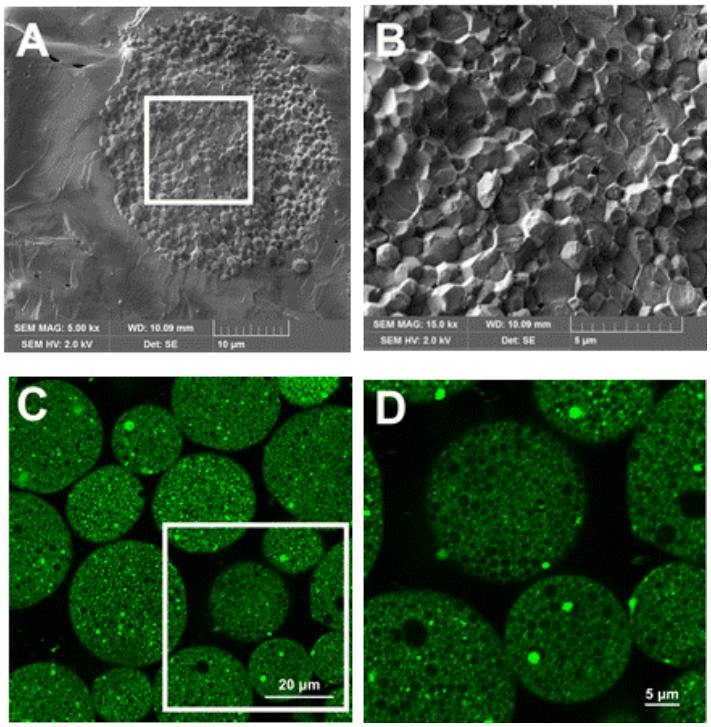

Figure 5.3 Representative cryo-SEM (A, B) and confocal fluorescent microscopy images (C, D) showing inner structure of Exparel MVLs.

The non-centric aqueous compartments within Exparel MLVs were imaged by cryo-SEM and confocal microscope (**Figure 5.3**), respectively. Cryo-SEM images showed a close packing of the internal chambers with polyhedral structures. The diameters of inner structure are within a range of 1-2 μm, which is consistent to previous reports [215, 216]. As a less-disruptive method, confocal microscopy was used to visualize the fluorescently labeled lipid layers within MVLs in aqueous environment.

Similar to SEM images, confocal microscopy images showed spherical inner compartments within MVLs. Lipid droplets formed by tricaprylin were also observed as dense green dots within MVLs.

5.4.3 Drug and lipids contents

The total and unencapsulated bupivacaine, as well as the lipid contents, of four batches of Exparel were quantified using UPLC. To isolate the unencapsulated bupivacaine, a two-step isolation method was established. First, MVLs and supernatant consisting of the unencapsulated drug were separated by centrifugation at 400 rcf centrifuge force. For reference, 600 rcf is the commonly used centrifugation force for particle isolation and purification of drug-loading MVLs [217, 218]. No difference in particle size distribution was observed before and after centrifugation, suggesting the centrifuge process did not disrupt the particle structure (data not shown). The supernatant was subsequently subject to ultracentrifugation to further isolate unencapsulated bupivacaine from possible lipid nanoparticles. As shown in **Table 5.4**, the total bupivacaine contents were consistent with the labeled drug content except for batch 17-4046, which is lower than the labeled value. The free drug percentages ranged from 4 to 8%. Variance in lipid contents was found among four batches of Exparel products (**Table 5.5**). It is also worth noting that the ratio of different lipid species also varies among different batches, as one lipid component might be slightly higher than the labeled value while another one was slightly lower.

Table 5.4 Total bupivacaine and unencapsulated bupivacaine contents in four batches of Exparel formulation. All values are presented as mean ± SD (n=3).

Lot No.	Total bupivacaine (mg/mL)	Free bupivacaine (mg/mL)	Free bupivacaine fraction (%)
Published Values	13.3	-	-
17-3110	13.67 ± 0.62	0.54 ± 0.05	4.1 ± 0.4
17-4046	12.43 ± 0.28	0.73± 0.06	5.5 ± 0.4
17-4161	13.23 ± 0.11	1.09 ± 0.01	8.2 ± 0.1
17-4216	13.10 ± 0.32	0.62 ± 0.03	4.6 ± 0.3

Table 5.5 Lipid contents in four batches of Exparel formulation. All values are presented as Mean ± SD (n=3).

Lot No.	DEPC (mg/mL)	DPPG (mg/mL)	Tricaprylin (mg/mL)	Cholesterol (mg/mL)
Published Values	8.2	0.9	2.0	4.7
17-3110	8.17 ± 0.26	0.82 ± 0.02	2.19 ± 0.20	4.54 ± 0.07
17-4046	7.19 ± 0.36	0.73 ± 0.04	1.92 ± 0.08	4.04 ± 0.02
17-4161	7.68 ± 0.33	0.92 ± 0.07	1.75 ± 0.09	4.42 ± 0.02
17-4216	7.81 ± 0.21	0.78 ± 0.07	2.12 ± 0.12	4.26 ± 0.06

5.4.4 Residual organic solvents

Different manufacturing methods have been described in various patents concerning Exparel. In earlier patents, it was described that in the first emulsification step, bupivacaine salt is dissolved in the first aqueous solution, and chloroform is used as the organic solvent [203, 219]. However, the manufacturing process was later modified, where methylene chloride is used to dissolve lipids and bupivacaine free base in the first emulsification process [220]. To identify the species and level of residual organic solvents in commercial Exparel product, the formulation was tested by GC along with standard samples of three commonly used organic solvents, including chloroform, methylene chloride, and diethyl ether. As seen in **Table 5.6**, only methylene chloride was detected in the samples, which is consistent with the organic solvent

disclosed in the latest patents. The methylene chloride contents of four batches of Exparel are well below the limit of 600 ppm set by ICH guideline Q3C (R8).

Table 5.6 Residual organic solvents quantified in four batches of Exparel formulation. All values are presented as Mean ± SD (n=3).

Lot No.	Methylene Chloride (ppm)	Chloroform (ppm)	Diethyl Ether
17-3110	62.2 ± 5.9	Not detected	Not detected
17-4046	73.5 ± 4.5	Not detected	Not detected
17-4161	135.6 ± 3.6	Not detected	Not detected
17-4216	65.5 ± 4.6	Not detected	Not detected

5.4.5 pH of internal and external aqueous phases

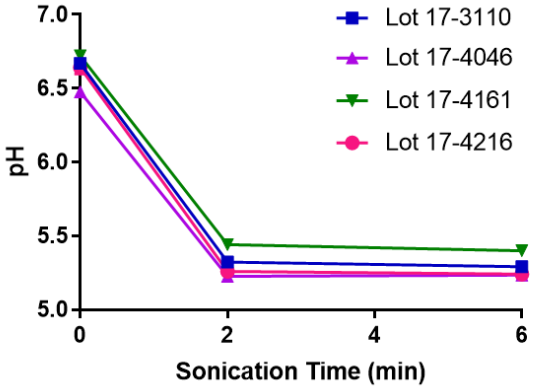

Figure 5.4 Formulation pH of four batches of Exparel before and after probe sonication. All values are presented as Mean ± SD (n=3).

Exparel MVLs have distinct external and inner water phases. As a weak basic drug, bupivacaine is mostly ionized in the acidic inner aqueous chambers, which reduces its diffusion through lipid membranes. To facilitate drug encapsulation and sustained release of bupivacaine, the external aqueous phase of Exparel MVLs is 0.9% saline with a reported pH of 5.8-7.4, while the inner aqueous phase is more acidic [200, 203, 205]. To investigate the pH of the external and inner aqueous phase of Exparel

MVLs, the formulation pH before and after particle rupture was measured. As shown in **Figure 5.4**, prior to probe sonication, all four batches of Exparel had a pH of 6.5-7, which agreed with the reported pH of 5.8-7.4 in the package insert. A drastic pH drop was observed after probe sonication, which corresponds to the release of the acidic inner aqueous phase upon particle rupture.

5.4.6 In vitro drug release assay

5.4.6.1 Experimental setups

As shown in **Figure 5.5** and **5.6**, The release assay performed on a horizontal shaker resulted in limited drug release and little change in particle size. In comparison, the rotator-facilitated method resulted in a rapid drug release within 24 h accompanied by a steady decrease of particle sizes. Such results are consistent with the previous study of Manna *et al.*, where increased mechanical stress was found to increase the drug release rate through surface erosion [215]. Interestingly, minimal drug release and particle size change were observed in the mesh-tube-facilitated method. With the

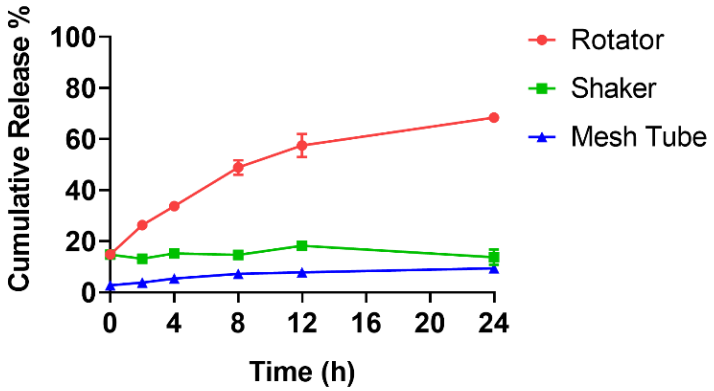

Figure 5.5 *In vitro* drug release profile of Exparel determined by different experimental setups. All values are presented as Mean ± SD (n=3).

relatively rapid drug release, the rotator-facilitated method is selected for further optimizations.

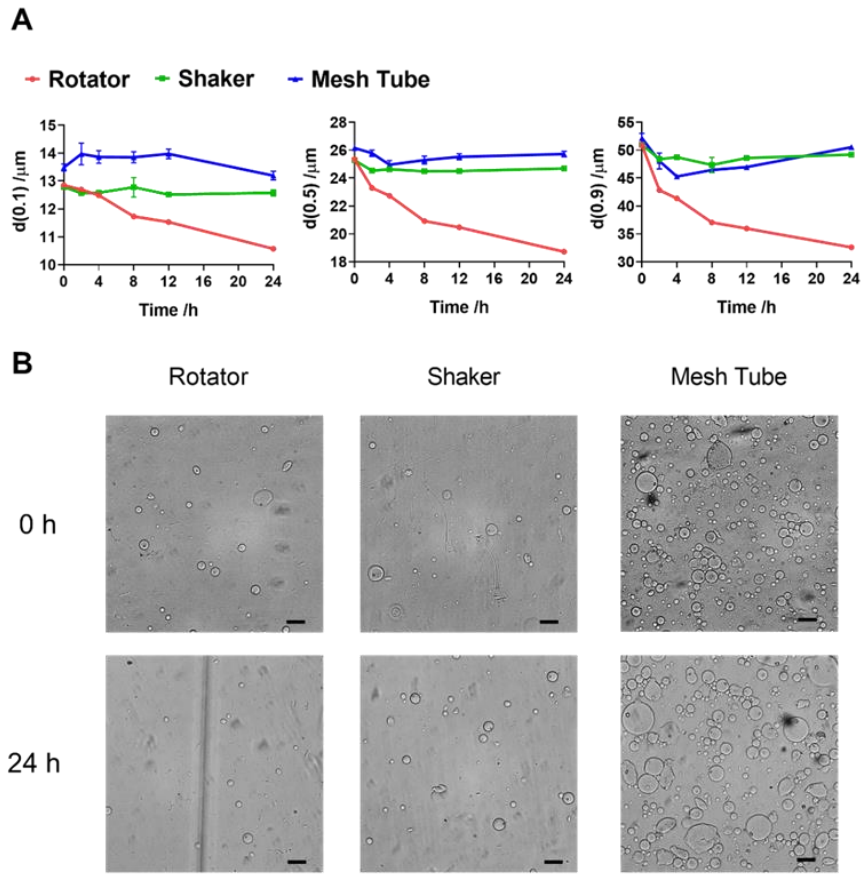

***Figure 5.6*.** Particle size distribution (A) and morphology (B) of Exparel liposomes before and after different drug release assays. Scale bar represents 50 μm. All values are presented as Mean ± SD (n=3).

5.4.6.2 Effects of formulation dilution and release media

As shown in **Figure 5.7** and **Figure 5.8**, more diluted formulations presented quicker drug release and a more significant decrease in particle size. On the other hand, less diluted formulation aggregated during the release process, possibly explaining the slower drug release. In terms of the effects of release media pH on drug

release kinetics, as shown in **Figure 5.9 and Figure 5.10**, drug release was accelerated at lower pH. Meanwhile, drug release was slowed when supplementing BSA to the release media. Reduction of particle size was observed in PBS groups, but supplementing BSA abolished such changes.

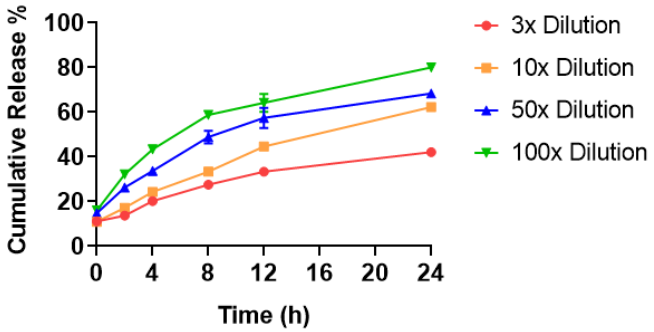

Figure 5.7 *In vitro* drug release profile of Exparel determined by the rotator method with different dilution factors. All values are presented as Mean ± SD (n=3).

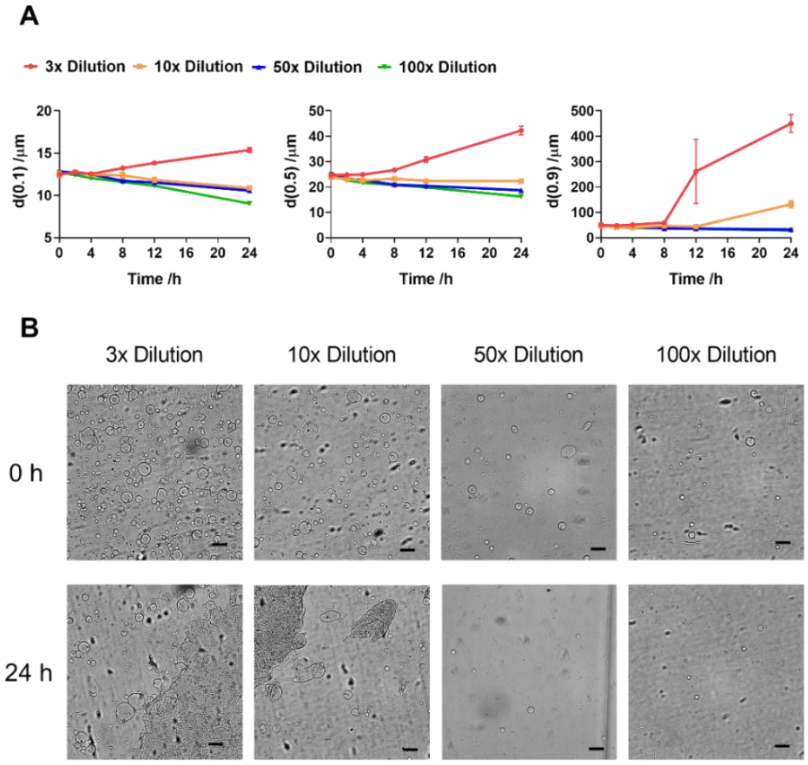

Figure 5.8 Particle size distribution (A) and morphology (B) of Exparel liposomes before and after drug release assays with different dilutions. Scale bar represents 50 µm. All values are presented as Mean ± SD (n=3).

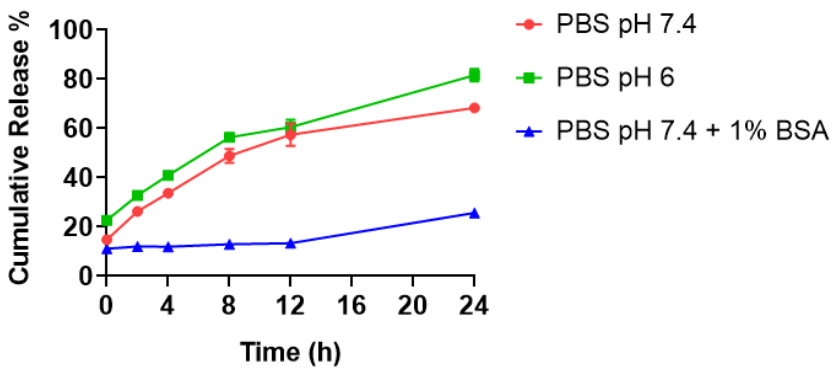

Figure 5.9 *In vitro* drug release profile of Exparel determined by the rotator method with different release media. All values are presented as Mean ± SD (n=3).

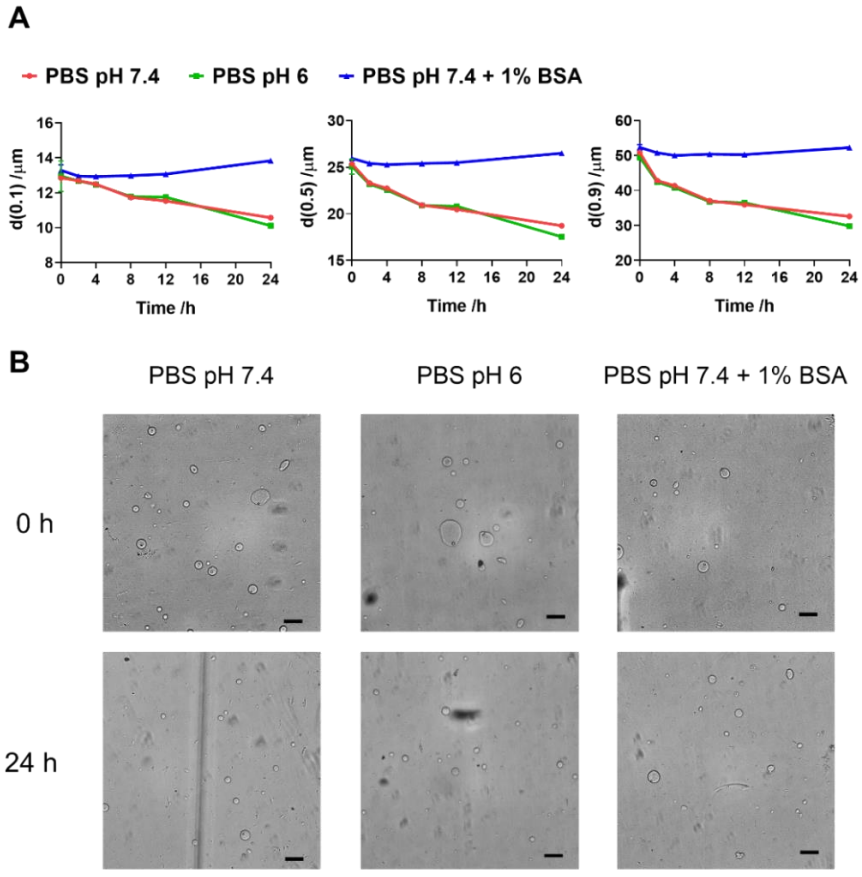

Figure 5.10 Particle size distribution (A) and morphology change (B) of Exparel liposomes during release experiment with different release media. Scale bar represents 50 µm. All values are presented as Mean ± SD (n=3).

5.4.6.3 In vitro drug release kinetics intact and compromised Exparel products

The rotator-facilitated method, with 50x dilution and PBS (pH 7.4) as the release media, was chosen as the optimized IVRT method. The discriminative ability of the optimized IVRT was further tested by comparing *in vitro* drug release kinetics of intact and compromised Exparel samples. As shown in **Figure 5.11**, mechanical agitated Exparel MVLs showed a faster drug release, while the freeze-thaw formulation completely lost the sustained-release function.

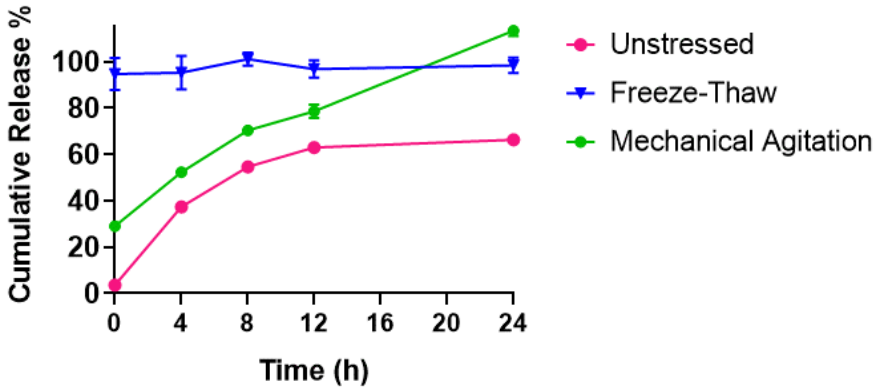

Figure 5.11 *In vitro* drug release profile of intact and compromised Exparel MVLs. All values are presented as Mean ± SD (n=3).

The batch-to-batch comparison of Exparel was conducted using the optimized IVRT. As shown in **Figure 5.12**, four batches of Exparel showed similar drug release profiles. The results of the f2 release similarity comparison were all above 50%, suggesting no statistical difference in release profiles across different batches.

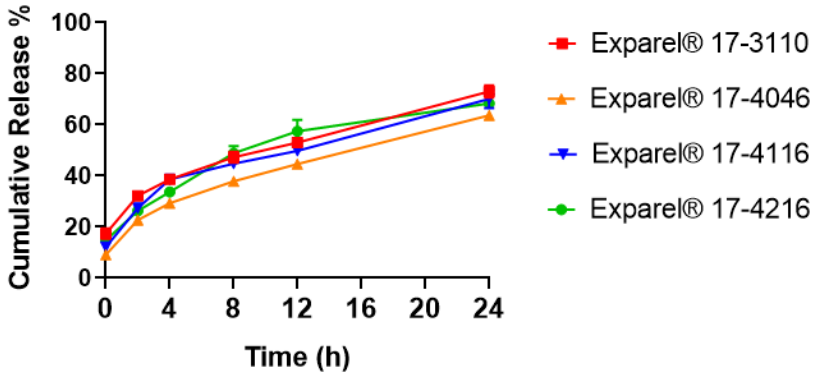

Figure 5.12 *In vitro* drug release profile of four different Exparel batches. All values are presented as Mean ± SD (n=3).

5.5 Discussion

In the present study, analytical methods were developed to quantify the particle size distribution, drug and lipids contents, formulation pH, residual solvents, and *in vitro* drug release of Exparel bupivacaine MVLs. Four different batches of Exparel product showed good batch-to-batch consistency in particle size, pH, and *in vitro* drug release kinetics. At the same time, variance in lipid and drug contents was found across different batches. Moreover, there was a noticeable difference in the ratio of lipid components across different batches, implying potential variability in lipid recoveries during the manufacturing process. While we acknowledge that the results were obtained from limited samples and the quantification method was not rigorously validated under GLP requirements, it is worth noting that there could be some batch-to-batch variability of Exparel based on the current results. This observation supports the need for testing multiple batches of the reference product, when possible. The inherent product variability can pose a significant challenge for generic drug developers working on complex injectable products. In a recent industry survey presented in GDUFA Science

and Research Initiatives Public Workshop, 10 out of 18 respondents voiced concerns related to highly variable and old reference products [221]. Some highlighted issues include “reference listed drugs do not pass *in vitro* comparability when compared to itself”, and “discrepancies between label and actual product” [221]. The survey results, which resonated our findings on batch-to-batch variability of Exparel, suggested the need for further research to address challenges in demonstrating equivalence to reference products with possible high inherent variability.

MVLs are characterized by a honeycomb-like structure where the inner aqueous phase is separated into multiple non-centric chambers. According to the FDA draft product specific guidance on bupivacaine MVLs, generic bupivacaine MVLs are recommended to present similar inner chamber morphology compared to the reference product. In the present study, cryo-SEM and confocal microscopy are used to characterize the inner structure of Exparel MVLs with different emphases. Cryo-SEM revealed the polyhedral structure of inner chambers packed in a similar way to gas-liquid foams, which is consistent with previous topology studies [222]. In terms of the distribution of lipid components in MVLs, a previous ^{13}C nuclear magnetic resonance (NMR) study has suggested that the inner chambers were separated by phospholipid bilayers, while triglyceride mainly resides at bilayer intersection spaces or forms droplets dispersed in MVLs [223]. Both the lipid membrane separation and tricaprylin oil droplets were observed using confocal microscopy with the lipophilic BODIPY dye in the present study. Cryo-SEM and confocal microscopy would be valuable tools to determine the similarity of inner structures between generic candidates and the reference product.

The complex sustained-release mechanisms of Exparel and other MVLs have not been fully revealed. Various mechanisms have been suggested to be involved, including drug permeation through lipid membranes, lipid rearrangement, and particle erosion [208, 209, 224]. In a recent study by Manna *et al.*, using a reverse dialysis method adapted with the USP-2 apparatus, a tri-phasic release profile of bupivacaine from MVLs was observed [215]. The first stage is an initial burst release stage, possibly caused by unencapsulated or surface-bound bupivacaine. The initial burst release is followed by a lag phase where the drug slowly diffuses through lipid membranes, possibly accompanied by lipid rearrangement. The MVLs subsequently undergo a secondary release phase, mainly attributed to particle erosion [215].

In the present study, we intended to design an accelerated and discriminatory IVRT method for assessing potential physicochemical differences in product formulation. Instead, we intended to design a quick and discriminatory IVRT method that can achieve ~80% release within 24 h for quality control and comparison purposes. Mechanical stress was found to be the main driving force for accelerated drug release from MVLs. In the shaker-facilitated method and mesh-bag-facilitated method, insufficient mixing and limited mechanical stress led to minimal drug release within 24 h. On the contrary, vertical rotation resulted in an accelerated drug release. A significant reduction in particle size was observed only during the rotator-facilitated, suggesting particle erosion is the main mechanism driving the accelerated drug release. Such observation is consistent with the earlier study by Manna et al. [215]. The impacts of sample dilution, release media pH, and BSA supplementation were further determined. More diluted samples presented faster drug release in the rotator-based assay,

whereas insufficient dilution led to slow drug release with significant particle aggregation. Acidic release media accelerated drug release, which can be explained by increased sink condition as bupivacaine is more ionized thus more water-soluble in acidic pH. Supplementing BSA to release media led to slow drug release with minimal change in particle size. Such results were surprising, as BSA was expected to increase drug release by disrupting liposome membranes and binding released bupivacaine molecules [225]. One possible explanation is that BSA increased the viscosity of release media, which altered the mechanical stress on liposomal particles.

A rotator-based IVRT method with release media of PBS pH 7.4 was selected to evaluate the *in vitro* release kinetics of Exparel. The discriminatory ability of the established IVRT was tested by comparing release profiles of the intact formulation and formulation compromised by mechanical stress and freeze-thaw. As shown in **Figure 5.11**, mechanical agitation greatly increased the free-drug content and drug release rate from bupivacaine liposomes. Freeze-thaw cycle completely abolished the sustained release of the drug, indicating complete destruction of liposome structures during freeze-thaw. The sensitivity of Exparel MVLs to mechanical force indicates that well-controlled transportation and storage conditions are of vital importance to assure the quality of Exparel MVLs during the supply chain.

The present study has several limitations. With the observed batch-to-batch variability, the number of batches of Exparel analyzed in the study was considered limited. The rotator-based IVRT method relied on mechanical stress to accelerate drug release from MVLs, which does not represent physiological conditions. Thus, while this IVRT method may be used for quality control or comparison purposes as part of the

totality evidence approach, other assay setups which more closely mimic physiological conditions would be more desirable when developing *in vitro-in vivo* correlations to predict *in vivo* behavior of bupivacaine MVLs.

5.6 Conclusion

A series of analytical methods were developed to analyze various key quality attributes of liposomal bupivacaine formulation Exparel including particle size distribution, drug and lipids contents, formulation pH, and residual solvents. An accelerated *in vitro* drug release assay was developed. Exparel MVLs presented a median volume particle diameter (d0.5) around 26 μm, with a honeycomb-like inner structure which could be observed by confocal microscopy and cryo-SEM. Methylene chloride was identified as a residual solvent. A good consistency in particle size, pH, and *in vitro* drug release kinetics was found in four batches of Exparel product. Differences in lipid and drug contents was observed across different batches, suggesting possible batch-to-batch variability of Exparel.

Chapter 6 Conclusion and Perspectives

The recent advances in the understanding of the physiological functions of HDLs have led to a paradigm shift for sHDL therapies from focusing on elevating HDL cholesterol levels to enhancing sHDLs functionalities. The first section of the thesis, consisting of Chapters 2 and 3, focuses on optimizing sHDL components to achieve superior endothelial protective and anti-inflammatory effects. In Chapter 2, an activated endothelium targeted sHDL was developed by conjugating VCAM-1 specific peptide ligand. The active targeting sHDLs showed enhanced binding on activated endothelium, inhibited inflammatory responses, and reduced leukocyte adhesion on inflamed endothelium. Based on the results of this proof-of-concept study, VHPK-sHDLs hold the potential to be further optimized to fully exert therapeutic potential to inflammatory disease either as a stand-alone therapy or drug delivery carrier.

In Chapter 3, a bioactive phospholipid, phosphatidylserine (PS), was introduced to sHDL nanoparticles. Incorporating PS into sHDLs improved the particle stability and anti-inflammatory effects on LPS-activated macrophages without impairing the cholesterol efflux capacity and pharmacokinetic profiles of sHDLs. With enhanced anti-inflammatory effects, PS-containing sHDLs may be promising therapeutic agents in suppressing overactive immune responses involved in varieties of diseases such as sepsis, autoimmune diseases, and COVID-19-associated hyperinflammatory syndrome, which will be investigated in future studies. Overall, the knowledge provided in Chapters

2 and 3 increased the understanding of the structure-function relationship of sHDLs, which we hope would facilitate the further optimization of sHDL functionalities for expanded therapeutic applications of sHDL therapies.

The second section of the thesis, consisting of Chapters 4 and 5, focuses on the analytical characterization of liposomal drug products, with a special focus on developing *in vitro* drug release test (IVRT) methods. Chapter 4 is focused on the dialysis-based method, which is a commonly used IVRT method for liposomal drug carriers. The mass transfer analysis demonstrated that the barrier effects produced by dialysis membranes could delay the appearance of drug molecules in the sampling compartment, leading to underestimated drug release. A two-step approach was proposed to address this problem. First, the barrier effect of the dialysis membrane was determined by a calibration experiment. Then, a mathematical model was applied to find the actual drug release kinetics from the apparent drug release data. The model was tested on Doxil® (doxorubicin liposomes), and a good agreement was found between the experimental data and the predicted value. The proposed model would help the proper interpretation of the data from dialysis studies. Moreover, it enables the methodological evaluation of dialysis-based *in vitro* drug release assays, which will facilitate the development of reliable, reproducible, and discriminatory IVRT methods for liposome and other nanoparticle drug delivery systems.

Chapter 5 focused on characterizing the physicochemical properties of a commercial multivesicular liposomal product, Exparel. The critical quality attributes of Exparel, including particle size, inner structure, drug and lipid contents, residual solvents, and pH, were characterized, and batch-to-batch variability of Exparel was

examined. Moreover, an *in vitro* drug release assay was developed for formulation comparison and quality control for multivesicular liposomes. The data derived from Chapter 5 will provide generic drug developers with valuable information on CQAs of bupivacaine multivesicular liposomes. The next step of the research will involve investigating the relationship between critical process parameters (CPPs), CQAs, and *in vivo* performance, as well as establishing IVIVC for bupivacaine liposomes. Overall, we expect the analytical methods developed in Chapter 4 and Chapter 5 could provide useful information to liposomal product developers as well as regulatory agencies on the analytical characterization of liposomal drug products. Such collaborations with industry and regulatory agencies will be continued in the future to fill the current scientific and regulatory gaps in the development of liposomal drug products.

Bibliography

[1] A. Kontush, M. Lindahl, M. Lhomme, L. Calabresi, M.J. Chapman, W.S. Davidson, Structure of HDL: particle subclasses and molecular components, Handbook of experimental pharmacology, 224 (2015) 3-51.
[2] A. Kontush, M. Lhomme, M.J. Chapman, Unraveling the complexities of the HDL lipidome, Journal of lipid research, 54 (2013) 2950-2963.
[3] E.M. Tsompanidi, M.S. Brinkmeier, E.H. Fotiadou, S.M. Giakoumi, K.E. Kypreos, HDL biogenesis and functions: role of HDL quality and quantity in atherosclerosis, Atherosclerosis, 208 (2010) 3-9.
[4] A.D. Dergunov, V.B. Baserova, Different Pathways of Cellular Cholesterol Efflux, Cell Biochem Biophys, (2022).
[5] E. Favari, A. Chroni, U.J. Tietge, I. Zanotti, J.C. Escola-Gil, F. Bernini, Cholesterol efflux and reverse cholesterol transport, Handbook of experimental pharmacology, 224 (2015) 181-206.
[6] H.J. Pownall, C. Rosales, B.K. Gillard, A.M. Gotto, Jr., High-density lipoproteins, reverse cholesterol transport and atherogenesis, Nature reviews. Cardiology, (2021).
[7] H.C. Prosser, M.K.C. Ng, C.A. Bursill, The role of cholesterol efflux in mechanisms of endothelial protection by HDL, Current opinion in lipidology, 23 (2012) 182-189.
[8] F. Bonacina, A. Pirillo, A.L. Catapano, G.D. Norata, Cholesterol membrane content has a ubiquitous evolutionary function in immune cell activation: the role of HDL, Current opinion in lipidology, 30 (2019) 462-469.
[9] X. Zhu, J.S. Owen, M.D. Wilson, H. Li, G.L. Griffiths, M.J. Thomas, E.M. Hiltbold, M.B. Fessler, J.S. Parks, Macrophage ABCA1 reduces MyD88-dependent Toll-like receptor trafficking to lipid rafts by reduction of lipid raft cholesterol, Journal of lipid research, 51 (2010) 3196-3206.
[10] M. Suzuki, D.K. Pritchard, L. Becker, A.N. Hoofnagle, N. Tanimura, T.K. Bammler, R.P. Beyer, R. Bumgarner, T. Vaisar, M.C. de Beer, F.C. de Beer, K. Miyake, J.F. Oram, J.W. Heinecke, High-density lipoprotein suppresses the type I interferon response, a family of potent antiviral immunoregulators, in macrophages challenged with lipopolysaccharide, Circulation, 122 (2010) 1919-1927.
[11] E.E. Morin, L. Guo, A. Schwendeman, X.A. Li, HDL in sepsis - risk factor and therapeutic approach, Front Pharmacol, 6 (2015) 244.
[12] M.A. Incalza, R. D'Oria, A. Natalicchio, S. Perrini, L. Laviola, F. Giorgino, Oxidative stress and reactive oxygen species in endothelial dysfunction associated with cardiovascular and metabolic diseases, Vascul Pharmacol, 100 (2018) 1-19.
[13] M.C. Vohl, T.A. Neville, R. Kumarathasan, S. Braschi, D.L. Sparks, A novel lecithin-cholesterol acyltransferase antioxidant activity prevents the formation of oxidized lipids during lipoprotein oxidation, Biochemistry, 38 (1999) 5976-5981.

[14] N. Shunmoogam, P. Naidoo, R. Chilton, Paraoxonase (PON)-1: a brief overview on genetics, structure, polymorphisms and clinical relevance, Vasc Health Risk Manag, 14 (2018) 137-143.
[15] A.N. Klimov, K.A. Kozhevnikova, A.A. Kuzmin, A.S. Kuznetsov, E.V. Belova, On the ability of high density lipoproteins to remove phospholipid peroxidation products from erythrocyte membranes, Biochemistry (Mosc), 66 (2001) 300-304.
[16] C.R. White, G. Datta, S. Giordano, High-Density Lipoprotein Regulation of Mitochondrial Function, Adv Exp Med Biol, 982 (2017) 407-429.
[17] F. Robbesyn, V. Garcia, N. Auge, O. Vieira, M.F. Frisach, R. Salvayre, A. Negre-Salvayre, HDL counterbalance the proinflammatory effect of oxidized LDL by inhibiting intracellular reactive oxygen species rise, proteasome activation, and subsequent NF-kappaB activation in smooth muscle cells, FASEB J, 17 (2003) 743-745.
[18] U. Forstermann, H.G. Li, Therapeutic effect of enhancing endothelial nitric oxide synthase (eNOS) expression and preventing eNOS uncoupling, British journal of pharmacology, 164 (2011) 213-223.
[19] A. Uittenbogaard, P.W. Shaul, I.S. Yuhanna, A. Blair, E.J. Smart, High density lipoprotein prevents oxidized low density lipoprotein-induced inhibition of endothelial nitric-oxide synthase localization and activation in caveolae, Journal of Biological Chemistry, 275 (2000) 11278-11283.
[20] C. Mineo, I.S. Yuhanna, M.J. Quon, P.W. Shaul, High density lipoprotein-induced endothelial nitric-oxide synthase activation is mediated by Akt and MAP kinases, Journal of Biological Chemistry, 278 (2003) 9142-9149.
[21] T. Kimura, H. Tomura, C. Mogi, A. Kuwabara, A. Damirin, T. Ishizuka, A. Sekiguchi, M. Ishiwara, D.S. Im, K. Sato, M. Murakami, F. Okajima, Role of scavenger receptor class B type I and sphingosine 1-phosphate receptors in high density lipoprotein-induced inhibition of adhesion molecule expression in endothelial cells, Journal of Biological Chemistry, 281 (2006) 37457-37467.
[22] J.R. Nofer, B. Levkau, I. Wolinska, R. Junker, M. Fobker, A. von Eckardstein, U. Seedorf, G. Assmann, Suppression of endothelial cell apoptosis by high density lipoproteins (HDL) and HDL-associated lysophingolipids, Journal of Biological Chemistry, 276 (2001) 34480-34485.
[23] J.T.M. Tan, M.K.C. Ng, C.A. Bursill, The role of high-density lipoproteins in the regulation of angiogenesis, Cardiovascular Research, 106 (2015) 184-193.
[24] M.F. Brodde, S.J. Korporaal, G. Herminghaus, M. Fobker, T.J. Van Berkel, U.J. Tietge, H. Robenek, M. Van Eck, B.E. Kehrel, J.R. Nofer, Native high-density lipoproteins inhibit platelet activation via scavenger receptor BI: role of negatively charged phospholipids, Atherosclerosis, 215 (2011) 374-382.
[25] K.C. Vickers, D.L. Michell, HDL-small RNA Export, Transport, and Functional Delivery in Atherosclerosis, Current atherosclerosis reports, 23 (2021) 38.
[26] B.L. Sanchez-Gaytan, F. Fay, M.E. Lobatto, J. Tang, M. Ouimet, Y. Kim, S.E. van der Staay, S.M. van Rijs, B. Priem, L. Zhang, E.A. Fisher, K.J. Moore, R. Langer, Z.A. Fayad, W.J. Mulder, HDL-mimetic PLGA nanoparticle to target atherosclerosis plaque macrophages, Bioconjug Chem, 26 (2015) 443-451.
[27] T. Skajaa, D.P. Cormode, P.A. Jarzyna, A. Delshad, C. Blachford, A. Barazza, E.A. Fisher, R.E. Gordon, Z.A. Fayad, W.J.M. Mulder, The biological properties of iron oxide

core high-density lipoprotein in experimental atherosclerosis, Biomaterials, 32 (2011) 206-213.
[28] R. Kuai, D. Li, Y.E. Chen, J.J. Moon, A. Schwendeman, High-Density Lipoproteins: Nature's Multifunctional Nanoparticles, ACS Nano, 10 (2016) 3015-3041.
[29] F.M. van der Valk, D.M. Schulte, S. Meiler, J. Tang, K.H. Zheng, J. Van den Bossche, T. Seijkens, M. Laudes, M. de Winther, E. Lutgens, A. Alaarg, J.M. Metselaar, G.M. Dallinga-Thie, W.J.M. Mulder, E.S.G. Stroes, A.A.J. Hamers, Liposomal prednisolone promotes macrophage lipotoxicity in experimental atherosclerosis, Nanomed-Nanotechnol, 12 (2016) 1463-1470.
[30] S. Diditchenko, A. Gille, I. Pragst, D. Stadler, M. Waelchli, R. Hamilton, A. Leis, S.D. Wright, Novel formulation of a reconstituted high-density lipoprotein (CSL112) dramatically enhances ABCA1-dependent cholesterol efflux, Arteriosclerosis, thrombosis, and vascular biology, 33 (2013) 2202-2211.
[31] A. Gille, R. Easton, D. D'Andrea, S.D. Wright, C.L. Shear, CSL112 enhances biomarkers of reverse cholesterol transport after single and multiple infusions in healthy subjects, Arteriosclerosis, thrombosis, and vascular biology, 34 (2014) 2106-2114.
[32] P. Tricoci, D.M. D'Andrea, P.A. Gurbel, Z. Yao, M. Cuchel, B. Winston, R. Schott, R. Weiss, M.A. Blazing, L. Cannon, A. Bailey, D.J. Angiolillo, A. Gille, C.L. Shear, S.D. Wright, J.H. Alexander, Infusion of Reconstituted High-Density Lipoprotein, CSL112, in Patients With Atherosclerosis: Safety and Pharmacokinetic Results From a Phase 2a Randomized Clinical Trial, J Am Heart Assoc, 4 (2015) e002171.
[33] C. Michael Gibson, S. Korjian, P. Tricoci, Y. Daaboul, M. Yee, P. Jain, J.H. Alexander, P.G. Steg, A.M. Lincoff, J.J. Kastelein, R. Mehran, D.M. D'Andrea, L.I. Deckelbaum, B. Merkely, M. Zarebinski, T.O. Ophuis, R.A. Harrington, Safety and Tolerability of CSL112, a Reconstituted, Infusible, Plasma-Derived Apolipoprotein A-I, After Acute Myocardial Infarction: The AEGIS-I Trial (ApoA-I Event Reducing in Ischemic Syndromes I), Circulation, 134 (2016) 1918-1930.
[34] C.M. Gibson, J.J.P. Kastelein, A.T. Phillips, P.E. Aylward, M.K. Yee, M. Tendera, S.J. Nicholls, S. Pocock, S.G. Goodman, J.H. Alexander, A.M. Lincoff, C. Bode, D. Duffy, M. Heise, G. Berman, S.J. Mears, P. Tricoci, L.I. Deckelbaum, P.G. Steg, P. Ridker, R. Mehran, Rationale and design of ApoA-I Event Reducing in Ischemic Syndromes II (AEGIS-II): A phase 3, multicenter, double-blind, randomized, placebo-controlled, parallel-group study to investigate the efficacy and safety of CSL112 in subjects after acute myocardial infarction, Am Heart J, 231 (2021) 121-127.
[35] R. Barbaras, Non-clinical development of CER-001, Front Pharmacol, 6 (2015) 220.
[36] C.H. Keyserling, R. Barbaras, R. Benghozi, J.L. Dasseux, Development of CER-001: Preclinical Dose Selection Through to Phase I Clinical Findings, Clin Drug Invest, 37 (2017) 483-491.
[37] J.C. Tardif, C.M. Ballantyne, P. Barter, J.L. Dasseux, Z.A. Fayad, M.C. Guertin, J.J. Kastelein, C. Keyserling, H. Klepp, W. Koenig, P.L. L'Allier, J. Lesperance, T.F. Luscher, J.F. Paolini, A. Tawakol, D.D. Waters, H.D.L.I.S.Q.A.R.I. Can, Effects of the high-density lipoprotein mimetic agent CER-001 on coronary atherosclerosis in patients with acute coronary syndromes: a randomized trial, European heart journal, 35 (2014) 3277-3286.
[38] Y. Kataoka, J. Andrews, M. Duong, T. Nguyen, N. Schwarz, J. Fendler, R. Puri, J. Butters, C. Keyserling, J.F. Paolini, J.L. Dasseux, S.J. Nicholls, Regression of coronary atherosclerosis with infusions of the high-density lipoprotein mimetic CER-001 in

patients with more extensive plaque burden, Cardiovascular diagnosis and therapy, 7 (2017) 252-263.
[39] J. Andrews, A. Janssan, T. Nguyen, A.D. Pisaniello, D.J. Scherer, J.J. Kastelein, B. Merkely, S.E. Nissen, K. Ray, G.G. Schwartz, S.G. Worthley, C. Keyserling, J.L. Dasseux, J. Butters, J. Girardi, R. Miller, S.J. Nicholls, Effect of serial infusions of reconstituted high-density lipoprotein (CER-001) on coronary atherosclerosis: rationale and design of the CARAT study, Cardiovascular diagnosis and therapy, 7 (2017) 45-51.
[40] S.J. Nicholls, J. Andrews, J.J.P. Kastelein, B. Merkely, S.E. Nissen, K.K. Ray, G.G. Schwartz, S.G. Worthley, C. Keyserling, J.L. Dasseux, L. Griffith, S.W. Kim, A. Janssan, G. Di Giovanni, A.D. Pisaniello, D.J. Scherer, P.J. Psaltis, J. Butters, Effect of Serial Infusions of CER-001, a Pre-beta High-Density Lipoprotein Mimetic, on Coronary Atherosclerosis in Patients Following Acute Coronary Syndromes in the CER-001 Atherosclerosis Regression Acute Coronary Syndrome Trial: A Randomized Clinical Trial, JAMA Cardiol, 3 (2018) 815-822.
[41] G.K. Hovingh, L.P. Smits, C. Stefanutti, H. Soran, S. Kwok, J. de Graaf, D. Gaudet, C.H. Keyserling, H. Klepp, J. Frick, J.F. Paolini, J.L. Dasseux, J.J. Kastelein, E.S. Stroes, The effect of an apolipoprotein A-I-containing high-density lipoprotein-mimetic particle (CER-001) on carotid artery wall thickness in patients with homozygous familial hypercholesterolemia: The Modifying Orphan Disease Evaluation (MODE) study, Am Heart J, 169 (2015) 736-742 e731.
[42] R.S. Kootte, L.P. Smits, F.M. van der Valk, J.L. Dasseux, C.H. Keyserling, R. Barbaras, J.F. Paolini, R.D. Santos, T.H. van Dijk, G.M. Dallinga-van Thie, A.J. Nederveen, W.J. Mulder, G.K. Hovingh, J.J. Kastelein, A.K. Groen, E.S. Stroes, Effect of open-label infusion of an apoA-I-containing particle (CER-001) on RCT and artery wall thickness in patients with FHA, Journal of lipid research, 56 (2015) 703-712.
[43] ClinicalTrials.gov, ClinicalTrials.gov Identifier: NCT0269713, CER-001 Therapy as a Novel Approach to Treat Genetic Orphan Diseases (TANGO).
[44] K.H. Zheng, Y. Kaiser, C.C. van Olden, R.D. Santos, J.L. Dasseux, J. Genest, D. Gaudet, J. Westerink, C. Keyserling, H.J. Verberne, E. Leitersdorf, R.A. Hegele, O.S. Descamps, P. Hopkins, A.J. Nederveen, E.S.G. Stroes, No benefit of HDL mimetic CER-001 on carotid atherosclerosis in patients with genetically determined very low HDL levels, Atherosclerosis, 311 (2020) 13-19.
[45] C. Pavanello, M. Turri, A. Strazzella, P. Tulissi, S. Pizzolitto, G. De Maglio, R. Nappi, L. Calabresi, G. Boscutti, The HDL mimetic CER-001 remodels plasma lipoproteins and reduces kidney lipid deposits in inherited lecithin:cholesterol acyltransferase deficiency, Journal of internal medicine, 291 (2022) 364-370.
[46] S. Faguer, D. Chauveau, M. Colombat, A. Delas, P. Bernadet-Monrozies, A. Beq, V. Soler, I. Labadens, A. Huart, P. Benlian, J.P. Schanstra, Administration of the High-Density Lipoprotein Mimetic CER-001 for Inherited Lecithin-Cholesterol Acyltransferase Deficiency, Annals of internal medicine, (2021).
[47] ABIONYX Pharma, ABIONYX Pharma Receives FDA Orphan Drug Designation (ODD) for CER-001 for the Treatment of LCAT Deficiency Presenting as Kidney Dysfunction and/or Ophthalmologic Disease, 2022.
[48] ABIONYX Pharma, ABIONYX initiates a Phase 2a clinical trial with CER-001 in septic patients at high risk of developing Acute Kidney Injury, 2020.

[49] ABIONYX Pharma, ABIONYX Pharma Reports Positive Interim Results From Phase 2a Clinical Trial Evaluating CER-001 in the Treatment of Septic Patients at High Risk of Developing Acute Kidney Injury, 2022.
[50] K.H. Zheng, J. Kroon, J. Schoormans, O. Gurney-Champion, S. Meijer, S. Gisbertz, M. Hulshof, D. Vugts, G. van Dongen, B. Coolen, H.J. Verberne, A. Nederveen, E. Stroes, H. van Laarhoven, (89)Zr-labeled High-Density Lipoprotein Nanoparticle PET imaging reveals tumor uptake in patients with esophageal cancer, J Nucl Med, (2022).
[51] S. Tanaka, F. Begue, B. Veeren, A. Tran-Dinh, T. Robert, P. Tashk, B. Lortat-Jacob, D. Faille, L. de Chaisemartin, N. Zappella, E. Atchade, L. Kramer, P. Montravers, O. Meilhac, First Recombinant High-Density Lipoprotein Particles Administration in a Severe ICU COVID-19 Patient, a Multi-Omics Exploratory Investigation, Biomedicines, 10 (2022).
[52] A.S. Xiang, B.A. Kingwell, Rethinking good cholesterol: a clinicians' guide to understanding HDL, The lancet. Diabetes & endocrinology, 7 (2019) 575-582.
[53] S. Kajani, S. Curley, F.C. McGillicuddy, Unravelling HDL-Looking beyond the Cholesterol Surface to the Quality Within, Int J Mol Sci, 19 (2018).
[54] E. Favari, M.J. Thomas, M.G. Sorci-Thomas, High-density lipoprotein functionality as a new pharmacological target on cardiovascular disease: unifying mechanism that explains high-density lipoprotein protection toward the progression of atherosclerosis, Journal of Cardiovascular Pharmacology, 71 (2018) 325-331.
[55] M.H. Caparon, K.J. Rust, A.K. Hunter, J.K. McLaughlin, K.E. Thomas, J.T. Herberg, R.E. Shell, P.B. Lanter, B.F. Bishop, R.L. Dufield, X. Wang, S.V. Ho, Integrated solution to purification challenges in the manufacture of a soluble recombinant protein in E. coli, Biotechnol Bioeng, 105 (2010) 239-249.
[56] M.H. Caparon, K.J. Rust, A.K. Hunter, J.K. McLaughlin, K.E. Thomas, J.T. Herberg, R.E. Shell, P.B. Lanter, B.F. Bishop, R.L. Dufield, X. Wang, S.V. Ho, Integrated Solution to Purification Challenges in the Manufacture of a Soluble Recombinant Protein in E. coli, Biotechnol Bioeng, 105 (2010) 239-249.
[57] S.A. Nankar, P.S. Kawathe, A.H. Pande, HDL, ApoA-I and ApoE-Mimetic Peptides: Potential Broad Spectrum Agent for Clinical Use?, Int J Pept Res Ther, 28 (2022).
[58] A. Wolska, M. Reimund, D.O. Sviridov, M.J. Amar, A.T. Remaley, Apolipoprotein Mimetic Peptides: Potential New Therapies for Cardiovascular Diseases, Cells, 10 (2021).
[59] L. Giorgi, A. Niemela, E.-P. Kumpula, O. Natri, P. Parkkila, J.T. Huiskonen, A.S. Koivuniemi, Mechanistic insights into the activation of lecithin-cholesterol acyltransferase in therapeutic nanodiscs composed of apolipoprotein AI mimetic peptides and phospholipids, bioRxiv, (2022).
[60] N. Satta, S. Pagano, B. Gencer, L. Kaiser, O. Hartley, F. Mach, A. Calmy, N. Vuilleumier, C-Terminus Apoa-1 Mimetic Peptides to Detect Cognate Auto-Antibodies and Reverse Hiv-Induced Foam Cell Formation, Atherosclerosis, 315 (2020) E124-E124.
[61] A. Kontush, M. Lhomme, M.J. Chapman, Thematic Review Series: High Density Lipoprotein Structure, Function, and Metabolism Unraveling the complexities of the HDL lipidome, Journal of lipid research, 54 (2013) 2950-2963.
[62] P. Keul, A. Polzin, K. Kaiser, M. Graler, L. Dannenberg, G. Daum, G. Heusch, B. Levkau, Potent anti-inflammatory properties of HDL in vascular smooth muscle cells

mediated by HDL-S1P and their impairment in coronary artery disease due to lower HDL-S1P: a new aspect of HDL dysfunction and its therapy, Faseb Journal, 33 (2019) 1482-1495.
[63] A.V. Thuy, C.M. Reimann, N.Y.A. Hemdan, M.H. Graler, Sphingosine 1-Phosphate in Blood: Function, Metabolism, and Fate, Cell Physiol Biochem, 34 (2014) 158-171.
[64] L. Camont, M. Lhomme, F. Rached, W. Le Goff, A. Negre-Salvayre, R. Salvayre, C. Calzada, M. Lagarde, M.J. Chapman, A. Kontush, Small, dense high-density lipoprotein-3 particles are enriched in negatively charged phospholipids: relevance to cellular cholesterol efflux, antioxidative, antithrombotic, anti-inflammatory, and antiapoptotic functionalities, Arteriosclerosis, thrombosis, and vascular biology, 33 (2013) 2715-2723.
[65] M.B. Naeini, V. Bianconi, M. Pirro, A. Sahebkar, The role of phosphatidylserine recognition receptors in multiple biological functions, Cell Mol Biol Lett, 25 (2020) 23.
[66] M. Darabi, A. Kontush, Can phosphatidylserine enhance atheroprotective activities of high-density lipoprotein?, Biochimie, 120 (2016) 81-86.
[67] M. Delgado-Rodríguez, M. Medina-Cuadros, A. Gómez-Ortega, G. Martínez-Gallego, M. Mariscal-Ortiz, M.A. Martinez-Gonzalez, M. Sillero-Arenas, Cholesterol and serum albumin levels as predictors of cross infection, death, and length of hospital stay, Archives of surgery, 137 (2002) 805-812.
[68] E. Bernal, M. Masiá, S. Padilla, F. Gutiérrez, High-density lipoprotein cholesterol in HIV-infected patients: evidence for an association with HIV-1 viral load, antiretroviral therapy status, and regimen composition, AIDS patient care and STDs, 22 (2008) 569-575.
[69] T.-C. Su, Y.-T. Lee, T.-J. Cheng, H.-P. Chien, J.-D. Wang, Chronic hepatitis B virus infection and dyslipidemia, Journal of the Formosan Medical Association, 103 (2004) 286-291.
[70] J.-Y. Chien, J.-S. Jerng, C.-J. Yu, P.-C. Yang, Low serum level of high-density lipoprotein cholesterol is a poor prognostic factor for severe sepsis, Crit Care Med, 33 (2005) 1688-1693.
[71] M.-H. Tsai, Y.-S. Peng, Y.-C. Chen, J.-M. Lien, Y.-C. Tian, J.-T. Fang, H.-H. Weng, P.-C. Chen, C.-W. Yang, C.-S. Wu, Low serum concentration of apolipoprotein AI is an indicator of poor prognosis in cirrhotic patients with severe sepsis, Journal of hepatology, 50 (2009) 906-915.
[72] L. Guo, E.E. Morin, M. Yu, L. Mei, M.V. Fawaz, Q. Wang, Y. Yuan, C.-G. Zhan, T.J. Standiford, A. Schwendeman, Replenishing HDL with synthetic HDL has multiple protective effects against sepsis in mice, Science Signaling, 15 (2022) eabl9322.
[73] D.R. Coelho, P.H. Carneiro, L. Mendes-Monteiro, J.N. Conde, I. Andrade, T. Cao, D. Allonso, M. White-Dibiasio, R.J. Kuhn, R. Mohana-Borges, ApoA1 Neutralizes Proinflammatory Effects of Dengue Virus NS1 Protein and Modulates Viral Immune Evasion, J Virol, 95 (2021) e0197420.
[74] S.Y. Kim, M. Yu, E.E. Morin, J. Kang, M.J. Kaplan, A. Schwendeman, High-Density Lipoprotein in Lupus: Disease Biomarkers and Potential Therapeutic Strategy, Arthritis & rheumatology, 72 (2020) 20-30.
[75] E. Botta, T. Merono, C. Saucedo, M. Martin, W. Tetzlaff, P. Sorroche, L. Boero, V. Malah, M. Menafra, L. Gomez Rosso, J.M. Chapman, A. Kontush, E. Soriano, F. Brites, Associations between disease activity, markers of HDL functionality and arterial stiffness in patients with rheumatoid arthritis, Atherosclerosis, 251 (2016) 438-444.

[76] A. Hafiane, E. Favari, S.S. Daskalopoulou, N. Vuilleumier, M.A. Frias, High-density lipoprotein cholesterol efflux capacity and cardiovascular risk in autoimmune and non-autoimmune diseases, Metabolism: clinical and experimental, 104 (2020) 154141.
[77] C.K. Smith, N.L. Seto, A. Vivekanandan-Giri, W. Yuan, M.P. Playford, Z. Manna, S.A. Hasni, R. Kuai, N.N. Mehta, A. Schwendeman, S. Pennathur, M.J. Kaplan, Lupus high-density lipoprotein induces proinflammatory responses in macrophages by binding lectin-like oxidised low-density lipoprotein receptor 1 and failing to promote activating transcription factor 3 activity, Annals of the rheumatic diseases, 76 (2017) 602-611.
[78] B.J. Wu, K.L. Ong, S. Shrestha, K. Chen, F. Tabet, P.J. Barter, K.A. Rye, Inhibition of Arthritis in the Lewis Rat by Apolipoprotein A-I and Reconstituted High-Density Lipoproteins, Arterioscl Throm Vas, 34 (2014) 543-551.
[79] L.K. Mooberry, N.A. Sabnis, M. Panchoo, B. Nagarajan, A.G. Lacko, Targeting the SR-B1 Receptor as a Gateway for Cancer Therapy and Imaging, Frontiers in Pharmacology, 7 (2016).
[80] S. Raut, L. Mooberry, N. Sabnis, A. Garud, A.S. Dossou, A. Lacko, Reconstituted HDL: Drug Delivery Platform for Overcoming Biological Barriers to Cancer Therapy, Frontiers in Pharmacology, 9 (2018).
[81] D. Chernick, R. Zhong, L. Li, The Role of HDL and HDL Mimetic Peptides as Potential Therapeutics for Alzheimer's Disease, Biomolecules, 10 (2020).
[82] C. Ducroux, J.P. Desilles, M.A. Mawhin, S. Delbosc, B. Ho-Tin-Noe, V. Ollivier, L. Di Meglio, B. Lapergue, J.B. Michel, P. Amarenco, Protective Effect of ApoA1 (Apolipoprotein A1)-Milano in a Rat Model of Large Vessel Occlusion Stroke, Stroke, 51 (2020) 1886-1890.
[83] M.L. Schultz, M.V. Fawaz, R.D. Azaria, T.C. Hollon, E.A. Liu, T.J. Kunkel, T.A. Halseth, K.L. Krus, R. Ming, E.E. Morin, H.S. McLoughlin, D.D. Bushart, H.L. Paulson, V.G. Shakkottai, D.A. Orringer, A.S. Schwendeman, A.P. Lieberman, Synthetic high-density lipoprotein nanoparticles for the treatment of Niemann-Pick diseases, BMC Med, 17 (2019) 200.
[84] L. Mei, M.Z. Yu, Y.Y. Liu, E. Weh, M. Pawar, L. Li, C.G. Besirli, A.A. Schwendeman, Synthetic high-density lipoprotein nanoparticles delivering rapamycin for the treatment of age-related macular degeneration, Nanomed-Nanotechnol, 44 (2022).
[85] N. Filipczak, J. Pan, S.S.K. Yalamarty, V.P. Torchilin, Recent advancements in liposome technology, Advanced drug delivery reviews, 156 (2020) 4-22.
[86] D.E. Large, R.G. Abdelmessih, E.A. Fink, D.T. Auguste, Liposome composition in drug delivery design, synthesis, characterization, and clinical application, Advanced drug delivery reviews, 176 (2021) 113851.
[87] Y. Fan, M. Marioli, K. Zhang, Analytical characterization of liposomes and other lipid nanoparticles for drug delivery, J Pharm Biomed Anal, 192 (2021) 113642.
[88] U.S.F.a.D. Administration, Liposome Drug Products: Chemistry, Manufacturing, and Controls; Human Pharmacokinetics and Bioavailability; and Labeling Documentation, 2018.
[89] U.S.F.a.D. Administration, Drug Products, Including Biological Products, that Contain Nanomaterials - Guidance for Industry, 2022.
[90] R. Nordstrom, L. Zhu, J. Harmark, Y. Levi-Kalisman, E. Koren, Y. Barenholz, G. Levinton, D. Shamrakov, Quantitative Cryo-TEM Reveals New Structural Details of Doxil-Like PEGylated Liposomal Doxorubicin Formulation, Pharmaceutics, 13 (2021).

[91] S. Bhattacharjee, DLS and zeta potential–what they are and what they are not?, Journal of controlled release, 235 (2016) 337-351.
[92] S. Bhattacharjee, DLS and zeta potential - What they are and what they are not?, Journal of controlled release : official journal of the Controlled Release Society, 235 (2016) 337-351.
[93] B. Ruozi, D. Belletti, A. Tombesi, G. Tosi, L. Bondioli, F. Forni, M.A. Vandelli, AFM, ESEM, TEM, and CLSM in liposomal characterization: a comparative study, Int J Nanomedicine, 6 (2011) 557-563.
[94] S. Peretz Damari, D. Shamrakov, M. Varenik, E. Koren, E. Nativ-Roth, Y. Barenholz, O. Regev, Practical aspects in size and morphology characterization of drug-loaded nano-liposomes, International journal of pharmaceutics, 547 (2018) 648-655.
[95] F. Caputo, D. Mehn, J.D. Clogston, M. Rosslein, A. Prina-Mello, S.E. Borgos, S. Gioria, L. Calzolai, Asymmetric-flow field-flow fractionation for measuring particle size, drug loading and (in)stability of nanopharmaceuticals. The joint view of European Union Nanomedicine Characterization Laboratory and National Cancer Institute - Nanotechnology Characterization Laboratory, J Chromatogr A, 1635 (2021) 461767.
[96] J. Parot, F. Caputo, D. Mehn, V.A. Hackley, L. Calzolai, Physical characterization of liposomal drug formulations using multi-detector asymmetrical-flow field flow fractionation, Journal of controlled release : official journal of the Controlled Release Society, 320 (2020) 495-510.
[97] S.M. Ansar, T. Mudalige, Characterization of doxorubicin liposomal formulations for size-based distribution of drug and excipients using asymmetric-flow field-flow fractionation (AF4) and liquid chromatography-mass spectrometry (LC-MS), International journal of pharmaceutics, 574 (2020) 118906.
[98] A.L. Robson, P.C. Dastoor, J. Flynn, W. Palmer, A. Martin, D.W. Smith, A. Woldu, S. Hua, Advantages and Limitations of Current Imaging Techniques for Characterizing Liposome Morphology, Front Pharmacol, 9 (2018) 80.
[99] M. Frohlich, V. Brecht, R. Peschka-Suss, Parameters influencing the determination of liposome lamellarity by 31P-NMR, Chem Phys Lipids, 109 (2001) 103-112.
[100] B.J. Boyd, T. Rades, Applications of small angle X-ray scattering in pharmaceutical science, Analytical Techniques in the Pharmaceutical Sciences, Springer2016, pp. 339-360.
[101] V. Nele, M.N. Holme, U. Kauscher, M.R. Thomas, J.J. Doutch, M.M. Stevens, Effect of Formulation Method, Lipid Composition, and PEGylation on Vesicle Lamellarity: A Small-Angle Neutron Scattering Study, Langmuir : the ACS journal of surfaces and colloids, 35 (2019) 6064-6074.
[102] D. Solomon, N. Gupta, N.S. Mulla, S. Shukla, Y.A. Guerrero, V. Gupta, Role of In Vitro Release Methods in Liposomal Formulation Development: Challenges and Regulatory Perspective, AAPS J, 19 (2017) 1669-1681.
[103] J. Shen, D.J. Burgess, In Vitro Dissolution Testing Strategies for Nanoparticulate Drug Delivery Systems: Recent Developments and Challenges, Drug Deliv Transl Res, 3 (2013) 409-415.
[104] N.S.S. Magalhaes, H. Fessi, F. Puisieux, S. Benita, M. Seiller, An in-Vitro Release Kinetic Examination and Comparative-Evaluation between Submicron Emulsion and Polylactic Acid Nanocapsules of Clofibride, Journal of Microencapsulation, 12 (1995) 195-205.

[105] I. Henriksen, S.A. Sande, G. Smistad, T. Agren, J. Karlsen, In-Vitro Evaluation of Drug-Release Kinetics from Liposomes by Fractional Dialysis, International journal of pharmaceutics, 119 (1995) 231-238.
[106] L. Mora, K.Y. Chumbimuni-Torres, C. Clawson, L. Hernandez, L. Zhang, J. Wang, Real-time electrochemical monitoring of drug release from therapeutic nanoparticles, Journal of controlled release : official journal of the Controlled Release Society, 140 (2009) 69-73.
[107] S. Holzschuh, K. Kaess, A. Fahr, C. Decker, Quantitative In Vitro Assessment of Liposome Stability and Drug Transfer Employing Asymmetrical Flow Field-Flow Fractionation (AF4), Pharmaceutical research, 33 (2016) 842-855.
[108] I.C.O.H.O.T.R.F.R.O.P.F.H. USE, PHARMACEUTICAL DEVELOPMENT Q8(R2) (2009).
[109] M. Kapoor, S.L. Lee, K.M. Tyner, Liposomal Drug Product Development and Quality: Current US Experience and Perspective, AAPS J, 19 (2017) 632-641.
[110] J.S.B. de Vlieger, D.J.A. Crommelin, K. Tyner, D.C. Drummond, W. Jiang, S.E. McNeil, S. Neervannan, R.M. Crist, V.P. Shah, Report of the AAPS Guidance Forum on the FDA Draft Guidance for Industry: "Drug Products, Including Biological Products, that Contain Nanomaterials", AAPS J, 21 (2019) 56.
[111] J. Shen, D.J. Burgess, In vitro-in vivo correlation for complex non-oral drug products: Where do we stand?, Journal of controlled release : official journal of the Controlled Release Society, 219 (2015) 644-651.
[112] M.P. Mast, H. Modh, C. Champanhac, J.W. Wang, G. Storm, J. Kramer, V. Mailander, G. Pastorin, M.G. Wacker, Nanomedicine at the crossroads - A quick guide for IVIVC, Advanced drug delivery reviews, 179 (2021) 113829.
[113] U.F.a.D. Administration., Draft Guidance on Bupivacaine, 2018.
[114] R.S. Hotchkiss, L.L. Moldawer, S.M. Opal, K. Reinhart, I.R. Turnbull, J.L. Vincent, Sepsis and septic shock, Nat Rev Dis Primers, 2 (2016) 16045.
[115] K. Kobiyama, K. Ley, Atherosclerosis, Circ Res, 123 (2018) 1118-1120.
[116] L. Wang, F.S. Wang, M.E. Gershwin, Human autoimmune diseases: a comprehensive update, Journal of internal medicine, 278 (2015) 369-395.
[117] M.A. Gimbrone, Jr., G. Garcia-Cardena, Endothelial Cell Dysfunction and the Pathobiology of Atherosclerosis, Circ Res, 118 (2016) 620-636.
[118] E.V. Dolmatova, K. Wang, R. Mandavilli, K.K. Griendling, The effects of sepsis on endothelium and clinical implications, Cardiovasc Res, 117 (2021) 60-73.
[119] G. Grandl, C. Wolfrum, Hemostasis, endothelial stress, inflammation, and the metabolic syndrome, Semin Immunopathol, 40 (2018) 215-224.
[120] G. Murdaca, B.M. Colombo, P. Cagnati, R. Gulli, F. Spano, F. Puppo, Endothelial dysfunction in rheumatic autoimmune diseases, Atherosclerosis, 224 (2012) 309-317.
[121] D.A. Chistiakov, A.N. Orekhov, Y.V. Bobryshev, Effects of shear stress on endothelial cells: go with the flow, Acta Physiol (Oxf), 219 (2017) 382-408.
[122] K. Peters, R.E. Unger, J. Brunner, C.J. Kirkpatrick, Molecular basis of endothelial dysfunction in sepsis, Cardiovasc Res, 60 (2003) 49-57.
[123] C. Zhang, The role of inflammatory cytokines in endothelial dysfunction, Basic Res Cardiol, 103 (2008) 398-406.

[124] P. Theofilis, M. Sagris, E. Oikonomou, A.S. Antonopoulos, G. Siasos, C. Tsioufis, D. Tousoulis, Inflammatory Mechanisms Contributing to Endothelial Dysfunction, Biomedicines, 9 (2021).
[125] J.F. Leeuwenberg, E.F. Smeets, J.J. Neefjes, M.A. Shaffer, T. Cinek, T.M. Jeunhomme, T.J. Ahern, W.A. Buurman, E-selectin and intercellular adhesion molecule-1 are released by activated human endothelial cells in vitro, Immunology, 77 (1992) 543-549.
[126] T. Collins, H.J. Palmer, M.Z. Whitley, A.S. Neish, A.J. Williams, A Common Theme in Endothelial Activation - Insights from the Structural-Analysis of the Genes for E-Selectin and Vcam-1, Trends Cardiovas Med, 3 (1993) 92-97.
[127] M. Khatami, Unresolved inflammation: 'immune tsunami' or erosion of integrity in immune-privileged and immune-responsive tissues and acute and chronic inflammatory diseases or cancer, Expert Opin Biol Th, 11 (2011) 1419-1432.
[128] J. Viola, O. Soehnlein, Atherosclerosis - A matter of unresolved inflammation, Seminars in immunology, 27 (2015) 184-193.
[129] M. Back, A. Yurdagul, Jr., I. Tabas, K. Oorni, P.T. Kovanen, Inflammation and its resolution in atherosclerosis: mediators and therapeutic opportunities, Nature reviews. Cardiology, 16 (2019) 389-406.
[130] C. Buechler, R. Pohl, C. Aslanidis, Pro-Resolving Molecules-New Approaches to Treat Sepsis?, Int J Mol Sci, 18 (2017).
[131] T. Umemoto, C.Y. Han, P. Mitra, M.M. Averill, C. Tang, L. Goodspeed, M. Omer, S. Subramanian, S. Wang, L.J. Den Hartigh, H. Wei, E.J. Kim, J. Kim, K.D. O'Brien, A. Chait, Apolipoprotein AI and high-density lipoprotein have anti-inflammatory effects on adipocytes via cholesterol transporters: ATP-binding cassette A-1, ATP-binding cassette G-1, and scavenger receptor B-1, Circ Res, 112 (2013) 1345-1354.
[132] C. Mineo, H. Deguchi, J.H. Griffin, P.W. Shaul, Endothelial and antithrombotic actions of HDL, Circ Res, 98 (2006) 1352-1364.
[133] P.W. Shaul, Regulation of endothelial nitric oxide synthase: location, location, location, Annu Rev Physiol, 64 (2002) 749-774.
[134] G.W. Cockerill, K.A. Rye, J.R. Gamble, M.A. Vadas, P.J. Barter, High-Density-Lipoproteins Inhibit Cytokine-Induced Expression of Endothelial-Cell Adhesion Molecules, Arterioscl Throm Vas, 15 (1995) 1987-1994.
[135] M. Sugano, K. Tsuchida, N. Makino, High-density lipoproteins protect endothelial cells from tumor necrosis factor-alpha-induced apoptosis, Biochem Bioph Res Co, 272 (2000) 872-876.
[136] J.A. de Souza, C. Vindis, A. Negre-Salvayre, K.A. Rye, M. Couturier, P. Therond, S. Chantepie, R. Salvayre, M.J. Chapman, A. Kontush, Small, dense HDL 3 particles attenuate apoptosis in endothelial cells: pivotal role of apolipoprotein A-I, Journal of cellular and molecular medicine, 14 (2010) 608-620.
[137] A. Abudukeremu, C.X. Huang, H.W. Li, R.L. Sun, X. Liu, X.Y. Wu, X.K. Xie, J.J. Huang, J. Zhang, J.L. Bao, Y.L. Zhang, Efficacy and Safety of High-Density Lipoprotein/Apolipoprotein A1 Replacement Therapy in Humans and Mice With Atherosclerosis: A Systematic Review and Meta-Analysis, Front Cardiovasc Med, 8 (2021).
[138] M. Khan, N. Lalwani, S. Drake, J. Crockatt, J. Dasseux, Single-dose intravenous infusion of ETC-642, a 22-Mer ApoA-I analogue and phospholipids complex, elevates

HDL-C in atherosclerosis patients, Circulation, LIPPINCOTT WILLIAMS & WILKINS 530 WALNUT ST, PHILADELPHIA, PA 19106-3621 USA, 2003, pp. 563-564.
[139] E. Zakiev, M. Feng, V. Sukhorukov, A. Kontush, HDL-Targeting Therapeutics: Past, Present and Future, Curr Pharm Des, 23 (2017) 1207-1215.
[140] S. Tanaka, F. Begue, B. Veeren, A. Tran-Dinh, T. Robert, P. Tashk, B. Lortat-Jacob, D. Faille, L. de Chaisemartin, N. Zappella, First Recombinant High-Density Lipoprotein Particles Administration in a Severe ICU COVID-19 Patient, a Multi-Omics Exploratory Investigation, Biomedicines, 10 (2022) 754.
[141] R. Alon, P.D. Kassner, M.W. Carr, E.B. Finger, M.E. Hemler, T.A. Springer, The Integrin Vla-4 Supports Tethering and Rolling in Flow on Vcam-1, Journal of Cell Biology, 128 (1995) 1243-1253.
[142] K.A. Kelly, M. Nahrendorf, A.M. Yu, F. Reynolds, R. Weissleder, In vivo phage display selection yields atherosclerotic plaque targeted peptides for imaging, Molecular Imaging and Biology, 8 (2006) 201-207.
[143] G. Ailuno, S. Baldassari, G. Zuccari, M. Schlich, G. Caviglioli, Peptide-based nanosystems for vascular cell adhesion molecule-1 targeting: a real opportunity for therapeutic and diagnostic agents in inflammation associated disorders, J Drug Deliv Sci Tec, 55 (2020).
[144] R. Kuai, L.J. Ochyl, K.S. Bahjat, A. Schwendeman, J.J. Moon, Designer vaccine nanodiscs for personalized cancer immunotherapy, Nat Mater, 16 (2017) 489-496.
[145] M.V. Fawaz, S.Y. Kim, D. Li, R. Ming, Z. Xia, K. Olsen, I.D. Pogozheva, J.J.G. Tesmer, A. Schwendeman, Phospholipid Component Defines Pharmacokinetic and Pharmacodynamic Properties of Synthetic High-Density Lipoproteins, The Journal of pharmacology and experimental therapeutics, 372 (2020) 193-204.
[146] A. Schwendeman, D.O. Sviridov, W. Yuan, Y. Guo, E.E. Morin, Y. Yuan, J. Stonik, L. Freeman, A. Ossoli, S. Thacker, S. Killion, M. Pryor, Y.E. Chen, S. Turner, A.T. Remaley, The effect of phospholipid composition of reconstituted HDL on its cholesterol efflux and anti-inflammatory properties, Journal of lipid research, 56 (2015) 1727-1737.
[147] D.J. Medina-Leyte, M. Dominguez-Perez, I. Mercado, M.T. Villarreal-Molina, L. Jacobo-Albavera, Use of Human Umbilical Vein Endothelial Cells (HUVEC) as a Model to Study Cardiovascular Disease: A Review, Appl Sci-Basel, 10 (2020).
[148] D. Li, M.V. Fawaz, E.E. Morin, R. Ming, D. Sviridov, J. Tang, R. Ackermann, K. Olsen, A.T. Remaley, A. Schwendeman, Effect of Synthetic High Density Lipoproteins Modification with Polyethylene Glycol on Pharmacokinetics and Pharmacodynamics, Molecular pharmaceutics, 15 (2018) 83-96.
[149] Y. Guo, W. Yuan, B. Yu, R. Kuai, W. Hu, E.E. Morin, M.T. Garcia-Barrio, J. Zhang, J.J. Moon, A. Schwendeman, Y. Eugene Chen, Synthetic High-Density Lipoprotein-Mediated Targeted Delivery of Liver X Receptors Agonist Promotes Atherosclerosis Regression, EBioMedicine, 28 (2018) 225-233.
[150] K. Thayse, N. Kindt, S. Laurent, S. Carlier, VCAM-1 Target in Non-Invasive Imaging for the Detection of Atherosclerotic Plaques, Biology (Basel), 9 (2020).
[151] F. Garello, A. Pagoto, F. Arena, A. Buffo, F. Blasi, D. Alberti, E. Terreno, MRI visualization of neuroinflammation using VCAM-1 targeted paramagnetic micelles, Nanomedicine : nanotechnology, biology, and medicine, 14 (2018) 2341-2350.

[152] J.H. Park, Y. Jiang, J. Zhou, H. Gong, A. Mohapatra, J. Heo, W. Gao, R.H. Fang, L. Zhang, Genetically engineered cell membrane-coated nanoparticles for targeted delivery of dexamethasone to inflamed lungs, Sci Adv, 7 (2021).
[153] C.S. Thaxton, J.S. Rink, P.C. Naha, D.P. Cormode, Lipoproteins and lipoprotein mimetics for imaging and drug delivery, Advanced drug delivery reviews, 106 (2016) 116-131.
[154] S.Y. Kim, Optimization of Synthetic High-Density Lipoprotein Nanostructures for Treatment of Inflammatory Diseases, 2019.
[155] B.A. Di Bartolo, S.J. Nicholls, S. Bao, K.-A. Rye, A.K. Heather, P.J. Barter, C. Bursill, The apolipoprotein AI mimetic peptide ETC-642 exhibits anti-inflammatory properties that are comparable to high density lipoproteins, Atherosclerosis, 217 (2011) 395-400.
[156] J. Miles, M. Khan, C. Painchaud, N. Lalwani, S. Drake, J. Dasseux, Single-dose tolerability, pharmacokinetics, and cholesterol mobilization in HDL-C fraction following intravenous administration of ETC-642, a 22-mer ApoA-I analogue and phospholipids complex, in atherosclerosis patients, Arterioscl Throm Vas, LIPPINCOTT WILLIAMS & WILKINS 530 WALNUT ST, PHILADELPHIA, PA 19106-3621 USA, 2004, pp. E19-E19.
[157] K.H. Zheng, F.M. van der Valk, L.P. Smits, M. Sandberg, J.L. Dasseux, R. Baron, R. Barbaras, C. Keyserling, B.F. Coolen, A.J. Nederveen, H.J. Verberne, T.E. Nell, D.J. Vugts, R. Duivenvoorden, Z.A. Fayad, W.J.M. Mulder, G. van Dongen, E.S.G. Stroes, HDL mimetic CER-001 targets atherosclerotic plaques in patients, Atherosclerosis, 251 (2016) 381-388.
[158] B. Plochberger, M. Axmann, C. Rohrl, J. Weghuber, M. Brameshuber, B.K. Rossboth, S. Mayr, R. Ros, R. Bittman, H. Stangl, G.J. Schutz, Direct observation of cargo transfer from HDL particles to the plasma membrane, Atherosclerosis, 277 (2018) 53-59.
[159] D. Goti, A. Hrzenjak, S. Levak-Frank, S. Frank, D.R. van der Westhuyzen, E. Malle, W. Sattler, Scavenger receptor class B, type I is expressed in porcine brain capillary endothelial cells and contributes to selective uptake of HDL-associated vitamin E, J Neurochem, 76 (2001) 498-508.
[160] K.A. Kelly, J.R. Allport, A. Tsourkas, V.R. Shinde-Patil, L. Josephson, R. Weissleder, Detection of vascular adhesion molecule-1 expression using a novel multimodal nanoparticle, Circulation Research, 96 (2005) 327-336.
[161] N.A. Maniatis, A. Kotanidou, J.D. Catravas, S.E. Orfanos, Endothelial pathomechanisms in acute lung injury, Vascul Pharmacol, 49 (2008) 119-133.
[162] A. Trakaki, G. Marsche, Current Understanding of the Immunomodulatory Activities of High-Density Lipoproteins, Biomedicines, 9 (2021).
[163] K.R. Primer, P.J. Psaltis, J.T.M. Tan, C.A. Bursill, The Role of High-Density Lipoproteins in Endothelial Cell Metabolism and Diabetes-Impaired Angiogenesis, Int J Mol Sci, 21 (2020).
[164] H. Karlsson, A. Kontush, R.W. James, Functionality of HDL: antioxidation and detoxifying effects, Handbook of experimental pharmacology, 224 (2015) 207-228.
[165] F. Begue, S. Tanaka, Z. Mouktadi, P. Rondeau, B. Veeren, N. Diotel, A. Tran-Dinh, T. Robert, E. Velia, P. Mavingui, M. Lagrange-Xelot, P. Montravers, D. Couret, O. Meilhac, Altered high-density lipoprotein composition and functions during severe COVID-19, Scientific reports, 11 (2021) 2291.

[166] D. Capodanno, R. Mehran, C.M. Gibson, D.J. Angiolillo, CSL112, a reconstituted, infusible, plasma-derived apolipoprotein A-I: safety and tolerability profiles and implications for management in patients with myocardial infarction, Expert opinion on investigational drugs, 27 (2018) 997-1005.
[167] J.-L. Dasseux, ETC-642, a Peptide/phospholipids complex that mimics the structure and functions of high density lipoproteins (HDL), 2004, pp. presented at TIDES Conference.
[168] C.H. Keyserling, T.L. Hunt, H.M. Klepp, R.A. Scott, R. Barbaras, A. Schwendeman, N. Lalwani, J.L. Dasseux, CER-001, a Synthetic HDL-Mimetic, Safely Mobilizes Cholesterol in Healthy Dyslipidemic Volunteers, Circulation, 124 (2011).
[169] I. Karalis, J.W. Jukema, HDL Mimetics Infusion and Regression of Atherosclerosis: Is It Still Considered a Valid Therapeutic Option?, Curr Cardiol Rep, 20 (2018) 66.
[170] M. Darabi, A. Kontush, Phosphatidylserine in atherosclerosis, Current opinion in lipidology, 27 (2016) 414-420.
[171] F.Y. Glassman, J.L. Schneider, R. Ramakrishnan, R.K. Dingman, M. Ramanathan, R.B. Bankert, S.V. Balu-Iyer, Phosphatidylserine Is Not Just a Cleanup Crew but Also a Well-Meaning Teacher, Journal of pharmaceutical sciences, 107 (2018) 2048-2054.
[172] M. Darabi, M. Lhomme, V.D. Dahik, I. Guillas, E. Frisdal, E. Tubeuf, L. Poupel, M. Patel, E.L. Gautier, T. Huby, M. Guerin, K.A. Rye, P. Lesnik, W. Le Goff, A. Kontush, Phosphatidylserine enhances anti-inflammatory effects of reconstituted HDL in macrophages via distinct intracellular pathways, FASEB J, 36 (2022) e22274.
[173] M. Darabi, I. Guillas-Baudouin, W. Le Goff, M.J. Chapman, A. Kontush, Therapeutic applications of reconstituted HDL: When structure meets function, Pharmacology & therapeutics, 157 (2016) 28-42.
[174] A.C. Doran, A. Yurdagul, Jr., I. Tabas, Efferocytosis in health and disease, Nature reviews. Immunology, 20 (2020) 254-267.
[175] F. Abdolmaleki, N. Farahani, S.M. Gheibi Hayat, M. Pirro, V. Bianconi, G.E. Barreto, A. Sahebkar, The Role of Efferocytosis in Autoimmune Diseases, Front Immunol, 9 (2018) 1645.
[176] A. Yurdagul, Jr., A.C. Doran, B. Cai, G. Fredman, I.A. Tabas, Mechanisms and Consequences of Defective Efferocytosis in Atherosclerosis, Front Cardiovasc Med, 4 (2017) 86.
[177] R.B. Birge, S. Boeltz, S. Kumar, J. Carlson, J. Wanderley, D. Calianese, M. Barcinski, R.A. Brekken, X. Huang, J.T. Hutchins, B. Freimark, C. Empig, J. Mercer, A.J. Schroit, G. Schett, M. Herrmann, Phosphatidylserine is a global immunosuppressive signal in efferocytosis, infectious disease, and cancer, Cell Death Differ, 23 (2016) 962-978.
[178] R.F. Fernandez-Boyanapalli, S.C. Frasch, K. McPhillips, R.W. Vandivier, B.L. Harry, D.W. Riches, P.M. Henson, D.L. Bratton, Impaired apoptotic cell clearance in CGD due to altered macrophage programming is reversed by phosphatidylserine-dependent production of IL-4, Blood, 113 (2009) 2047-2055.
[179] A.M. Fond, C.S. Lee, I.G. Schulman, R.S. Kiss, K.S. Ravichandran, Apoptotic cells trigger a membrane-initiated pathway to increase ABCA1, The Journal of clinical investigation, 125 (2015) 2748-2758.

[180] R.S. Kiss, M.R. Elliott, Z. Ma, Y.L. Marcel, K.S. Ravichandran, Apoptotic cells induce a phosphatidylserine-dependent homeostatic response from phagocytes, Curr Biol, 16 (2006) 2252-2258.
[181] J.A. Kamps, H.W. Morselt, G.L. Scherphof, Uptake of liposomes containing phosphatidylserine by liver cells in vivo and by sinusoidal liver cells in primary culture: in vivo-in vitro differences, Biochem Biophys Res Commun, 256 (1999) 57-62.
[182] D. Liu, F. Liu, Y.K. Song, Recognition and clearance of liposomes containing phosphatidylserine are mediated by serum opsonin, Biochim Biophys Acta, 1235 (1995) 140-146.
[183] S. Raut, L. Mooberry, N. Sabnis, A. Garud, A.S. Dossou, A. Lacko, Reconstituted HDL: Drug Delivery Platform for Overcoming Biological Barriers to Cancer Therapy, Front Pharmacol, 9 (2018) 1154.
[184] P. Palatini, G. Viola, E. Bigon, A.M. Menegus, A. Bruni, Pharmacokinetic characterization of phosphatidylserine liposomes in the rat, British journal of pharmacology, 102 (1991) 345-350.
[185] M.A. Shetab Boushehri, A. Lamprecht, Nanoparticles as drug carriers: current issues with in vitro testing, Nanomedicine (Lond), 10 (2015) 3213-3230.
[186] Y. Zambito, E. Pedreschi, G. Di Colo, Is dialysis a reliable method for studying drug release from nanoparticulate systems?-A case study, International journal of pharmaceutics, 434 (2012) 28-34.
[187] G. Moreno-Bautista, K.C. Tam, Evaluation of dialysis membrane process for quantifying the in vitro drug-release from colloidal drug carriers, Colloid Surface A, 389 (2011) 299-303.
[188] C. Washington, Evaluation of Non-Sink Dialysis Methods for the Measurement of Drug Release from Colloids - Effects of Drug Partition, International journal of pharmaceutics, 56 (1989) 71-74.
[189] S.J. Wallace, J. Li, R.L. Nation, B.J. Boyd, Drug release from nanomedicines: Selection of appropriate encapsulation and release methodology, Drug Deliv Transl Res, 2 (2012) 284-292.
[190] M.Y. Levy, S. Benita, Drug Release from Submicronized O/W Emulsion - a New Invitro Kinetic Evaluation Model, International journal of pharmaceutics, 66 (1990) 29-37.
[191] S.A. Abouelmagd, B. Sun, A.C. Chang, Y.J. Ku, Y. Yeo, Release Kinetics Study of Poorly Water-Soluble Drugs from Nanoparticles: Are We Doing It Right?, Molecular pharmaceutics, 12 (2015) 997-1003.
[192] S. Modi, B.D. Anderson, Determination of Drug Release Kinetics from Nanoparticles: Overcoming Pitfalls of the Dynamic Dialysis Method, Molecular pharmaceutics, 10 (2013) 3076-3089.
[193] K.D. Fugit, B.D. Anderson, Dynamic, Nonsink Method for the Simultaneous Determination of Drug Permeability and Binding Coefficients in Liposomes, Molecular pharmaceutics, 11 (2014) 1314-1325.
[194] R. Schwarzl, F. Du, R. Haag, R.R. Netz, General method for the quantification of drug loading and release kinetics of nanocarriers, European journal of pharmaceutics and biopharmaceutics : official journal of Arbeitsgemeinschaft fur Pharmazeutische Verfahrenstechnik e.V, 116 (2017) 131-137.

[195] W. Yuan, R. Kuai, Z. Dai, Y. Yuan, N. Zheng, W. Jiang, C. Noble, M. Hayes, F.C. Szoka, A. Schwendeman, Development of a Flow-Through USP-4 Apparatus Drug Release Assay to Evaluate Doxorubicin Liposomes, AAPS J, 19 (2017) 150-160.
[196] X. Xu, M.A. Khan, D.J. Burgess, A two-stage reverse dialysis in vitro dissolution testing method for passive targeted liposomes, International journal of pharmaceutics, 426 (2012) 211-218.
[197] V. Papadopoulou, K. Kosmidis, M. Vlachou, P. Macheras, On the use of the Weibull function for the discernment of drug release mechanisms, International journal of pharmaceutics, 309 (2006) 44-50.
[198] C. Washington, Drug Release from Microdisperse Systems - a Critical-Review, International journal of pharmaceutics, 58 (1990) 1-12.
[199] P. Chahar, K.C. Cummings, 3rd, Liposomal bupivacaine: a review of a new bupivacaine formulation, J Pain Res, 5 (2012) 257-264.
[200] Exparel® [prescribing information].
[201] S.R. Gorfine, E. Onel, G. Patou, Z.V. Krivokapic, Bupivacaine extended-release liposome injection for prolonged postsurgical analgesia in patients undergoing hemorrhoidectomy: a multicenter, randomized, double-blind, placebo-controlled trial, Dis Colon Rectum, 54 (2011) 1552-1559.
[202] I. Pacira Pharmaceuticals, PACIRA BIOSCIENCES REPORTS FULL-YEAR AND FOURTH QUARTER 2020 FINANCIAL RESULTS, 2021.
[203] M.B. Sankaram, S. Kim, Multivesicular liposomes with controlled release of encapsulated biologically active substances, in: U.S.P.a.T. Office (Ed.), PACIRA PHARMACEUTICALS Inc US, 2000.
[204] M.B. Sankaram, S. Kim, Preparation of multivesicular liposomes for controlled release of encapsulated biologically active substances, in: U.S.P.a.T. Office. (Ed.), Pacira Pharmaceuticals Inc, 1999.
[205] S. Kim, T. Kim, S. Murdande, Sustained-release liposomal anesthetic compositions, in: U.S.P.a.T. Office. (Ed.), Pacira Pharmaceuticals Inc, 2014.
[206] H. Hartounian, D. Meissner, C.B. Pepper, Production of multivesicular liposomes, in: U.S.P.a.T. Office. (Ed.), 2017.
[207] Q. Ye, J. Asherman, M. Stevenson, E. Brownson, N.V. Katre, DepoFoam technology: a vehicle for controlled delivery of protein and peptide drugs, Journal of controlled release : official journal of the Controlled Release Society, 64 (2000) 155-166.
[208] S. Mantripragada, A lipid based depot (DepoFoam technology) for sustained release drug delivery, Prog Lipid Res, 41 (2002) 392-406.
[209] M.S. Angst, D.R. Drover, Pharmacology of drugs formulated with DepoFoam: a sustained release drug delivery system for parenteral administration using multivesicular liposome technology, Clinical pharmacokinetics, 45 (2006) 1153-1176.
[210] J.S. Hall, D.J. Turnbull, J. John J. Grigsby , S.M. Ardekani, P.N. Davis, L.D. Garcia, S.M. Kurz, K.D.A. Los, Manufacturing of bupivacaine multivesicular liposomes, Pacira Pharmaceuticals Inc, 2021.
[211] Q. Ye, N. Katre, M. Sankaram, Modulation of drug loading in multivescular liposomes, in: U.S.P.a.T. Office. (Ed.), Pacira Pharmaceuticals Inc, 2000.
[212] A. Chaurasiya, A. Gorajiya, K. Panchal, S. Katke, A.K. Singh, A review on multivesicular liposomes for pharmaceutical applications: preparation, characterization, and translational challenges, Drug Deliv Transl Res, (2021).

[213] T. Toliyat, Z. Khorasanirad, Development of a Depofoam Technology for the Sustained Delivery of Desferrioxamine Mesylate, DARU Journal of Pharmaceutical Sciences, 11 (2003) 88-94.
[214] S.P. Vyas, M. Rawat, A. Rawat, S. Mahor, P.N. Gupta, Pegylated protein encapsulated multivesicular liposomes: a novel approach for sustained release of interferon alpha, Drug Dev Ind Pharm, 32 (2006) 699-707.
[215] S. Manna, Y. Wu, Y. Wang, B. Koo, L. Chen, P. Petrochenko, Y. Dong, S. Choi, D. Kozak, B. Oktem, X. Xu, J. Zheng, Probing the mechanism of bupivacaine drug release from multivesicular liposomes, Journal of controlled release : official journal of the Controlled Release Society, 294 (2019) 279-287.
[216] B.H. Lu, Q.Y. Ma, J. Zhang, R. Liu, Z.G. Yue, C.L. Xu, Z.H. Li, H.Q. Lin, Preparation and characterization of bupivacaine multivesicular liposome: A QbD study about the effects of formulation and process on critical quality attributes, International journal of pharmaceutics, 598 (2021).
[217] Q. Ye, M.B. Sankaram, Method for producing liposomes with increased percent of compound encapsulated, in: U.S.P.a.T. Office. (Ed.), Pacira Pharmaceuticals Inc, 1999.
[218] S. Kim, M.S. Turker, E.Y. Chi, S. Sela, G.M. Martin, Preparation of Multivesicular Liposomes, Biochimica Et Biophysica Acta, 728 (1983) 339-348.
[219] S. Kim, T. Kim, S. Murdandi, Sustained-release liposomal anesthetic compositions, in: U.S.P.a.T. Office. (Ed.), Pacira Pharmaceuticals Inc, 2000.
[220] N. Zheng, W. Jiang, R. Lionberger, L.X. Yu, Bioequivalence for Liposomal Drug Products, in: L.X. Yu, B.V. Li (Eds.) FDA Bioequivalence Standards, Springer New York, New York, NY, 2014, pp. 275-296.
[221] Keynote and Industry Survey Results - GDUFA Science and Research Initiatives Public Workshop, 2021.
[222] M.S. Spector, J.A. Zasadzinski, M.B. Sankaram, Topology of multivesicular liposomes, a model biliquid foam, Langmuir : the ACS journal of surfaces and colloids, 12 (1996) 4704-4708.
[223] J.F. Ellena, M. Le, D.S. Cafiso, R.M. Solis, M. Langston, M.B. Sankaram, Distribution of phospholipids and triglycerides in multivesicular lipid particles, Drug delivery, 6 (1999) 97-106.
[224] F.R. Kohn, S.A. Malkmus, E.A. Brownson, S.S. Rossi, T.L. Yaksh, Fate of the predominant phospholipid component of DepoFoam drug delivery matrix after intrathecal administration of sustained-release encapsulated cytarabine in rats, Drug delivery, 5 (1998) 143-151.
[225] J. Zborowski, F. Roerdink, G. Scherphof, Leakage of Sucrose from Phosphatidylcholine Liposomes Induced by Interaction with Serum-Albumin, Biochimica Et Biophysica Acta, 497 (1977) 183-191.